Cell Reports

Article

Oligodendrocyte-derived LGI3 and its receptor ADAM23 organize juxtaparanodal Kv1 channel clustering for short-term synaptic plasticity

Graphical abstract

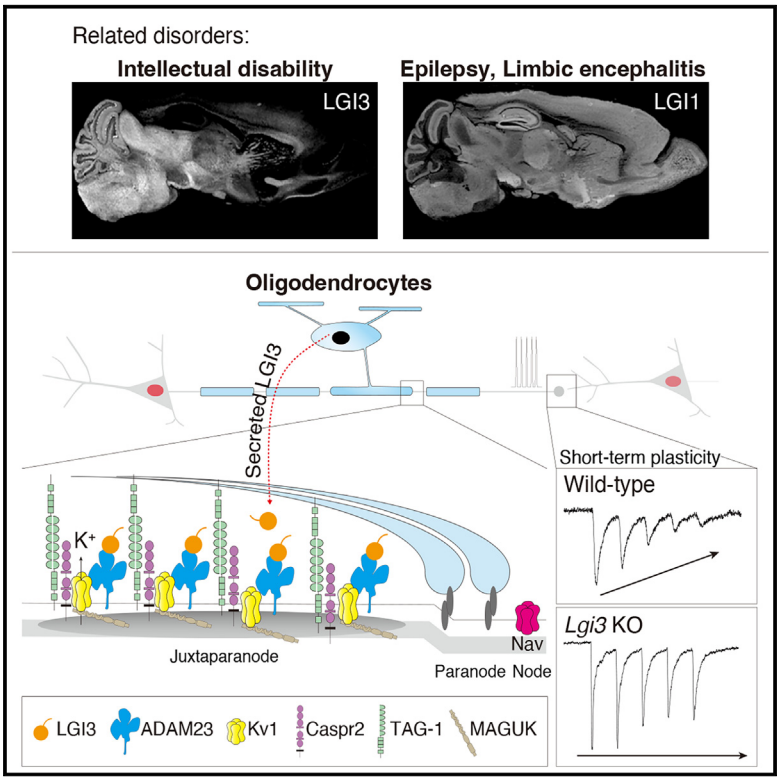

Highlights

- Oligodendrocyte-derived LGI3 forms nanoclusters at juxtaparanodes of myelinated axons
- LGI3 is required for juxtaparanodal clustering of ADAM23 and Kv1 channels
- LGI3 regulates Kv1-channel-dependent short-term plasticity in the cerebral cortex
- Juxtaparanodal LGI3-ADAM23-Kv1 channel is a possible molecular pathway affected in ID

Authors

Yuri Miyazaki, Takeshi Otsuka, Yoko Yamagata, ..., Masumi Hirabayashi, Yuko Fukata, Masaki Fukata

Correspondence

fukata.yuko.y1@f.mail.nagoya-u.ac.jp (Y.F.), fukata.masaki.h6@f.mail.nagoya-u.ac.jp (M.F.)

In brief

Miyazaki et al. show that intellectual-disability-related ligand LGI3 is secreted from oligodendrocytes and specifically clustered at the juxtaparanode of myelinated axons together with its axonal receptor, ADAM23. The juxtaparanode-specific action of LGI3 allows us to serendipitously isolate a subcellular-specific role of ubiquitously expressed Kv1 channels in short-term synaptic plasticity.

Miyazaki et al., 2024, Cell Reports *43*, 113634
January 23, 2024 © 2023 The Author(s).
https://doi.org/10.1016/j.celrep.2023.113634

CellPress

Cell Reports

CellPress
OPEN ACCESS

Article

Oligodendrocyte-derived LGI3 and its receptor ADAM23 organize juxtaparanodal Kv1 channel clustering for short-term synaptic plasticity

Yuri Miyazaki,[1,2] Takeshi Otsuka,[3,4] Yoko Yamagata,[5] Toshihiro Endo,[6] Makoto Sanbo,[7] Hiromi Sano,[8] Kenta Kobayashi,[4,9] Hiroki Inahashi,[2] Hans-Christian Kornau,[10,11] Dietmar Schmitz,[10,11] Harald Prüss,[10,12,13] Dies Meijer,[14,15] Masumi Hirabayashi,[4,7] Yuko Fukata,[2,16,*] and Masaki Fukata[1,2,4,17,*]

[1]Division of Neuropharmacology, Nagoya University Graduate School of Medicine, Nagoya 466-8550, Japan
[2]Division of Membrane Physiology, Department of Molecular and Cellular Physiology, National Institute for Physiological Sciences, National Institutes of Natural Sciences, Okazaki, Aichi 444-8787, Japan
[3]Section of Cellular Electrophysiology, National Institute for Physiological Sciences, National Institutes of Natural Sciences, Okazaki, Aichi 444-8787, Japan
[4]Graduate Institute for Advanced Studies, SOKENDAI, Okazaki, Aichi 444-8585, Japan
[5]Section of Multilayer Physiology, National Institute for Physiological Sciences, National Institutes of Natural Sciences, Okazaki, Aichi 444-8585, Japan
[6]Phenovance, LLC, Kashiwa, Chiba 277-0882, Japan
[7]Section of Mammalian Transgenesis, Center for Genetic Analysis of Behavior, National Institute for Physiological Sciences, National Institutes of Natural Sciences, Okazaki, Aichi 444-8787, Japan
[8]Division of Behavioral Neuropharmacology, International Center for Brain Science, Fujita Health University, Toyoake, Aichi 470-1192, Japan
[9]Section of Viral Vector Development, Center for Genetic Analysis of Behavior, National Institute for Physiological Sciences, National Institutes of Natural Sciences, Okazaki, Aichi 444-8585, Japan
[10]German Center for Neurodegenerative Diseases (DZNE) Berlin, Berlin, Germany
[11]Neuroscience Research Center (NWFZ), Cluster NeuroCure, Charité-Universitätsmedizin Berlin, corporate member of Freie Universität Berlin and Humboldt-Universität zu Berlin, Berlin, Germany
[12]Helmholtz Innovation Lab BaoBab (Brain Antibody-omics and B-cell Lab), Berlin, Germany
[13]Department of Neurology and Experimental Neurology, Charité-Universitätsmedizin Berlin, corporate member of Freie Universität Berlin and Humboldt-Universität zu Berlin, Berlin, Germany
[14]Centre for Discovery Brain Sciences, University of Edinburgh, Edinburgh, UK
[15]Muir Maxwell Epilepsy Centre, University of Edinburgh, Edinburgh, UK
[16]Division of Molecular and Cellular Pharmacology, Nagoya University Graduate School of Medicine, Nagoya 466-8550, Japan
[17]Lead contact
*Correspondence: fukata.yuko.y1@f.mail.nagoya-u.ac.jp (Y.F.), fukata.masaki.h6@f.mail.nagoya-u.ac.jp (M.F.)
https://doi.org/10.1016/j.celrep.2023.113634

SUMMARY

Neurodevelopmental disorders, such as intellectual disability (ID), epilepsy, and autism, involve altered synaptic transmission and plasticity. Functional characterization of their associated genes is vital for understanding physio-pathological brain functions. *LGI3* is a recently recognized ID-associated gene encoding a secretory protein related to an epilepsy-gene product, LGI1. Here, we find that LGI3 is uniquely secreted from oligodendrocytes in the brain and enriched at juxtaparanodes of myelinated axons, forming nanoscale subclusters. Proteomic analysis using epitope-tagged *Lgi3* knockin mice shows that LGI3 uses ADAM23 as a receptor and selectively co-assembles with Kv1 channels. A lack of *Lgi3* in mice disrupts juxtaparanodal clustering of ADAM23 and Kv1 channels and suppresses Kv1-channel-mediated short-term synaptic plasticity. Collectively, this study identifies an extracellular organizer of juxtaparanodal Kv1 channel clustering for finely tuned synaptic transmission. Given the defective secretion of the LGI3 missense variant, we propose a molecular pathway, the juxtaparanodal LGI3-ADAM23-Kv1 channel, for understanding neurodevelopmental disorders.

INTRODUCTION

Recent advances in whole-exome sequencing and genome-wide association analysis have accelerated the identification of genes and variants associated with neurodevelopmental disorders such as autism spectrum disorder, epilepsy, and intellectual disability (ID).[1–4] Most of the associated genes converge on common functional pathways, such as neurogenesis, chromatin modification, and synaptic function.[5,6] Thus, elucidation of pathophysiological functions of disease-related gene products is an

This is an open access article under the CC BY-NC-ND license (http://creativecommons.org/licenses/by-nc-nd/4.0/).

essential step for understanding the molecular pathways behind the disorders and provides beneficial information for strategies of the molecular diagnosis and treatment.

The neuronal secreted protein LGI1, a member of the LGI family (LGI1–LGI4), and its receptor ADAM22 constitute the epilepsy-related protein complex.[7] Mutations in *LGI1* cause autosomal dominant lateral temporal lobe epilepsy (ADLTE),[8–10] and LGI1 autoantibodies cause autoimmune limbic encephalitis, characterized by adult-onset amnesia and seizures.[11,12] A recent study finds that biallelic *ADAM22* pathogenic variants cause infantile-onset refractory epilepsy with ID.[13] LGI1 and ADAM22 form a *trans*-synaptic heterotetrameric assembly[14] and instruct PSD-95-family membrane-associated guanylate kinases (MAGUKs) to regulate AMPA and NMDA receptors and Kv1 channels.[15,16] In contrast, biallelic mutations in *LGI4* cause arthrogryposis multiplex congenita (AMC) with peripheral nerve hypomyelination,[17,18] and *Lgi4* mutant or knockout (KO) mice exhibit an AMC-like forelimb defect and peripheral nerve hypomyelination.[19–21] Importantly, *Adam22* KO mice show peripheral nerve hypomyelination and multiple seizures,[22–24] exhibiting combined phenotypes of *Lgi1* (epilepsy)[25–27] and *Lgi4* (peripheral nerve hypomyelination) KO mice. *Lgi2* is associated with epilepsy in dogs,[28] and LGI2 is proposed to regulate the development of inhibitory synapses.[29] Recent exome sequencing identified a biallelic *LGI3* missense variant in patients with ID.[30] The physiological and pathological functions of LGI3, however, remain to be elucidated.

Neuronal-glial interactions, such as axo-glial interactions in myelination, are involved in neuronal functions, and their abnormalities have been recognized in neurological disorders.[31] Oligodendrocytes produce myelin sheaths that enwrap neuronal axons in the central nervous system (CNS) and establish discrete functional domains along the axon: the node of Ranvier, paranode, and juxtaparanode (JXP). These membrane domains are associated with distinct ion channel clustering for rapid saltatory conduction: voltage-dependent sodium channels (Nav) at nodes and voltage-dependent potassium channels (Kv1) at JXPs.[32,33] Although glial cells play a critical role in the organization of ion channel domains in the axonal membrane,[32,34] the exact mechanisms and their significance to physiological and pathological processes in the brain remain incompletely understood.

This study defines ID-related LGI3 as an oligodendrocyte-derived extracellular factor that acts at the JXP of myelinated axons through its receptor ADAM23. LGI3-ADAM23 plays an instructive role in juxtaparanodal Kv1 channel clustering for short-term synaptic plasticity.

RESULTS

An ID-related LGI3 missense variant shows the severe secretion defect

To assess the impact of an ID-associated biallelic missense variation (LGI3 Asp331Asn, D331N) (Figure 1A)[30] on LGI3 functions, we built a homology model of the human LGI3 protein based on the crystal structure of human LGI1 (PDB: 5Y31[14]). The modeled structure predicted that Asp331 occurs in the core of the β-propeller structure of the epitempin (EPTP) domain (Figure 1B, left) and interacts with a Ca^{2+} ion together with the other four amino acid residues to stabilize the structure (Figure 1B, right). We then asked whether the LGI3 variant D331N is secreted because the ADLTE-causing variation E383A in LGI1, which disrupts the Ca^{2+} coordination in EPTP, severely impairs its secretion.[14,35] The secretion level of LGI3 D331N from transfected HEK293T cells was greatly decreased as compared to that of wild-type LGI3, showing the similar defect level to that of LGI1 E383A (Figure 1C). This indicates that the ID-related LGI3 variant is dysfunctional and suggests pathological significance of the loss of LGI3 function for ID.

LGI3 is uniquely expressed in oligodendrocytes in the brain

We next investigated the tissue distribution and developmental changes of the LGI3 protein in mice by comparison with those of other LGI family members and the LGI1 receptor family ADAM22/23 (Figures S1A and S1B). Western blotting showed the specific or predominant expression of all the family members tested in the nervous system. LGI3 and ADAM23 were expressed both in the CNS (brain and spinal cord) and the peripheral nervous system (PNS; sciatic nerve) (Figure S1A). We also found that LGI3 was hardly detected in the newborn and neonatal brains and progressively increased during animal maturation up to postnatal day 180 (P180) (Figure S1B).

The cellular distribution of LGI3 in the brain remains controversial, as previous *in situ* hybridization analyses on mouse brain sections showed neuronal expression of *Lgi3*,[36,37] while single-cell transcriptome analyses suggested *Lgi3* expression in mature oligodendrocytes.[38–40] To decisively examine the cell-type expression profile of *Lgi3* in the brain, we performed fluorescent *in situ* hybridization (FISH) analysis of the adult mouse brain and found that *Lgi3*-positive cells (referred to as $Lgi3^+$ cells) were distributed in broad brain regions (Figure 1D; Table S1). Importantly, the double fluorescence labeling of *Lgi3* and *Mbp*, a marker of mature oligodendrocytes, shows that about 90% $Lgi3^+$ cells were Mbp^+ in white matter fiber tracts such as the corpus callosum and the internal capsule of the striatum. Reciprocally, most Mbp^+ cells were $Lgi3^+$ in all brain regions tested (Table S1). In contrast, neither $Lgi1^+$ nor $Lgi2^+$ cells were Mbp^+ in any brain regions tested, confirming their neuronal expression (Figure 1D; Table S1). $Mbp^-/Lgi3^+$ cells were observed in some brain regions (e.g., hippocampal dentate granule cell layer and CA1 pyramidal cell layer) (Figure S1C). To examine how much the neuronal expression contributes to the protein levels of LGI3 in the brain, we prepared mouse primary cortical neuron cultures, which contain a negligible number of mature oligodendrocytes. The LGI3 protein, as well as MBP, was not detectable in any ages of the neuron culture but was readily observed in the brain lysates. In contrast, LGI1, LGI2, and LGI4 were detected both in cultured neurons and brain lysates (Figure 1E). We also found that LGI3 protein was hardly detected in the whole-brain lysate from oligodendrocyte-specific *Lgi3* KO mice ($Lgi3^{LoxP/\Delta E1}$;*Mbp*-Cre) (Figure 1F). These results indicate that oligodendrocytes are the primary source of LGI3 protein in the brain.

LGI3 is clustered at the JXP of myelinated axons

To precisely localize LGI3 protein expression in the brain, we generated *Lgi3* knockin mice harboring the FLAG and hexahistidine tandem tag (referred to as FH tag) at the C terminus of LGI3

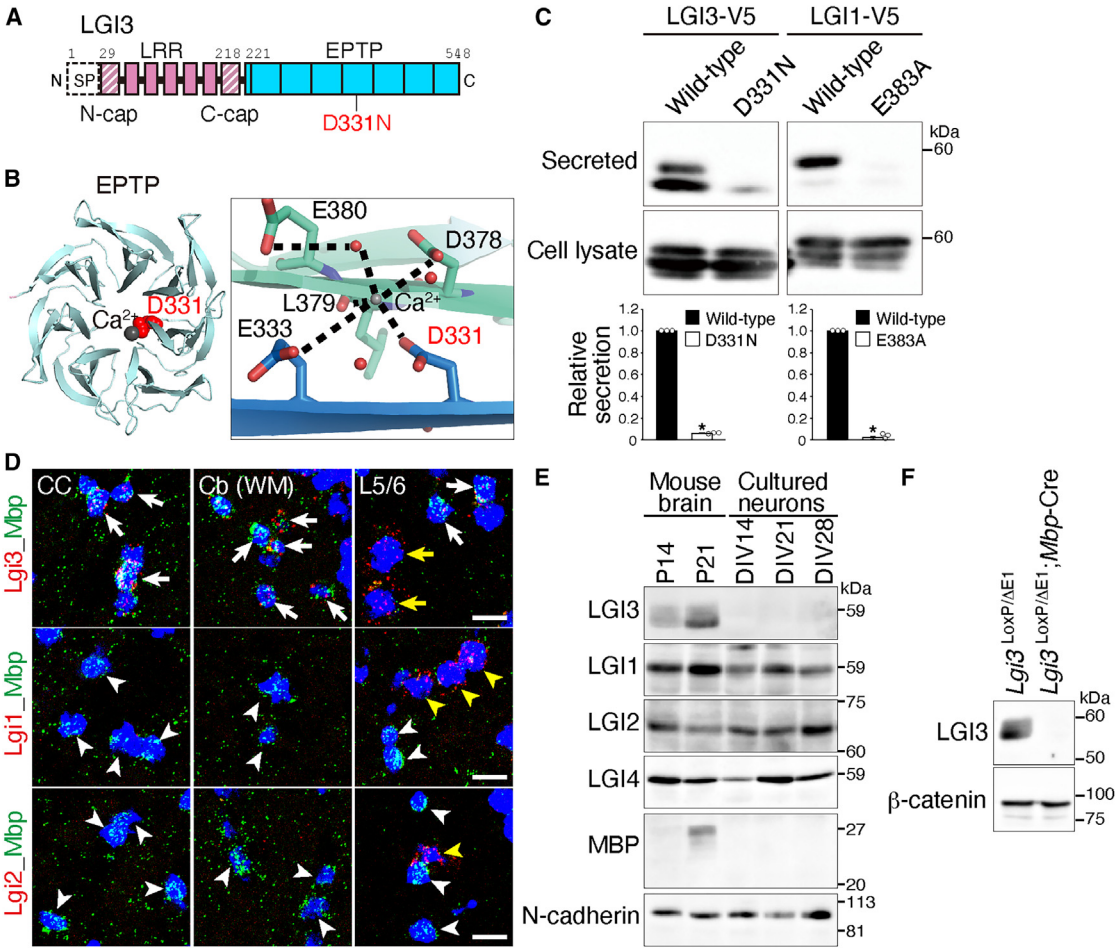

Figure 1. ID-related LGI3 is uniquely expressed in oligodendrocytes

(A) Domain organization of human LGI3. SP, signal peptide; LRR, leucine-rich repeat domain; EPTP, epitempin domain; N- and C-cap, N- and C-terminal cysteine caps in LRR.

(B) Mapping of the ID variant on the modeled LGI3 structure. Left, Asp331 is mapped as red spheres. Right, close-up view of the Ca^{2+}-binding site in the LGI3 EPTP β-propeller. Ca^{2+} and water molecules are shown as gray and red spheres, respectively. Sticks, Ca^{2+}-interacting residues; dotted lines, hydrogen bonds.

(C) Shown are western blots (WBs) of LGIs-V5 in the conditioned medium (secreted) and the cell lysates. Bottom, quantification of the amounts of secreted LGI proteins. n = 3 experiments. Mann-Whitney U test. *$p < 0.05$. Mean ± SD.

(D) Fluorescence *in situ* hybridization (FISH) analysis for *Lgi3*, *Lgi1*, and *Lgi2* expression in the mouse brain (P125). Red, *Lgi3*, *Lgi1*, or *Lgi2*; green, *Mbp*. White arrows, $Mbp^+/Lgi3^+$ cells; yellow arrows, $Mbp^-/Lgi3^+$ cells; white arrowheads, $Mbp^+/Lgi1^-$ or $Mbp^+/Lgi2^-$ cells; yellow arrowheads, $Mbp^-/Lgi1^+$ or $Mbp^-/Lgi2^+$ cells. Nuclear DNA was stained by DAPI (blue). CC, corpus callosum; Cb, cerebellum; WM, white matter; L5/6, cortical layers V and VI. Scale bars, 10 μm.

(E) WB analysis of LGI family proteins in the lysates of the mouse brains and primary cultured cortical neurons. N-cadherin, a loading control. P, postnatal days; DIV, days *in vitro*.

(F) WB analysis of $Lgi3^{LoxP/\Delta E1}$ and $Lgi3^{LoxP/\Delta E1}$;*Mbp*-Cre mouse brain lysates (P35).

See also Figure S1 and Table S1.

($Lgi3^{FH/FH}$ mouse) (Figures 2A and S2A). $Lgi3^{FH/FH}$ mice were viable and did not show detectable developmental defects. Immunohistochemical analysis using anti-FH tag antibody[35] showed that LGI3 was broadly distributed in the myelin-rich regions of the brain such as deeper layers of the cortex, corpus callosum, internal capsule, thalamus, midbrain, medulla, and cerebellar white matter (Figure 2B), where LGI3 largely overlapped with MBP (Figures 2C and S2B). The specificity of experiments was validated by using wild-type mice as a negative control (Figures 2B, 2C, and S2B). Interestingly, double immunofluorescence staining for LGI3-FH and LGI1 revealed their mutually exclusive distribution patterns (Figure 2B): LGI1 was less expressed in the myelin-rich regions but strongly expressed in the cortical and hippocampal neuropil, suggesting their distinct functions in the brain. Consistently, biochemical subcellular fractionation of the mouse brain showed that LGI3-FH in the knockin mouse as well as authentic LGI3 in the wild-type mouse were highly enriched in the myelin fraction like MBP, and only a trace amount of LGI3 was detected in the synaptosomal fraction (Figure 2D).

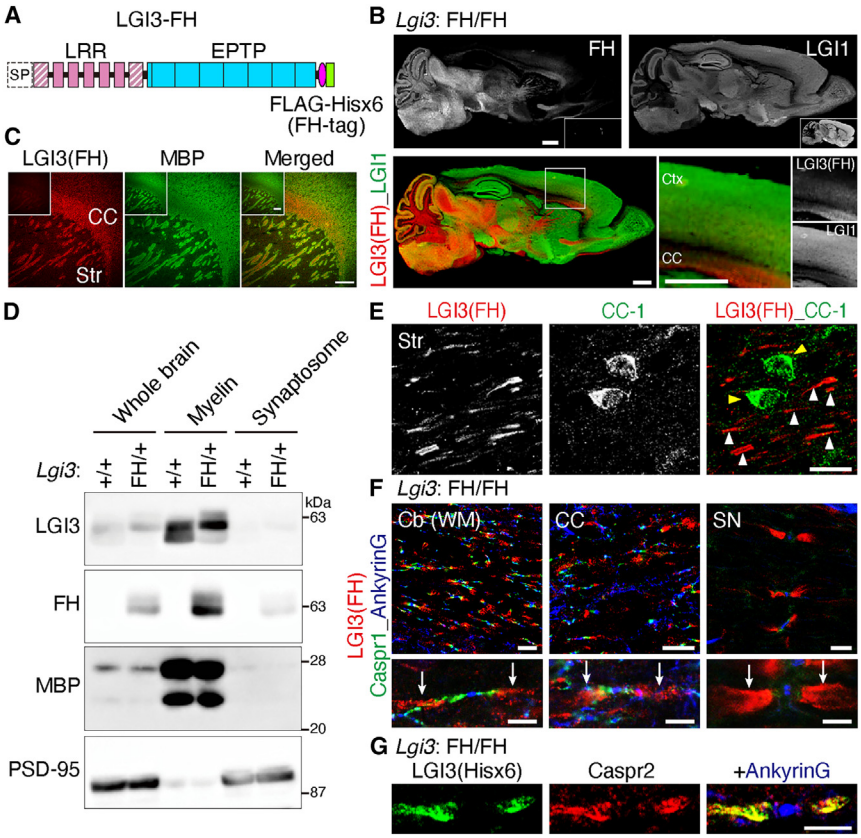

Figure 2. LGI3 is clustered at the JXP of myelinated axons

(A) Schematic image of FLAG-Hisx6 (FH)-tagged LGI3 protein.

(B) Distributions of LGI3-FH (red) and LGI1 (green) in the mouse brain.

(C) LGI3-FH is co-localized with MBP in the subcortical white matter (P166). Insets, wild-type mouse brain.

(D) Biochemical subcellular fractionation of LGI3 in the mouse brain (P34).

(E) LGI3-FH is not detected in the soma of oligodendrocytes in *Lgi3*$^{FH/FH}$ mice (P183). CC-1, cytoplasmic oligodendrocyte marker protein. White arrowheads, LGI3-FH clusters; yellow arrowheads, somata of oligodendrocytes.

(F and G) LGI3 is clustered at the JXP in the mouse brain and sciatic nerves. Sections are triple labeled by antibodies to (F) FH tag (LGI3-FH, red), Caspr1 (green, a paranode marker), and ankyrinG (blue, a node marker);

(G) Hisx6 tag (LGI3-FH, green), Caspr2 (red, a JXP marker), and ankyrinG (blue, in the merged image) in the internal capsule.

Arrows (in F, bottom) indicate LGI3-FH signals at the JXP. CC, corpus callosum; Str, striatum; Cb, cerebellum; WM, white matter; SN, sciatic nerves. P100 mouse tissue sections were used (B, F, and G). Scale bars, 1 mm (B), 250 μm (C), 10 μm (E and F, top), and 5 μm (F, bottom, and G).

See also Figure S2.

A higher-magnification image shows that LGI3-FH labeling was excluded from somata of CC-1^{+} mature oligodendrocytes but specifically appeared in paintbrush-like clusters along the surrounding axonal tract (Figure 2E). To determine the localization of LGI3 along myelinated axons, we co-labeled LGI3-FH with marker proteins for perinodal axonal domains: ankyrinG for nodes of Ranvier, Caspr1 for paranodes, and Caspr2 for JXPs. In the brain and sciatic nerves, LGI3 was found in discrete, micrometer-sized clusters that were flanked by paranodal Caspr1 clusters on one proximal side and segregated from nodal ankyrinG clusters (Figure 2F) and was co-labeled with juxtaparanodal Caspr2 (Figure 2G). Besides the axonal JXP, LGI3 was expressed in the molecular layer and the basket cell terminal (Pinceau) in the cerebellum (Figure S2C). These results indicate that the vast majority of LGI3 proteins expressed in the brain are secreted from oligodendrocytes and accumulated specifically at the JXP of myelinated axons.

LGI3 interacts with ADAM23 family, LGI family, and Kv1 channels in the mouse brain

To comprehensively identify the LGI3-associated protein complexes in the brain, tandem-affinity purification (TAP) of LGI3-FH was performed from *Lgi3*$^{FH/FH}$ mouse brain extracts. To efficiently solubilize proteins in the lipid-rich myelin fraction, we employed the high-stringency buffer condition including 2% Fos-Choline-14.[16] Silver staining of the TAP eluates detected the specific bands purified from *Lgi3*$^{FH/FH}$ mouse brain extracts (Figure 3A). Shotgun proteomics with label-free quantification identified 130 LGI3-associated proteins with significant enrichment (>4-fold enrichment in *Lgi3*$^{FH/FH}$ versus wild-type and $p < 0.05$, 4 replicates), including (1) ADAM11/22/23 family members, (2) LGI family members (LGI1, LGI2, LGI4), (3) Shaker-type voltage-dependent potassium channels (Kv1.x/Kcna, Kvβ2/Kcnab2), (4) PTPR-N family members (PTPR-N, PTPR-N2), transmembrane proteins involved in the secretion process,[41,42] and (5) other transmembrane proteins (Figure 3B; Table S2). Importantly, PSD-95-like MAGUK proteins, which are the major components of the LGI1-associated protein complexes in the brain,[26] were not detected in any replicates. Western blotting confirmed the interactions of LGI3 with ADAM23, ADAM22, and ADAM11 (Figure 3C). ADAM23 showed the highest recovery among the family members, in agreement with its greatest enrichment in label-free quantitative proteomics (Figure 3B). Although the mass spectrometry-based analysis assigned six alpha subunits of Kv1 channels (Kcna1, -2, -3, -4, -6, and -10) (Figure 3B), the unique sets of isoform-specific peptides were detected only from Kv1.1 and Kv1.2 isoforms (Kcna1 and -2) (Table S3). Consistently, Kv1.1 and Kv1.2 were detected by their specific antibodies in the TAP eluates but Kv1.3 and Kv1.4 were not (Figure 3C). Thus, ADAM23 is a predominant receptor for LGI3, and Kv1.1 and Kv1.2 are the main components of Kv1 channels associated with LGI3. Although the well-established protein associations

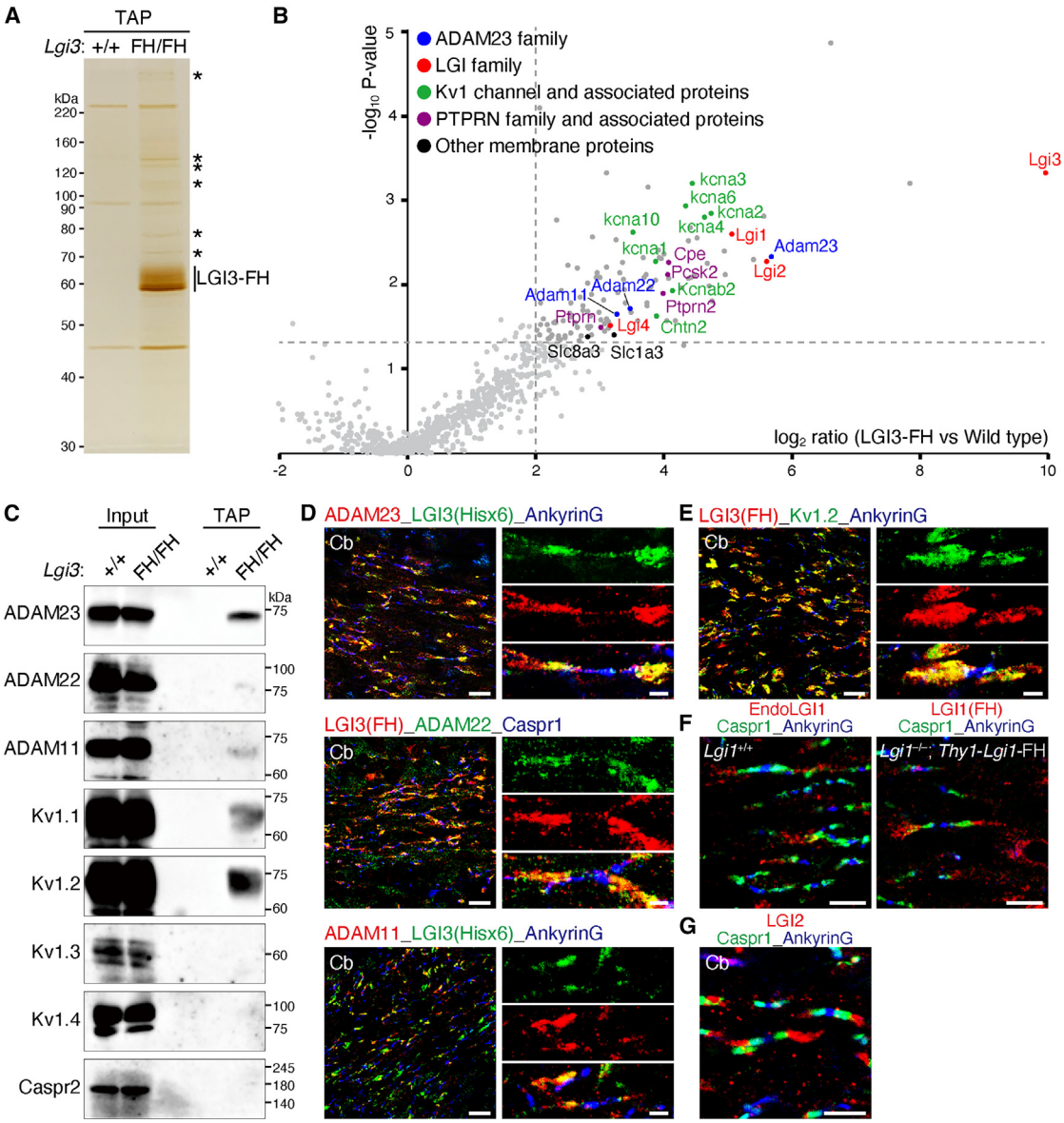

Figure 3. LGI3 interacts with ADAM23 family, LGI family, and Kv1 channel proteins and co-clusters at the JXP in the brain

(A) *In vivo* LGI3-associated protein complex purified from the *Lgi3*$^{FH/FH}$ mouse brain (~P100). Asterisks, specific bands co-purified with LGI3-FH.

(B) LGI3-interacting protein-protein networks in the mouse brain. Thresholds for enrichment are shown by gray dashed lines. Light gray dots, proteins with subthreshold values; gray dots above thresholds, proteins in other categories. All protein data (997 proteins) for the plot are shown in Table S2. n = 2 independent TAP experiments (with two shotgun MS per sample).

(C) Shown are WBs of input and TAP eluates with the indicated antibodies.

(D and E) Co-localization of LGI3 with ADAM23 family proteins and Kv1.2 channels at the JXP.

(F) The endogenous LGI1 protein (endoLGI1) (*Lgi1*$^{+/+}$, left) and neuronally expressed LGI1-FH driven by *Thy1* promoter in an *Lgi1* KO background (*Lgi1*$^{-/-}$;*Thy1-Lgi1*-FH mouse) were detected at the JXP.

(G) Localization of LGI2 at the JXP in the cerebellar white matter (Cb).

P100 (D, E, and G) and P36 (F) mouse brain sections were used. Scale bars, 10 μm (D and E, left), 5 μm (F and G), and 1 μm (D and E, right).

See also Figures S3 and S4 and Tables S2 and S3.

ADAM22-MAGUKs[7,16,43] and Kv1 channel-Caspr2[43,44] were not observed in the LGI3 protein complex under the present condition, we cannot exclude the possibility that our solubilization condition using Fos-Choline-14 may dissociate peripheral interactions of the LGI3 protein complex.

Next, we investigated the mode of interactions of LGI3 with ADAM23 or Kv1 channels. Consistent with previous data,[22] the surface-bound LGI3 was specifically detected when co-expressed with ADAM23 in COS7 cells, showing the interaction of secreted LGI3 with the ectodomain of ADAM23 (Figure S3A).

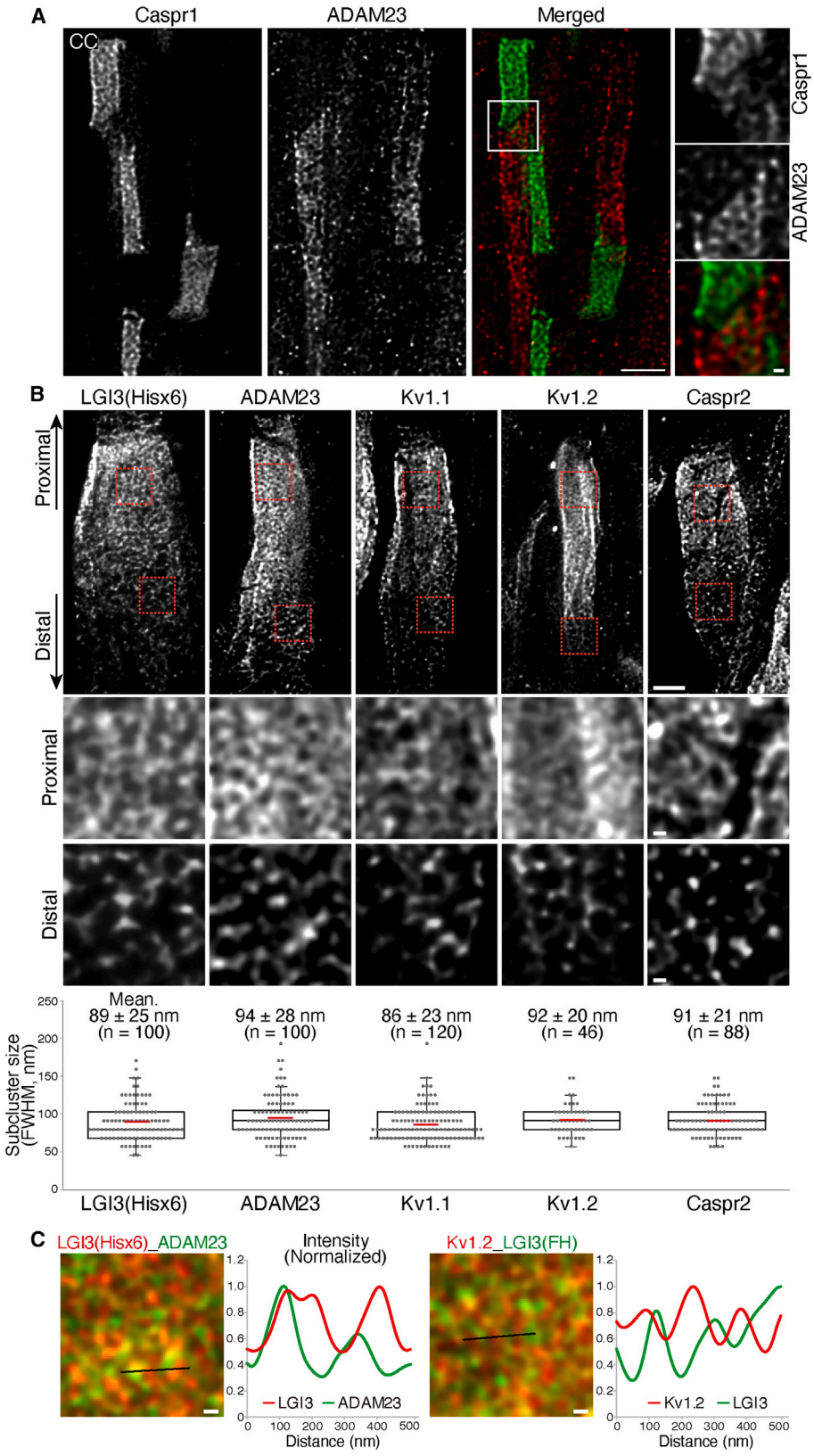

(legend on next page)

Although LGI3 showed less binding activity to ADAM23 than LGI1, their differential binding properties are likely due to the minor amino acid differences between LGI1 and LGI3 in the ADAM22-binding interface previously determined in LGI1 (Figure S3B).[14] In contrast, secreted LGI3 did not bind to the cell-surface-expressed Kv1.1 or Kv1.2 (Figure S3C), suggesting that the association of LGI3 with Kv1 in the brain is indirect and mediated by ADAM23 family proteins. In fact, co-expression of ADAM23 with Kv1.4 showed their co-localization at the cell surface (Figure S3D). Obtained co-localization signals were specific, as no clear co-localization was observed when unrelated membrane-localized proteins, DPP10 or N-cadherin, were expressed instead of Kv1.4 or ADAM23, respectively. Furthermore, we examined whether ADAM23 is recruited into cell surface clusters with Kv1 channels and PSD-95 in heterologous cells as previously shown for ADAM22-Kv1 channel-PSD-93/95 complexes[43] (Figure S3E). When Kv1.4 and PSD-95 were co-expressed in COS7 cells, large plaque-like co-clusters were formed as previously reported,[45] while ADAM23 co-expressed with Kv1.4 or PSD-95 did not form robust clusters. Importantly, ADAM23 was recruited into large surface clusters when co-expressed with Kv1.4 and PSD-95. This co-clustering activity is specific for ADAM23, as N-cadherin was not recruited to the PSD-95-Kv1.4 clusters (Figure S3F). Given that ADAM23 does not have a PDZ-binding motif, the recruitment of ADAM23 into the large surface clusters might be mediated by the direct interaction between ADAM23 and Kv1.4.

LGI3 is co-clustered with ADAM23 family, LGI family, and Kv1 channels at the JXP

We asked whether the identified LGI3-associated proteins, including the ADAM23 family, Kv1 channels, and the LGI family, are indeed co-localized with LGI3 at the JXP. Juxtaparanodal localization of ADAM22 in the PNS and CNS[43] and ADAM23 in the PNS[20] was previously shown. We found that ADAM23, ADAM22, and ADAM11 were co-clustered with LGI3 at the JXP in the myelin-rich regions of the brain (Figures 3D and S4A). LGI3 clusters also occurred with Kv1.2 at the JXP in various brain regions (Figures 3E and S4B). Kv1.1 and Kv1.2 are distributed to multiple axonal domains beyond the JXP, such as the axon initial segment (AIS) and presynaptic terminal in the CNS.[33,43] Similarly, ADAM23 family members occur at the synapse, AIS, and JXP.[20,43,46] In contrast, LGI3 was not evidently observed at the AIS (the ankyrinG-positive region without the flanking Caspr1 signals) (Figure S4C) nor at the synapse-enriched neuropil (Figures 2B, 2C, and S2B), fitting with the fact that synapses and AISs are not covered by oligodendrocyte-produced myelin sheaths.

Consistently with highly specific interactions of LGI family proteins with LGI3 (Figure 3B), we noted that endogenous LGI1 was also detected at the JXP (Figure 3F, left, and S4D), although LGI1 immunoreactivity was relatively weak in myelin-rich regions (Figure 2B). Accordingly, LGI1 was detected in the biochemically fractionated myelin fraction as well as the synaptosomal fraction (Figure S4E). Because *Lgi1* mRNA was not detected in oligodendrocytes (Figure 1D), it is conceivable that LGI1 is synthesized in and secreted by neurons and that a small fraction reaches the JXP. To address this hypothesis, we used the transgenic mouse in which *Lgi1*-FH was driven by the neuron-specific *Thy1* promoter in an *Lgi1* KO background (*Lgi1*$^{-/-}$;*Thy1-Lgi1*-FH).[26] We found that neuronally expressed LGI1-FH was clustered at the JXP (Figure 3F, right). Endogenous LGI2, which is neuronally expressed (Figure 1D), was also labeled at the JXP by the specific antibody (Figures 3G and S4F). These results indicate that LGI proteins derived from both neurons and oligodendrocytes co-occur at the JXP. Therefore, LGI3 is a unique LGI family member that acts predominantly at the JXP in the brain.

LGI3 and its associated proteins form nanoscale subclusters at the JXP

Recent stimulated emission depletion (STED) imaging of the sciatic nerve axons revealed that the nodal and paranodal proteins are finely aligned with a ~190 nm longitudinal periodicity.[47] Periodic organization of Kv1 channels is also observed along the AIS in cultured hippocampal neurons but not at the JXP in sciatic nerves[47] (Figure S5A). Freeze-fracture replica immunogold labeling suggested that juxtaparanodal Kv1 channels form densely packed "rosette"-like clusters in mouse sciatic nerves.[48] We then examined nanoscale organizations of LGI3 and its associated proteins at the JXP with STED imaging. Two-color STED microscopy of the myelinated axons in the corpus callosum visualized clear segregation between Caspr1-labeled regions (paranodes) and ADAM23-labeled regions (JXPs) with their complementary labeling at the transition (Figure 4A), as previously described for neurofascin (paranodes) and Kv1.2 (JXP) in sciatic nerves.[47] Importantly, LGI3 and ADAM23 as well as Kv1 channels were accumulated to form relatively uniform-sized subclusters at the nanoscale (Figure 4B). The average diameter of LGI3 subclusters was ~90 nm in the distal JXP of the myelinated large axons in the medulla (full width at half maximum [FWHM] 89 ± 25 nm, n = 100 subclusters; Figure 4B), and ADAM23 and Kv1 channel subclusters were comparably sized. A representative juxtaparanodal protein, Caspr2, showed essentially similar organizations. LGI3 nanoclusters were more densely detected in the proximal region to paranodes than in the distal region (Figure 4B), and similar nanoscale organizations were observed in various brain regions such as cerebellar white matter, internal capsule, and cortex (Figure S5B). In contrast to the periodic alignment of paranodal proteins previously observed,[47] the nanoclusters of LGI3, ADAM23, and Kv1 channels did not apparently show the ordered alignment,

Figure 4. LGI3 and its associated proteins form nanoscale subclusters at the JXP

(A) Two-color (2C) STED imaging of Caspr1 and ADAM23 at the perinodal axon in corpus callosum (CC).

(B) STED imaging of the large axons in the medulla. Dashed boxes are magnified in the middle two images (proximal and distal). The size of subclusters at the distal JXP is measured (bottom graphs). Red lines represent the mean value. FWHM, full width at half maximum.

(C) 2C STED imaging of the juxtaparanodal proteins.

P100 *Lgi3*$^{FH/FH}$ mouse brain sections were used. Scale bars, 1 μm (A, left, and B, top) and 100 nm (A and B, magnified, and C).

See also Figure S5.

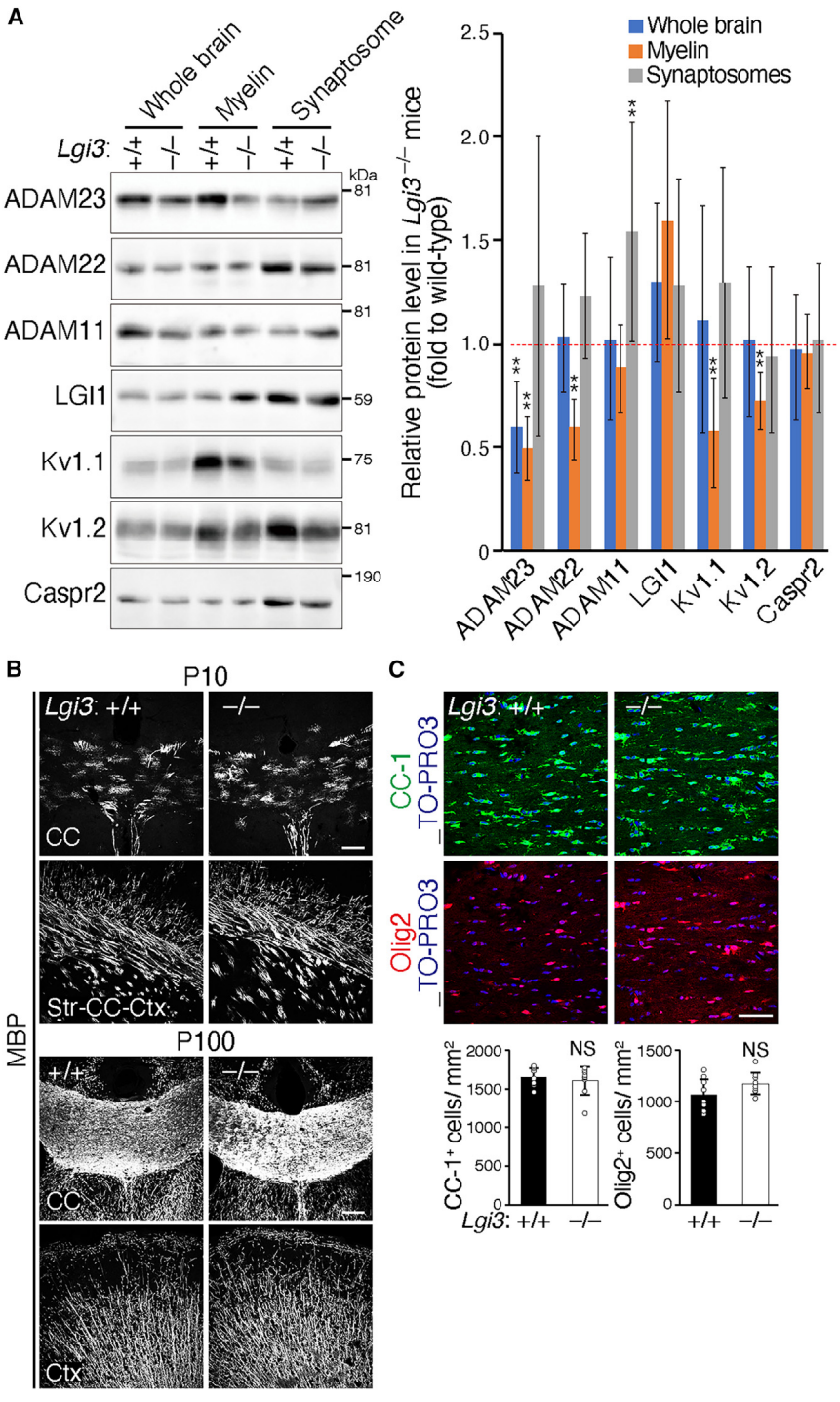

Figure 5. Loss of LGI3 specifically reduces ADAM23, ADAM22, and Kv1 channels in the myelin fraction without affecting myelination

(A) Shown are representative WBs of the whole-brain lysates and subcellular fractions of wild-type ($^{+/+}$) and *Lgi3*$^{-/-}$ mice (~P100) (left). The graph shows protein levels of the *Lgi3*$^{-/-}$ mouse brains relative to those of wild type (right). n = 5 mice per genotype. Mann-Whitney U test. **p < 0.01. Mean ± SD.

(B) Immunostaining for MBP in the neocortex and subcortical regions of the young (P10) and adult (P100) mouse brains. CC, corpus callosum; Str, striatum; Ctx, cortex.

(C) Immunohistochemistry for CC-1 (mature oligodendrocyte marker, green) and Olig2 (expressed throughout the oligodendrocyte lineage, red) in the CC (P50). Nuclear DNA was stained by TO-PRO3 (blue). Bottom, quantification of the number of CC-1^{+} cells and Olig2^{+} cells. n = 3 mice per genotype. Two-tailed Student's t test. NS, not significant. Mean ± SD.

Scale bars, 100 μm (B) and 50 μm (C).

See also Figure S6.

especially in the distal-sparse regions. Two-color STED imaging showed that subclusters of LGI3, ADAM23, and Kv1 channels closely occurred and partially overlapped with each other (Figures 4C and S5C). The present Kv1 channel nanocluster reminiscently represents the juxtaparanodal rosette-like cluster of the sciatic neurons in which six Kv1 channels are tightly packed.[48] It is highly plausible that the LGI3/ADAM23-packed nanoclusters could make close contact with Kv1 rosette clusters at the JXP of the CNS neurons, reflecting their physical interactions.

Loss of LGI3 specifically reduces ADAM23, ADAM22, and Kv1 channels in the myelin fraction without affecting myelination

To investigate the *in vivo* physiological roles of LGI3, we utilized an *Lgi3* mutant mouse harboring a large deletion at the C-terminal region (c.1356_1634del [p.Glu452_Val544del]), which was obtained in the process of generating the *Lgi3*-FH knockin mouse by the CRISPR-Cas9 system (Figure S6A). The LGI3 protein expression was lost in the homozygous mutant mouse brain (Figure S6B). We confirmed the null secretion of the mutant protein from transfected HEK293T cells even if the mutant gene was overexpressed (Figure S6C). Thus, we used this LGI3-null mutant mouse as the *Lgi3* KO mouse (hereafter referred to as *Lgi3*$^{-/-}$ mouse). *Lgi3*$^{-/-}$ mice were viable and fertile with no obvious developmental defects. We examined the protein expression levels in adult mouse brains (~P100) and found a great reduction of protein levels of ADAM23 and ADAM22 in the myelin fraction of *Lgi3*$^{-/-}$ mice (by ~50% and ~40%, respectively), whereas no changes were observed in the synaptosomal fraction (Figure 5A). Importantly, the Kv1 protein levels in the

myelin fraction were also significantly decreased in *Lgi3*$^{-/-}$ mice (by ~30%–40%). The reduction in ADAM23 and Kv1 protein levels was already evident in the younger mouse brain (P30) (Figure S6D). In contrast, loss of LGI3 did not significantly alter protein levels of ADAM11, LGI1, and Caspr2 (Figures 5A and S6D) and did not induce the compensatory mRNA expression of *Lgi1* and *Lgi2* in oligodendrocytes (Figure S6E).

Then, we asked whether myelination and oligogenesis are affected in *Lgi3*$^{-/-}$ mice, as alterations of protein expression predominantly occurred in the myelin fractions. Myelination of the subcortical white matter and the cerebral cortex was indistinguishable between wild-type and *Lgi3*$^{-/-}$ mice through the developmental early stage (P10) to adult (P100) (Figure 5B). Consistently, MBP protein levels in the brain were not significantly different between mouse genotypes (Figure S6F). We also found that the numbers of oligodendrocyte lineage (Olig2^{+} or CC-1^{+} cells) were comparable between genotypes (Figure 5C). These results together suggest that LGI3 deficiency selectively destabilizes the protein complex containing ADAM23, ADAM22, and Kv1 channels in the myelinated neurons without affecting myelination processes.

Loss of LGI3 disturbs ADAM23 and Kv1 channel clustering at the JXP

Then, we investigated whether and how JXP and other axonal domain formations are affected upon loss of LGI3. Immunohistochemical analysis showed that the number and size of paranodal Caspr1 clusters were comparable between wild-type and *Lgi3*$^{-/-}$ mice in the cerebral cortex layers V and VI (L5/6) and corpus callosum (Figures 6A and 6B), suggesting that the paranodal junction was intact in the *Lgi3*$^{-/-}$ mouse brain. In contrast, the number of juxtaparanodal Kv1.1 and Kv1.2 clusters flanked by the paranodal Caspr1 signals was significantly reduced, and the longitudinal cluster length was significantly shortened in the L5/6 of *Lgi3*$^{-/-}$ mice (Figures 6A and S7A) without affecting their fluorescence intensity (Figure S7B). The effects were modest in the corpus callosum, but the length of Kv1.1 clusters was also significantly shortened (Figure 6B). Strikingly, we found a robust reduction in the number of ADAM23 clusters at the JXP in the L5/6 and corpus callosum of *Lgi3*$^{-/-}$ mice (Figure 6C). In contrast, ADAM11 clusters were not significantly affected (Figure 6D). Thus, the reduced clustering of Kv1 channels and ADAM23 at the JXP of the *Lgi3*$^{-/-}$ mice well corresponds to their reduced protein levels in the myelin fraction (Figure 5A). The greater effects on ADAM23 than on Kv1 channels suggest that LGI3 primarily complexes with and stabilizes ADAM23 at the JXP. To examine the role of ADAM23 in Kv1 channel clustering, *Adam23* was knocked out by the CRISPR-Cas9 system via stereotaxic adeno-associated virus (AAV) injection in the brain of Cas9 knockin mice (*Rosa26*$^{Cas9/Cas9}$) (Figures 6F, 6G, and S7C). We found a significant reduction in the juxtaparanodal clustering of LGI3, Kv1.1, and Kv1.2 as well as ADAM23 in *Adam23* KO axons in the cortex. In contrast, there were no significant changes in the number of clusters of the juxtaparanodal proteins in *Adam22* KO axons. These results indicate that the LGI3-ADAM23 complex regulates Kv1 channel clustering at JXPs, although the contribution is different among brain regions. Furthermore, STED microscopy showed that the area covering the Kv1.1 nanocluster distribution at the JXP was significantly reduced in the *Lgi3*$^{-/-}$ mice (Figure 6E) (wild type, 2.86 ± 0.80 μm; *Lgi3*$^{-/-}$ mice, 1.70 ± 0.46 μm n = 18 [wild type] and n = 17 [*Lgi3*$^{-/-}$]; Student's t test: p = 4.6E−6). At present, it is technically difficult with the still-limited resolution of STED microscopy to exactly evaluate the number of nanoclusters, which are densely distributed in small-diameter and randomly oriented CNS axons. However, the size of nanoclusters of Kv1.1 resolved with STED microscopy was not apparently altered in *Lgi3*$^{-/-}$ mice, suggesting that the reduction of juxtaparanodal Kv1.1 clustering is attributed to the decrease in the number of Kv1.1 nanoclusters.

Next, we asked whether the residual clustering of Kv1.1 and ADAM23 at the JXP in *Lgi3*$^{-/-}$ mice depends on other LGI family proteins. Because *Lgi1*$^{-/-}$ mice die within postnatal 3 weeks before adequate myelination,[26] we obtained *Lgi1*$^{+/-}$;*Lgi3*$^{-/-}$ mice, which had a heterozygous *Lgi1* KO allele on the *Lgi3*$^{-/-}$ background. However, no additional effects on the clustering of juxtaparanodal Kv1.1 and ADAM23 were observed in *Lgi1*$^{+/-}$;*Lgi3*$^{-/-}$ mice (Figures S7D and S7E).

LGI3 regulates short-term synaptic plasticity through juxtaparanodal Kv1 channels

Axonal Kv1.1 and Kv1.2 channels regulate the conduction of action potential waveforms to presynaptic terminals.[49–51] This may affect neurotransmitter release and short-term synaptic plasticity.[52,53] We then asked whether the reduction in juxtaparanodal Kv1 channel clustering in *Lgi3*$^{-/-}$ mice affects synaptic properties in response to repetitive presynaptic cell firings. We investigated synaptic transmission of callosally projecting cortical cells in wild-type or *Lgi3*$^{-/-}$ mice. Channelrhodopsin-2 (ChR2) was selectively expressed in L2/3 pyramidal cells (PCs) in the cortex by *in utero* electroporation at embryonic day 15. Whole-cell recordings were obtained from L5 PCs in the contralateral motor cortex of the mouse (P65–P85), while axons of L2/3 callosal neurons expressing ChR2 were stimulated by light illumination to the callosal white matter (Figure 7A, blue circle). When repetitive stimulations were applied in the control mice, synaptic currents evoked by each stimulus were gradually reduced (Figures 7B and 7C; excitatory postsynaptic current [EPSC] amplitude ratio [mean ± SD]: second to first response (2nd/1st), 0.70 ± 0.072; third to first response (3rd/1st), 0.52 ± 0.11), exhibiting short-term depression (STD). Strikingly, the second and third EPSC responses relative to the first response in *Lgi3*$^{-/-}$ mice were significantly higher than in wild-type control (Figures 7B and 7C; ratio: 2nd/1st, 0.95 ± 0.16 and 3rd/1st, 0.88 ± 0.19; Welch's t test [*Lgi3*$^{-/-}$ versus control]: p = 1.4E−5 [2nd/1st] and 1.1E−6 [3rd/1st], respectively), indicating that STD was greatly suppressed in *Lgi3*$^{-/-}$ mice. In addition, we compared synaptic dynamics evoked by light illumination to the center of recording L5 PC soma (soma stimulation) (Figure 7A, green circle), which would include synaptic currents induced by ChR2-mediated direct depolarization of the presynaptic terminals. Although the suppressed STD was observed in the *Lgi3*$^{-/-}$ slices by soma stimulation, the extent of suppression was less than that by white matter stimulation (Figure 7D). Physiological properties of L5 PCs observed in the current-clamp mode were not significantly different between genotypes (Table S4). Taken together, these results suggest that LGI3 plays an essential role in short-term

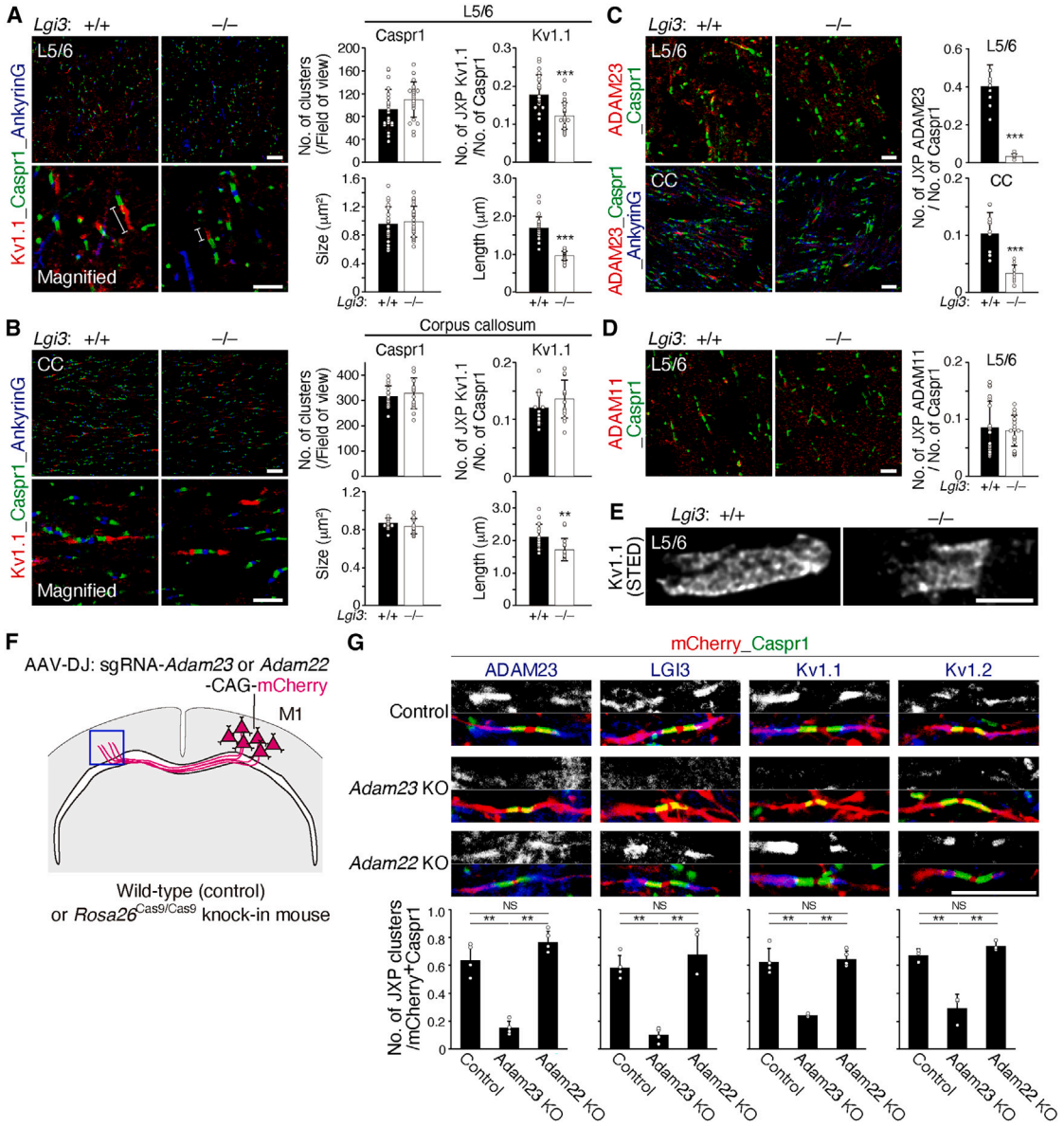

Figure 6. Loss of LGI3 disturbs ADAM23 and Kv1 channel clustering at the JXP

(A and B) Immunohistochemistry for Kv1.1 and axonal domain marker proteins in the L5/6 (A) and CC (B) of the wild-type ($^{+/+}$) and *Lgi3*$^{-/-}$ mice (left). Magnified images are shown at the bottom. The number and size of Caspr1 clusters and the number and length of juxtaparanodal Kv1.1 clusters are quantified (right graphs).

(C and D) The number of ADAM23 clusters at the JXP is significantly reduced in the L5/6 and CC of *Lgi3*$^{-/-}$ mice (C), while that of ADAM11 clusters is not affected (D).

(E) Representative STED images of juxtaparanodal Kv1.1 clustering in the L5/6 of wild-type ($^{+/+}$) and *Lgi3*$^{-/-}$ mice.

(F) Schematic illustration of stereotaxic injection of AAV for *Adam23* family gene KO by the CRISPR-Cas9 system. AAV-DJ-expressing sgRNA for *Adam23* or *Adam22* and a reporter mCherry were injected into the primary motor cortex of *Rosa26*$^{Cas9/Cas9}$ knockin mice (∼P40). Juxtaparanodal cluster formation on the mCherry^{+} axons in the contralateral cortex (blue square) was evaluated at 8 weeks after injection.

(G) Representative images of the juxtaparanodal proteins (grayscale or blue) on the mCherry^{+} (red) axons are shown. The number of juxtaparanodal protein clusters (ratio to Caspr1 clusters, green) was significantly reduced in the *Adam23* KO axons.

(A–E) Wild-type mice, P100–P119; *Lgi3*$^{-/-}$ mice, P100. (A–D) n = 3 mice per genotype. Mann-Whitney U test. **p < 0.01 and ***p < 0.001. Mean ± SD. (G) n = 4 experiments, one-way ANOVA post hoc Tukey's test. NS, not significant. **p < 0.01. mean ± SD. Scale bars, 10 μm (A and B, top), 5 μm (A and B, bottom, C, and D), 1 μm (E), and 10 μm (G).

See also Figure S7.

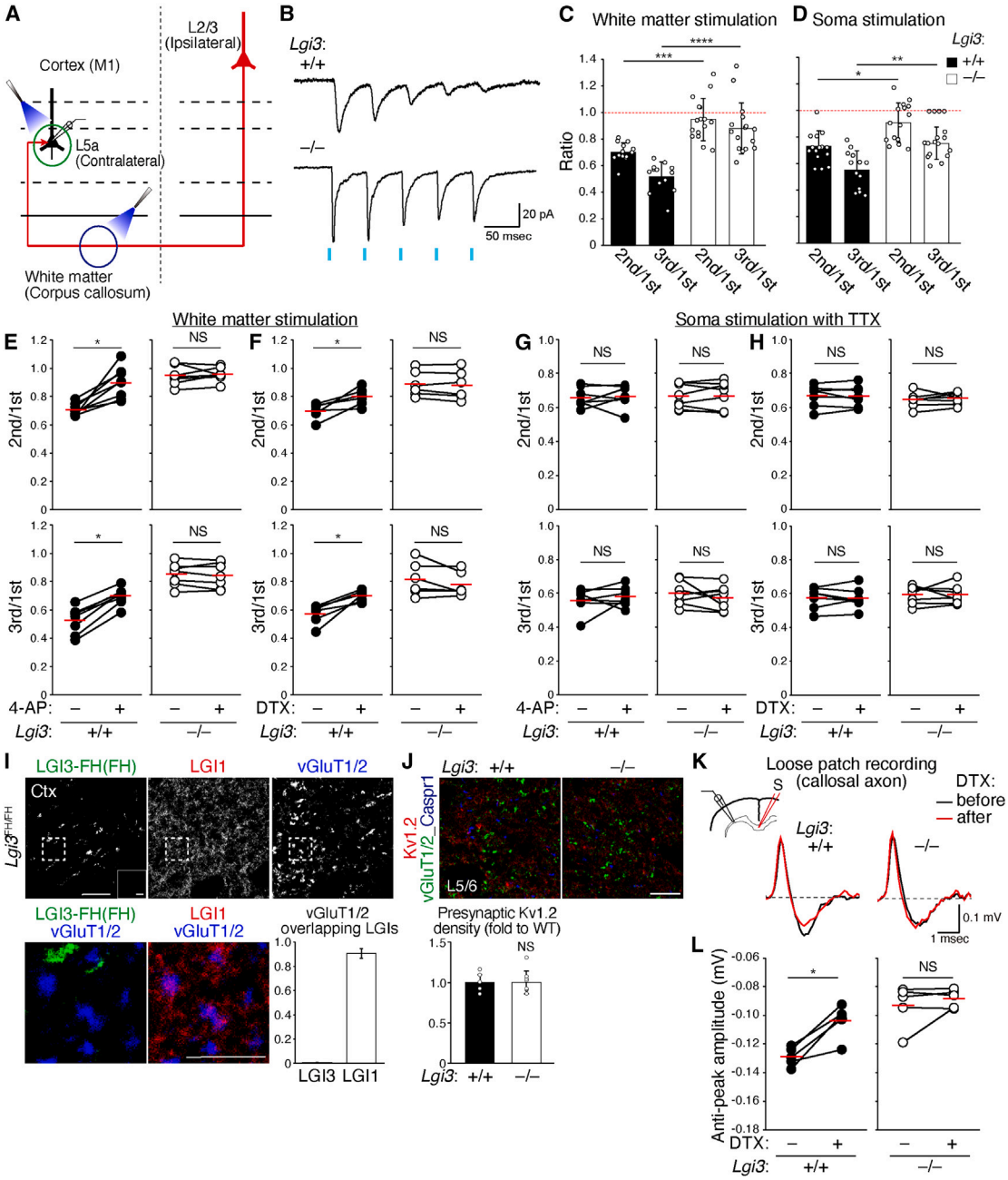

Figure 7. LGI3 regulates short-term synaptic plasticity through juxtaparanodal Kv1 channels

(A) Schematic electrophysiological experiments. Blue and green circles represent light illumination to the white matter and to the center of recording L5a pyramidal cell (PC) soma, respectively.

(B) Representative averaged current trace of L5a PC in response to repetitive stimulations by light illumination (1 ms duration, 20 Hz, light blue bars) to the white matter axons of ChR2^{+} L2/3 callosal neurons.

(C and D) EPSC amplitude ratio (second to first and third to first responses, respectively) of L5a PCs in the wild-type ($^{+/+}$) or *Lgi3*$^{-/-}$ mouse brain slices evoked by white matter (C) or soma stimulation (D). Wild-type, n = 13 and 12; *Lgi3*$^{-/-}$, n = 16 and 15 (white matter and soma stimulation, respectively). Welch's t test. *p < 0.01, **p < 0.001, ***p < 0.0001, and ****p < 0.00001. Mean ± SD.

(E and F) Blockade of Kv1 channels suppresses STD inductions in wild-type but not in *Lgi3*$^{-/-}$ mice. Ratio of EPSC evoked by white matter stimulation before and during bath application of (E) 100 μM 4-AP and (F) 100 nM DTX-I. Wilcoxon signed-rank test. NS, not significant. *p < 0.05.

(G and H) Presynaptic terminals on recorded L5a PCs were directly stimulated by soma stimulation in the presence of 1 μM TTX before and during bath application of 100 μM 4-AP (G) or 100 nM DTX-I (H). Wilcoxon signed-rank test. NS, not significant.

(I) LGI3 is exclusively localized in non-presynaptic regions of the mouse cortex in contrast to LGI1. Dashed white square area is magnified (bottom). Manders co-localization coefficient of vGlut1/2 with LGI3 or LGI1 is shown in the graph. Scale bars, 10 μm (top) and 5 μm (magnified, bottom). n = 3 experiments. Mean ± SD.

(legend continued on next page)

plasticity by regulating action potential waveform conduction over the axon.

Next, to determine whether the suppression of STD in the *Lgi3*$^{-/-}$ brain slice results from the reduced Kv1 channel function at the JXP, we applied potassium channel inhibitors to the bath solutions. In the wild-type controls, application of 4-aminopyridine (4-AP; 100 μM), a broad-spectrum inhibitor of Kv channels, significantly suppressed STD of synaptic currents induced by the repetitive white matter stimulation (Figure 7E, left), showing the comparable effects on STD to that of the loss of LGI3 (Figure 7E, right, 4-AP[−]). In contrast, 4-AP treatment did not affect the synaptic dynamics in the *Lgi3*$^{-/-}$ brain slice (Figure 7E, right). Then, we employed a specific blocker of Kv1.1, Kv1.2, and Kv1.6 subtypes, dendrotoxin-I (DTX-I; 100 nM[54,55]) (Figure 7F). DTX-I showed essentially the same effects as 4-AP: STD suppression in wild-type but not in *Lgi3*$^{-/-}$ brain slices. Thus, LGI3 loss and DTX-I-mediated Kv1 channel blockade similarly suppressed STD, and loss of LGI3 completely canceled the DTX-I inhibitory effects.

To further specify the role of LGI3-Kv1 channel clusters at JXPs separate from presynaptic Kv1 channels, we extracted synaptic events evoked by repetitive stimulations of presynaptic buttons in the soma-stimulation paradigm accompanied by tetrodotoxin (TTX) application (Figures 7G and 7H). Light stimulation of ChR2 in the presence of TTX directly depolarizes the presynaptic terminals under the conditions in which action potential generation and propagation along the stimulated axons are blocked. In the wild-type control slices, STD was induced by soma stimulation in the presence of TTX, and STD inductions were not suppressed by 4-AP or DTX application, indicating that presynaptic Kv1 channels are not involved in the soma-stimulation-induced STD. Importantly, the soma-stimulation-induced STD was similarly observed in *Lgi3*$^{-/-}$ brain slices and was not blocked by 4-AP or DTX treatment. These results strongly suggest that the partial suppression of STD in the soma stimulation of *Lgi3*$^{-/-}$ slices in Figure 7D is not due to the dysfunction of presynaptic Kv1 channels but is rather attributed to the defect in juxtaparanodal Kv1 channel function of distal parts of L2/3 axons within L5 (Figures 7G and 7H). Also, no significant differences in the resting membrane potential, input resistance, spike threshold, spike height, and spike width of L2/3 PCs were found between wild-type and *Lgi3*$^{-/-}$ mice (Table S5), supporting the specific effect of loss of LGI3 on the Kv1 channel function at JXPs. Consistently, LGI3 was neither co-localized with nor apposed to presynaptic vGlut1/2 in the cerebral cortex, whereas LGI1 was co-localized with vGlut1/2 (Figure 7I). These results indicate that LGI3 is not distributed to the presynapse in the cerebral cortex, excluding the possibility that presynaptic Kv1 channels are affected in *Lgi3*$^{-/-}$ mice. We also observed no significant changes in presynaptic Kv1.2 channel densities (Figure 7J) or in vGlut1/2^{+} synapse number (1.00- ± 0.36-fold to wild type, Student's t test: p = 0.99) in the L5/6 cortex of *Lgi3*$^{-/-}$ mice.

Finally, we performed loose-patch recordings from callosal axons and analyzed the waveform of action potentials (Figures 7K and 7L). In the wild-type brain slice, we detected a significant reduction of the repolarization phase of the action potential (anti-peak amplitude) by DTX-I treatment. This result indicates that juxtaparanodal Kv1 channels are involved in the repolarization phase of the action potential as reported.[56,57] In contrast, the repolarization phase of the action potentials was not affected by DTX-I application in the *Lgi3*$^{-/-}$ brain slices, supporting the specific impairment in juxtaparanodal Kv1 channels in *Lgi3*$^{-/-}$ mice. Taken together, we conclude that loss of LGI3 specifically affects juxtaparanodal Kv1 channels separate from non-juxtaparanodal Kv1 channels, leading to alterations in cerebral STD inductions.

Behavioral analysis of *Lgi3*$^{-/-}$ mice

To access the behavioral or cognitive phenotypes of *Lgi3*$^{-/-}$ mice, we investigated the ability of motor coordination and learning by the accelerating rotarod test (Figure S8A) and spatial learning and memory by the Morris water maze task (Figures S8B–S8D). We found no significant difference in both experiments between wild-type and *Lgi3*$^{-/-}$ mice, although *Lgi3*$^{-/-}$ mice showed a tendency to perform lower on the probe test on day 3 of the Morris water maze task (Figure S8C; Student's t test: p = 0.12 [*Lgi3*$^{-/-}$ versus control]).

Then, to further assess the higher cognitive function of *Lgi3*$^{-/-}$ mice, we employed the IntelliCage system, which allows us to test several behavioral tasks sequentially under the grouped-housing condition with limited intervention of experimenters[58] (Figures S8E–S8J). There was no significant difference between wild-type and *Lgi3*$^{-/-}$ mice in exploratory behavior (Figure S8F) or in basal activity (Figure S8G). To investigate the learning ability and behavioral flexibility of *Lgi3*$^{-/-}$ mice, we used a task called SP-FLEX, where the mice could obtain the reward (drinking water) by shuttling between two corners while adapting to its positional shifts[59,60] (Figure S8H). First, in the complete shift (CS)-only task, the rewarding corner pairs were positioned diagonally, and the positions alternated between the two diagonal patterns (Figure S8I). Second, in the complete and partial shift (CS-PS) shuffled task, the rewarding corner pairs were positioned either diagonally or adjacently, which made the task more complicated (Figure S8J). Although *Lgi3*$^{-/-}$ mice tended to require more trials to reach the criterion than wild-type mice both in the middle phases (CS2–4) of the CS-only task and in the beginning phases of the CS-PS shuffled task, no significant differences were observed between genotypes. Thus, under the present

(J) Presynaptic Kv1 channels are not altered in *Lgi3*$^{-/-}$ mice. The intensity of the Kv1.2 is quantified (graph). n = 6 experiments. Two-tailed Mann-Whitney U test. NS, not significant. Mean ± SD. Scale bars, 10 μm.
(K and L) Loose-patch single-axon recordings in the CC.
(K) Inset shows the schematic loose-patch single-axon recording. S, stimulating electrode.
(L) Wilcoxon signed-rank test. NS, not significant. *p < 0.05.
Red lines represent the mean value (E–H and L).
See also Tables S4 and S5.

experimental conditions, we observed no significant behavioral alterations in *Lgi3*$^{-/-}$ mice.

DISCUSSION

This study defines an essential role of the LGI3-ADAM23 complex in Kv1 channel clustering at JXPs in the brain. Previous single-particle, cryoelectron microscopy analysis showed that LGI1-ADAM22 heterodimers further assemble to make a 2:2 or 3:3 higher-order complex.[14] A subsequent study using STED microscopy suggests the *trans*-synaptic role of the LGI1-ADAM22 complex.[16] These findings raise a possible *trans*-configuration of LGI3-ADAM23 at the JXP, bridging the axon and the innermost myelin membranes. Alternatively, LGI3-ADAM23 may function in a *cis* fashion at the axon surface as an extracellular scaffold to stabilize the preexisting Kv1 channel nanoclusters at the JXP. Future higher-resolution microscopy analysis combined with structural analysis will clarify the exact configuration of LGI3-ADAM23 complexes at the JXP.

Because Kv1 channel subfamily members are abundantly and widely expressed in various subcellular locations, such as the synapse, AIS, and JXP,[33] it has been difficult to dissect the specific role of individual Kv1 channel loci in the brain function. The confined action of oligodendrocyte-derived LGI3 at the JXP would specify an essential role of juxtaparanodal Kv1 channel clustering in short-term plasticity. Short-term plasticity including STD contributes to processing information and maintaining the excitation-inhibition balance in the neural circuit,[61] and alterations in short-term plasticity have been observed in neuropsychiatric disease animal models.[52,62–64] Robust alterations in short-term plasticity in *Lgi3*$^{-/-}$ mice may sufficiently cause pathological abnormalities in neural circuits. Reinforcement of (residual) Kv1.1/1.2 functions could represent an intriguing therapeutic strategy for a certain form of neurodevelopmental disorders. Recently developed or proposed Kv1.1/1.2 modulators would have the potential to alleviate such pathogenic conditions.[65–68] Because KO mice of Kv1.1 and Kv1.2 display lethal epilepsy[57,69] and pathogenic variants of Kv1.1 and Kv1.2 cause severe epileptic encephalopathy,[70,71] the specific role of juxtaparanodal Kv1 channels in short-term plasticity has been hidden. Therefore, subcellular-specific analysis of disease-associated proteins may provide useful information to understand the complex pathophysiological mechanisms.

During the revision of this article, another related paper was published in which LGI2/3-ADAM23 regulates juxtaparanodal Kv1 channel clusters and the refractory period in myelinated axons in the peripheral sciatic nerve and spinal cord.[72] Given that biallelic *LGI3* pathogenic variants cause peripheral nerve hyperexcitability as well as moderate ID,[73] these studies are well complementary to each other, providing the potential PNS and CNS pathogenic mechanisms. Clarifying the whole picture of LGI-ADAM-family-related neurological/brain disorders will contribute to discovering additional molecular pathways for brain functioning and therapeutic strategies.

In this study, significant behavioral phenotypes were not detected in *Lgi3* KO mice, although a recent genetic study in humans reported that 16 individuals with loss-of-function variants in LGI3 from eight families display peripheral nerve hyperexcitability syndrome accompanied by mild or moderate ID with complete penetrance.[73] Three possibilities are considered for this discrepancy. First, behavioral paradigms tested were not sensitive enough to detect subtle, mild cognitive abnormalities. Second, our behavioral paradigms might not be suitable to address specific behavioral phenotypes. Third, mice might be more tolerant to loss of LGI3 than humans. In the case of epilepsy-related LGI1, human patients with loss-of-function heterozygous variants in *LGI1* show spontaneous epileptic seizures, whereas heterozygous *Lgi1* KO mice show no spontaneous seizures.[25,26] Further appropriate cognitive tests will clarify the causative relationship between loss of function of LGI3 and ID.

Limitation of the study

We observed the inhibitory effect of DTX-I on repolarization phases of action potentials by the loose-patch recording from wild-type callosal axons but not LGI3-deficient ones (Figures 7K and 7L), suggesting that DTX-I treatment inhibits juxtaparanodal Kv1 channels expressed beneath the myelin sheath. At present, however, we cannot completely exclude the involvement of pools of Kv1 channels other than juxtaparanodal channels, as one study reported only 28% corpus callosum axons are myelinated in the mouse.[74]

The exact mode of interaction between LGI3-ADAM23 and Kv1 channels remains unclear. Previous work showed that LGI1-ADAM22 regulates Kv1 channel expression at the synapse and AIS through the interaction of the cytoplasmic PDZ-binding motif (PBM) of ADAM22 with the PDZ domain of MAGUKs.[16,26,75] In this scenario, MAGUKs serve as the common scaffolding platform for two PBM-containing proteins, ADAM22 and Kv1 channels. In contrast, LGI3-associated protein complexes include abundant Kv1 channels but not MAGUKs (Figure 3), probably because ADAM23, a major receptor for LGI3, does not have the PBM and the present stringent detergent condition may dissociate peripheral Kv1 channel-MAGUK interaction.[43] Our results suggest that LGI3-ADAM23-Kv1 channel association could occur even in the absence of MAGUKs. Given that ADAM23 is recruited into large clusters of Kv1 channel-PSD-95 in COS7 cells (Figure S3E), it is speculated that the LGI3-ADAM23-Kv1 channel complex is co-clustered with MAGUKs at the JXP. Future structural analysis will address whether and how the LGI3-ADAM23 complex interacts with Kv1 channels and MAGUKs.

STAR★METHODS

Detailed methods are provided in the online version of this paper and include the following:

- KEY RESOURCES TABLE
- RESOURCE AVAILABILITY
  - Lead contact
  - Materials availability
  - Data and code availability
- EXPERIMENTAL MODEL AND SUBJECT DETAILS
  - Mice
  - Rat or mouse primary neuronal culture
  - Cell lines

- METHOD DETAILS
  - Plasmid constructions for protein expression in the heterologous cells
  - Secretion test of LGI mutant proteins
  - Generation of *Lgi3*-FH knock-in and *Lgi3* loss-of-function mutant (*Lgi3*$^{-/-}$) mouse
  - Generation of *Lgi1*$^{+/-}$;*Lgi3*$^{-/-}$ mouse
  - Generation of *Lgi3* oligodendrocyte-specific conditional knockout mouse
  - Generation of *Rosa26*-Cas9 knock-in mouse
  - Biochemical analysis of mouse tissue and primary neuron lysates
  - Subcellular fractionation to isolate crude myelin and synaptosomal fractions
  - Tandem affinity purification (TAP) of LGI3-FH from the knock-in mouse brain
  - Mass spectrometry
  - Cell-surface binding assay
  - Cell surface colocalization and co-clustering assay
  - Immunohistochemistry/fluorescence analysis
  - STED superresolution imaging and image analysis
  - Fluorescent *in situ* hybridization (FISH)
  - In utero electroporation
  - Slice experiments
  - Structural protein modeling and sequence alignment
  - AAV vector preparation and infection
  - Stereotaxic injection of AAV vector
  - Animals used for behavioral experiments
  - Rota-rod
  - Morris water maze
  - Behavioral analysis using IntelliCage system
  - Test apparatus (IntelliCage)
  - Experimental setup
  - Exploratory behavior and basal activity
  - Self-paced learning and behavioral flexibility (SP-FLEX) test
- QUANTIFICATION AND STATISTICAL ANALYSIS

SUPPLEMENTAL INFORMATION

Supplemental information can be found online at https://doi.org/10.1016/j.celrep.2023.113634.

ACKNOWLEDGMENTS

We thank Ms. Yumiko Makino (NIBB Trans-Omics Facility) for liquid chromatography-tandem mass spectrometry (LC-MS/MS) analysis; Drs. Nobuhiko Ohno (Jichi Medical University), Norihiko Yokoi (Nagoya Univ), and Hirohide Takebayashi (Niigata Univ) for helpful discussion; Dr. Atsushi Nambu (NIPS) for programming of computer software; Ms. Sanae Hara (NIPS) for technical assistance; RIKEN BRC for providing the transgenic mice; the Center for Animal Resources and Collaborative Study (NIPS) for animal behavioral analysis; and all members of the Fukata laboratory for their kind support. This work was supported by grants from the Ministry of Education, Culture, Sports, Science and Technology (22K15208 to Y.M.; 21K19390 and 22H02723 to Y.F.; and 23H00374, 23H04243, and 23K18228 to M.F.), the Japan Agency for Medical Research and Development (JP21wm0525022 to Y.F. and JP23ek0109649 to M.F.), the Takeda Science Foundation (to Y.F. and M.F.), and a BBSRC, UK grant (BB/T008008/1 to D.M.).

AUTHOR CONTRIBUTIONS

Y.M., Y.F., and M.F. designed research; Y.M. performed biochemical and immunohistochemical experiments; Y.M. and T.O. performed *in utero* electroporation; T.O. performed electrophysiological experiments; Y.M., M.S., and M.H. generated knockin and KO mice; Y.M., Y.Y., T.E., and H.I. performed mouse behavioral experiments; Y.M., H.S., K.K., H.-C.K., D.S., H.P., D.M., Y.F., and M.F. prepared critical reagents/resources; and Y.M., T.O., Y.F., and M.F. drafted the manuscript and all authors revised or commented on it.

DECLARATION OF INTERESTS

T.E. is the founder and researcher at Phenovance, LLC, Japan.

Received: September 9, 2022
Revised: October 31, 2023
Accepted: December 14, 2023
Published: January 8, 2024

REFERENCES

1. Gilman, S.R., Iossifov, I., Levy, D., Ronemus, M., Wigler, M., and Vitkup, D. (2011). Rare de novo variants associated with autism implicate a large functional network of genes involved in formation and function of synapses. Neuron *70*, 898–907.
2. Rees, E., and Owen, M.J. (2020). Translating insights from neuropsychiatric genetics and genomics for precision psychiatry. Genome Med. *12*, 43.
3. Satterstrom, F.K., Kosmicki, J.A., Wang, J., Breen, M.S., De Rubeis, S., An, J.Y., Peng, M., Collins, R., Grove, J., Klei, L., et al. (2020). Large-Scale Exome Sequencing Study Implicates Both Developmental and Functional Changes in the Neurobiology of Autism. Cell *180*, 568–584.e23.
4. Willsey, H.R., Willsey, A.J., Wang, B., and State, M.W. (2022). Genomics, convergent neuroscience and progress in understanding autism spectrum disorder. Nat. Rev. Neurosci. *23*, 323–341.
5. Südhof, T.C. (2008). Neuroligins and neurexins link synaptic function to cognitive disease. Nature *455*, 903–911.
6. Vieira, M.M., Jeong, J., and Roche, K.W. (2021). The role of NMDA receptor and neuroligin rare variants in synaptic dysfunction underlying neurodevelopmental disorders. Curr. Opin. Neurobiol. *69*, 93–104.
7. Fukata, Y., Adesnik, H., Iwanaga, T., Bredt, D.S., Nicoll, R.A., and Fukata, M. (2006). Epilepsy-related ligand/receptor complex LGI1 and ADAM22 regulate synaptic transmission. Science *313*, 1792–1795.
8. Gu, W., Wevers, A., Schröder, H., Grzeschik, K.-H., Derst, C., Brodtkorb, E., de Vos, R., and Steinlein, O.K. (2002). The LGI1 gene involved in lateral temporal lobe epilepsy belongs to a new subfamily of leucine-rich repeat proteins. FEBS Lett. *519*, 71–76.
9. Kalachikov, S., Evgrafov, O., Ross, B., Winawer, M., Barker-Cummings, C., Martinelli Boneschi, F., Choi, C., Morozov, P., Das, K., Teplitskaya, E., et al. (2002). Mutations in LGI1 cause autosomal-dominant partial epilepsy with auditory features. Nat. Genet. *30*, 335–341.
10. Morante-Redolat, J.M., Gorostidi-Pagola, A., Piquer-Sirerol, S., Sáenz, A., Poza, J.J., Galán, J., Gesk, S., Sarafidou, T., Mautner, V.F., Binelli, S., et al. (2002). Mutations in the LGI1/Epitempin gene on 10q24 cause autosomal dominant lateral temporal epilepsy. Hum. Mol. Genet. *11*, 1119–1128.
11. Irani, S.R., Alexander, S., Waters, P., Kleopa, K.A., Pettingill, P., Zuliani, L., Peles, E., Buckley, C., Lang, B., and Vincent, A. (2010). Antibodies to Kv1 potassium channel-complex proteins leucine-rich, glioma inactivated 1 protein and contactin-associated protein-2 in limbic encephalitis, Morvan's syndrome and acquired neuromyotonia. Brain *133*, 2734–2748.
12. Lai, M., Huijbers, M.G.M., Lancaster, E., Graus, F., Bataller, L., Balice-Gordon, R., Cowell, J.K., and Dalmau, J. (2010). Investigation of LGI1 as the antigen in limbic encephalitis previously attributed to potassium channels: a case series. Lancet Neurol. *9*, 776–785.

13. van der Knoop, M.M., Maroofian, R., Fukata, Y., van Ierland, Y., Karimiani, E.G., Lehesjoki, A.E., Muona, M., Paetau, A., Miyazaki, Y., Hirano, Y., et al. (2022). Biallelic ADAM22 pathogenic variants cause progressive encephalopathy and infantile-onset refractory epilepsy. Brain *145*, 2301–2312.

14. Yamagata, A., Miyazaki, Y., Yokoi, N., Shigematsu, H., Sato, Y., Goto-Ito, S., Maeda, A., Goto, T., Sanbo, M., Hirabayashi, M., et al. (2018). Structural basis of epilepsy-related ligand-receptor complex LGI1-ADAM22. Nat. Commun. *9*, 1546.

15. Chen, X., Fukata, Y., Fukata, M., and Nicoll, R.A. (2021). MAGUKs are essential, but redundant, in long-term potentiation. Proc. Natl. Acad. Sci. USA *118*, e2107585118.

16. Fukata, Y., Chen, X., Chiken, S., Hirano, Y., Yamagata, A., Inahashi, H., Sanbo, M., Sano, H., Goto, T., Hirabayashi, M., et al. (2021). LGI1-ADAM22-MAGUK configures transsynaptic nanoalignment for synaptic transmission and epilepsy prevention. Proc. Natl. Acad. Sci. USA *118*, e2022580118.

17. Mishra, S., Rai, A., Srivastava, P., and Phadke, S.R. (2020). A mild phenotype of LGI4-Related arthrogryposis multiplex congenita with intrafamilial variability. Eur. J. Med. Genet. *63*, 103756.

18. Xue, S., Maluenda, J., Marguet, F., Shboul, M., Quevarec, L., Bonnard, C., Ng, A.Y.J., Tohari, S., Tan, T.T., Kong, M.K., et al. (2017). Loss-of-Function Mutations in LGI4, a Secreted Ligand Involved in Schwann Cell Myelination, Are Responsible for Arthrogryposis Multiplex Congenita. Am. J. Hum. Genet. *100*, 659–665.

19. Bermingham, J.R., Jr., Shearin, H., Pennington, J., O'Moore, J., Jaegle, M., Driegen, S., van Zon, A., Darbas, A., Ozkaynak, E., Ryu, E.J., et al. (2006). The claw paw mutation reveals a role for Lgi4 in peripheral nerve development. Nat. Neurosci. *9*, 76–84.

20. Kegel, L., Jaegle, M., Driegen, S., Aunin, E., Leslie, K., Fukata, Y., Watanabe, M., Fukata, M., and Meijer, D. (2014). Functional phylogenetic analysis of LGI proteins identifies an interaction motif crucial for myelination. Development *141*, 1749–1756.

21. Nishino, J., Saunders, T.L., Sagane, K., and Morrison, S.J. (2010). Lgi4 promotes the proliferation and differentiation of glial lineage cells throughout the developing peripheral nervous system. J. Neurosci. *30*, 15228–15240.

22. Ozkaynak, E., Abello, G., Jaegle, M., van Berge, L., Hamer, D., Kegel, L., Driegen, S., Sagane, K., Bermingham, J.R., Jr., and Meijer, D. (2010). Adam22 is a major neuronal receptor for Lgi4-mediated Schwann cell signaling. J. Neurosci. *30*, 3857–3864.

23. Sagane, K., Hayakawa, K., Kai, J., Hirohashi, T., Takahashi, E., Miyamoto, N., Ino, M., Oki, T., Yamazaki, K., and Nagasu, T. (2005). Ataxia and peripheral nerve hypomyelination in ADAM22-deficient mice. BMC Neurosci. *6*, 33.

24. Yokoi, N., Fukata, Y., Okatsu, K., Yamagata, A., Liu, Y., Sanbo, M., Miyazaki, Y., Goto, T., Abe, M., Kassai, H., et al. (2021). 14-3-3 proteins stabilize LGI1-ADAM22 levels to regulate seizure thresholds in mice. Cell Rep. *37*, 110107.

25. Chabrol, E., Navarro, V., Provenzano, G., Cohen, I., Dinocourt, C., Rivaud-Péchoux, S., Fricker, D., Baulac, M., Miles, R., Leguern, E., and Baulac, S. (2010). Electroclinical characterization of epileptic seizures in leucine-rich, glioma-inactivated 1-deficient mice. Brain *133*, 2749–2762.

26. Fukata, Y., Lovero, K.L., Iwanaga, T., Watanabe, A., Yokoi, N., Tabuchi, K., Shigemoto, R., Nicoll, R.A., and Fukata, M. (2010). Disruption of LGI1-linked synaptic complex causes abnormal synaptic transmission and epilepsy. Proc. Natl. Acad. Sci. USA *107*, 3799–3804.

27. Yu, Y.E., Wen, L., Silva, J., Li, Z., Head, K., Sossey-Alaoui, K., Pao, A., Mei, L., and Cowell, J.K. (2010). Lgi1 null mutant mice exhibit myoclonic seizures and CA1 neuronal hyperexcitability. Hum. Mol. Genet. *19*, 1702–1711.

28. Seppälä, E.H., Jokinen, T.S., Fukata, M., Fukata, Y., Webster, M.T., Karlsson, E.K., Kilpinen, S.K., Steffen, F., Dietschi, E., Leeb, T., et al. (2011). LGI2 truncation causes a remitting focal epilepsy in dogs. PLoS Genet. *7*, e1002194.

29. Favuzzi, E., Deogracias, R., Marques-Smith, A., Maeso, P., Jezequel, J., Exposito-Alonso, D., Balia, M., Kroon, T., Hinojosa, A.J., F Maraver, E., and Rico, B. (2019). Distinct molecular programs regulate synapse specificity in cortical inhibitory circuits. Science *363*, 413–417.

30. Froukh, T.J. (2017). Next Generation Sequencing and Genome-Wide Genotyping Identify the Genetic Causes of Intellectual Disability in Ten Consanguineous Families from Jordan. Tohoku J. Exp. Med. *243*, 297–309.

31. Xin, W., and Chan, J.R. (2020). Myelin plasticity: sculpting circuits in learning and memory. Nat. Rev. Neurosci. *21*, 682–694.

32. Rasband, M.N., and Peles, E. (2021). Mechanisms of node of Ranvier assembly. Nat. Rev. Neurosci. *22*, 7–20.

33. Trimmer, J.S. (2015). Subcellular localization of K+ channels in mammalian brain neurons: remarkable precision in the midst of extraordinary complexity. Neuron *85*, 238–256.

34. Buttermore, E.D., Thaxton, C.L., and Bhat, M.A. (2013). Organization and maintenance of molecular domains in myelinated axons. J. Neurosci. Res. *91*, 603–622.

35. Yokoi, N., Fukata, Y., Kase, D., Miyazaki, T., Jaegle, M., Ohkawa, T., Takahashi, N., Iwanari, H., Mochizuki, Y., Hamakubo, T., et al. (2015). Chemical corrector treatment ameliorates increased seizure susceptibility in a mouse model of familial epilepsy. Nat. Med. *21*, 19–26.

36. Herranz-Pérez, V., Olucha-Bordonau, F.E., Morante-Redolat, J.M., and Pérez-Tur, J. (2010). Regional distribution of the leucine-rich glioma inactivated (LGI) gene family transcripts in the adult mouse brain. Brain Res. *1307*, 177–194.

37. Senechal, K.R., Thaller, C., and Noebels, J.L. (2005). ADPEAF mutations reduce levels of secreted LGI1, a putative tumor suppressor protein linked to epilepsy. Hum. Mol. Genet. *14*, 1613–1620.

38. Saunders, A., Macosko, E.Z., Wysoker, A., Goldman, M., Krienen, F.M., de Rivera, H., Bien, E., Baum, M., Bortolin, L., Wang, S., et al. (2018). Molecular Diversity and Specializations among the Cells of the Adult Mouse Brain. Cell *174*, 1015–1030.e16.

39. Zeisel, A., Hochgerner, H., Lönnerberg, P., Johnsson, A., Memic, F., van der Zwan, J., Häring, M., Braun, E., Borm, L.E., La Manno, G., et al. (2018). Molecular Architecture of the Mouse Nervous System. Cell *174*, 999–1014.e22.

40. Zhang, Y., Chen, K., Sloan, S.A., Bennett, M.L., Scholze, A.R., O'Keeffe, S., Phatnani, H.P., Guarnieri, P., Caneda, C., Ruderisch, N., et al. (2014). An RNA-sequencing transcriptome and splicing database of glia, neurons, and vascular cells of the cerebral cortex. J. Neurosci. *34*, 11929–11947.

41. Kubosaki, A., Nakamura, S., Clark, A., Morris, J.F., and Notkins, A.L. (2006). Disruption of the transmembrane dense core vesicle proteins IA-2 and IA-2beta causes female infertility. Endocrinology *147*, 811–815.

42. Nishimura, T., Kubosaki, A., Ito, Y., and Notkins, A.L. (2009). Disturbances in the secretion of neurotransmitters in IA-2/IA-2beta null mice: changes in behavior, learning and lifespan. Neuroscience *159*, 427–437.

43. Ogawa, Y., Oses-Prieto, J., Kim, M.Y., Horresh, I., Peles, E., Burlingame, A.L., Trimmer, J.S., Meijer, D., and Rasband, M.N. (2010). ADAM22, a Kv1 channel-interacting protein, recruits membrane-associated guanylate kinases to juxtaparanodes of myelinated axons. J. Neurosci. *30*, 1038–1048.

44. Horresh, I., Poliak, S., Grant, S., Bredt, D., Rasband, M.N., and Peles, E. (2008). Multiple molecular interactions determine the clustering of Caspr2 and Kv1 channels in myelinated axons. J. Neurosci. *28*, 14213–14222.

45. Kim, E., Niethammer, M., Rothschild, A., Jan, Y.N., and Sheng, M. (1995). Clustering of Shaker-type K+ channels by interaction with a family of membrane-associated guanylate kinases. Nature *378*, 85–88.

46. Kole, M.J., Qian, J., Waase, M.P., Klassen, T.L., Chen, T.T., Augustine, G.J., and Noebels, J.L. (2015). Selective Loss of Presynaptic Potassium Channel Clusters at the Cerebellar Basket Cell Terminal Pinceau in

Adam11 Mutants Reveals Their Role in Ephaptic Control of Purkinje Cell Firing. J. Neurosci. *35*, 11433–11444.

47. D'Este, E., Kamin, D., Balzarotti, F., and Hell, S.W. (2017). Ultrastructural anatomy of nodes of Ranvier in the peripheral nervous system as revealed by STED microscopy. Proc. Natl. Acad. Sci. USA *114*, E191–E199.
48. Rash, J.E., Vanderpool, K.G., Yasumura, T., Hickman, J., Beatty, J.T., and Nagy, J.I. (2016). KV1 channels identified in rodent myelinated axons, linked to Cx29 in innermost myelin: support for electrically active myelin in mammalian saltatory conduction. J. Neurophysiol. *115*, 1836–1859.
49. Foust, A.J., Yu, Y., Popovic, M., Zecevic, D., and McCormick, D.A. (2011). Somatic membrane potential and Kv1 channels control spike repolarization in cortical axon collaterals and presynaptic boutons. J. Neurosci. *31*, 15490–15498.
50. Kole, M.H.P., Letzkus, J.J., and Stuart, G.J. (2007). Axon initial segment Kv1 channels control axonal action potential waveform and synaptic efficacy. Neuron *55*, 633–647.
51. Shu, Y., Yu, Y., Yang, J., and McCormick, D.A. (2007). Selective control of cortical axonal spikes by a slowly inactivating K+ current. Proc. Natl. Acad. Sci. USA *104*, 11453–11458.
52. Crabtree, G.W., Sun, Z., Kvajo, M., Broek, J.A.C., Fénelon, K., McKellar, H., Xiao, L., Xu, B., Bahn, S., O'Donnell, J.M., and Gogos, J.A. (2017). Alteration of Neuronal Excitability and Short-Term Synaptic Plasticity in the Prefrontal Cortex of a Mouse Model of Mental Illness. J. Neurosci. *37*, 4158–4180.
53. Rama, S., Zbili, M., and Debanne, D. (2015). Modulation of spike-evoked synaptic transmission: The role of presynaptic calcium and potassium channels. Biochim. Biophys. Acta *1853*, 1933–1939.
54. Goldberg, E.M., Clark, B.D., Zagha, E., Nahmani, M., Erisir, A., and Rudy, B. (2008). K+ channels at the axon initial segment dampen near-threshold excitability of neocortical fast-spiking GABAergic interneurons. Neuron *58*, 387–400.
55. Sinha, K., Karimi-Abdolrezaee, S., Velumian, A.A., and Fehlings, M.G. (2006). Functional changes in genetically dysmyelinated spinal cord axons of shiverer mice: role of juxtaparanodal Kv1 family K+ channels. J. Neurophysiol. *95*, 1683–1695.
56. Scott, R., Sánchez-Aguilera, A., van Elst, K., Lim, L., Dehorter, N., Bae, S.E., Bartolini, G., Peles, E., Kas, M.J.H., Bruining, H., and Marín, O. (2019). Loss of Cntnap2 Causes Axonal Excitability Deficits, Developmental Delay in Cortical Myelination, and Abnormal Stereotyped Motor Behavior. Cerebr. Cortex *29*, 586–597.
57. Smart, S.L., Lopantsev, V., Zhang, C.L., Robbins, C.A., Wang, H., Chiu, S.Y., Schwartzkroin, P.A., Messing, A., and Tempel, B.L. (1998). Deletion of the K(V)1.1 potassium channel causes epilepsy in mice. Neuron *20*, 809–819.
58. Kiryk, A., Janusz, A., Zglinicki, B., Turkes, E., Knapska, E., Konopka, W., Lipp, H.P., and Kaczmarek, L. (2020). IntelliCage as a tool for measuring mouse behavior - 20 years perspective. Behav. Brain Res. *388*, 112620.
59. Balan, S., Iwayama, Y., Ohnishi, T., Fukuda, M., Shirai, A., Yamada, A., Weirich, S., Schuhmacher, M.K., Dileep, K.V., Endo, T., et al. (2021). A loss-of-function variant in SUV39H2 identified in autism-spectrum disorder causes altered H3K9 trimethylation and dysregulation of protocadherin beta-cluster genes in the developing brain. Mol. Psychiatr. *26*, 7550–7559.
60. Endo, T., Maekawa, F., Võikar, V., Haijima, A., Uemura, Y., Zhang, Y., Miyazaki, W., Suyama, S., Shimazaki, K., Wolfer, D.P., et al. (2011). Automated test of behavioral flexibility in mice using a behavioral sequencing task in IntelliCage. Behav. Brain Res. *221*, 172–181.
61. Blackman, A.V., Abrahamsson, T., Costa, R.P., Lalanne, T., and Sjöström, P.J. (2013). Target-cell-specific short-term plasticity in local circuits. Front. Synaptic Neurosci. *5*, 11.
62. Arguello, P.A., and Gogos, J.A. (2012). Genetic and cognitive windows into circuit mechanisms of psychiatric disease. Trends Neurosci. *35*, 3–13.
63. Deng, P.Y., Sojka, D., and Klyachko, V.A. (2011). Abnormal presynaptic short-term plasticity and information processing in a mouse model of fragile X syndrome. J. Neurosci. *31*, 10971–10982.
64. Kobayashi, K., Takagi, T., Ishii, S., Suzuki, H., and Miyakawa, T. (2018). Attenuated bidirectional short-term synaptic plasticity in the dentate gyrus of Schnurri-2 knockout mice, a model of schizophrenia. Mol. Brain *11*, 56.
65. Chao, O.Y., Marron Fernandez de Velasco, E., Pathak, S.S., Maitra, S., Zhang, H., Duvick, L., Wickman, K., Orr, H.T., Hirai, H., and Yang, Y.M. (2020). Targeting inhibitory cerebellar circuitry to alleviate behavioral deficits in a mouse model for studying idiopathic autism. Neuropsychopharmacology *45*, 1159–1170.
66. Manville, R.W., and Abbott, G.W. (2020). Isoform-Selective KCNA1 Potassium Channel Openers Built from Glycine. J. Pharmacol. Exp. Therapeut. *373*, 391–401.
67. Silverå Ejneby, M., Wallner, B., and Elinder, F. (2020). Coupling stabilizers open KV1-type potassium channels. Proc. Natl. Acad. Sci. USA *117*, 27016–27021.
68. Yang, Y.M., Arsenault, J., Bah, A., Krzeminski, M., Fekete, A., Chao, O.Y., Pacey, L.K., Wang, A., Forman-Kay, J., Hampson, D.R., and Wang, L.Y. (2020). Identification of a molecular locus for normalizing dysregulated GABA release from interneurons in the Fragile X brain. Mol. Psychiatr. *25*, 2017–2035.
69. Brew, H.M., Gittelman, J.X., Silverstein, R.S., Hanks, T.D., Demas, V.P., Robinson, L.C., Robbins, C.A., McKee-Johnson, J., Chiu, S.Y., Messing, A., and Tempel, B.L. (2007). Seizures and reduced life span in mice lacking the potassium channel subunit Kv1.2, but hypoexcitability and enlarged Kv1 currents in auditory neurons. J. Neurophysiol. *98*, 1501–1525.
70. D'Adamo, M.C., Liantonio, A., Rolland, J.F., Pessia, M., and Imbrici, P. (2020). Kv1.1 Channelopathies: Pathophysiological Mechanisms and Therapeutic Approaches. Int. J. Mol. Sci. *21*, 2935.
71. Masnada, S., Hedrich, U.B.S., Gardella, E., Schubert, J., Kaiwar, C., Klee, E.W., Lanpher, B.C., Gavrilova, R.H., Synofzik, M., Bast, T., et al. (2017). Clinical spectrum and genotype-phenotype associations of KCNA2-related encephalopathies. Brain *140*, 2337–2354.
72. Kozar-Gillan, N., Velichkova, A., Kanatouris, G., Eshed-Eisenbach, Y., Steel, G., Jaegle, M., Aunin, E., Peles, E., Torsney, C., and Meijer, D.N. (2023). LGI3/2-ADAM23 interactions cluster Kv1 channels in myelinated axons to regulate refractory period. J. Cell Biol. *222*, e202211031.
73. Marafi, D., Kozar, N., Duan, R., Bradley, S., Yokochi, K., Al Mutairi, F., Saadi, N.W., Whalen, S., Brunet, T., Kotzaeridou, U., et al. (2022). A reverse genetics and genomics approach to gene paralog function and disease: Myokymia and the juxtaparanode. Am. J. Hum. Genet. *109*, 1713–1723.
74. Sturrock, R.R. (1980). Myelination of the mouse corpus callosum. Neuropathol. Appl. Neurobiol. *6*, 415–420.
75. Seagar, M., Russier, M., Caillard, O., Maulet, Y., Fronzaroli-Molinieres, L., De San Feliciano, M., Boumedine-Guignon, N., Rodriguez, L., Zbili, M., Usseglio, F., et al. (2017). LGI1 tunes intrinsic excitability by regulating the density of axonal Kv1 channels. Proc. Natl. Acad. Sci. USA *114*, 7719–7724.
76. Muona, M., Fukata, Y., Anttonen, A.K., Laari, A., Palotie, A., Pihko, H., Lönnqvist, T., Valanne, L., Somer, M., Fukata, M., and Lehesjoki, A.E. (2016). Dysfunctional ADAM22 implicated in progressive encephalopathy with cortical atrophy and epilepsy. Neurol. Genet. *2*, e46.
77. Kornau, H.C., Kreye, J., Stumpf, A., Fukata, Y., Parthier, D., Sammons, R.P., Imbrosci, B., Kurpjuweit, S., Kowski, A.B., Fukata, M., et al. (2020). Human Cerebrospinal Fluid Monoclonal LGI1 Autoantibodies Increase Neuronal Excitability. Ann. Neurol. *87*, 405–418.
78. Zhou, L., Hossain, M.I., Yamazaki, M., Abe, M., Natsume, R., Konno, K., Kageyama, S., Komatsu, M., Watanabe, M., Sakimura, K., and Takebayashi, H. (2018). Deletion of exons encoding carboxypeptidase domain of Nna1

results in Purkinje cell degeneration (pcd) phenotype. J. Neurochem. *147*, 557–572.

79. Niwa-Kawakita, M., Abramowski, V., Kalamarides, M., Thomas, G., and Giovannini, M. (2000). Targeted expression of Cre recombinase to myelinating cells of the central nervous system in transgenic mice. Genesis *26*, 127–129.
80. Ohkawa, T., Fukata, Y., Yamasaki, M., Miyazaki, T., Yokoi, N., Takashima, H., Watanabe, M., Watanabe, O., and Fukata, M. (2013). Autoantibodies to epilepsy-related LGI1 in limbic encephalitis neutralize LGI1-ADAM22 interaction and reduce synaptic AMPA receptors. J. Neurosci. *33*, 18161–18174.
81. Otsuka, T., and Kawaguchi, Y. (2021). Pyramidal cell subtype-dependent cortical oscillatory activity regulates motor learning. Commun. Biol. *4*, 495.
82. Schneider, C.A., Rasband, W.S., and Eliceiri, K.W. (2012). NIH Image to ImageJ: 25 years of image analysis. Nat. Methods *9*, 671–675.
83. Dhaunchak, A.S., Huang, J.K., De Faria Junior, O., Roth, A.D., Pedraza, L., Antel, J.P., Bar-Or, A., and Colman, D.R. (2010). A proteome map of axo-glial specializations isolated and purified from human central nervous system. Glia *58*, 1949–1960.
84. Shi, G., Nakahira, K., Hammond, S., Rhodes, K.J., Schechter, L.E., and Trimmer, J.S. (1996). βSubunits Promote K+ Channel Surface Expression through Effects Early in Biosynthesis. Neuron *16*, 843–852.
85. Manganas, L.N., Wang, Q., Scannevin, R.H., Antonucci, D.E., Rhodes, K.J., and Trimmer, J.S. (2001). Identification of a trafficking determinant localized to the Kv1 potassium channel pore. Proc. Natl. Acad. Sci. USA *98*, 14055–14059.
86. Landry, C.F., Watson, J.B., Kashima, T., and Campagnoni, A.T. (1994). Cellular influences on RNA sorting in neurons and glia: an in situ hybridization histochemical study. Brain Res. Mol. Brain Res. *27*, 1–11.
87. Petreanu, L., Huber, D., Sobczyk, A., and Svoboda, K. (2007). Channelrhodopsin-2-assisted circuit mapping of long-range callosal projections. Nat. Neurosci. *10*, 663–668.
88. dal Maschio, M., Ghezzi, D., Bony, G., Alabastri, A., Deidda, G., Brondi, M., Sato, S.S., Zaccaria, R.P., Di Fabrizio, E., Ratto, G.M., and Cancedda, L. (2012). High-performance and site-directed in utero electroporation by a triple-electrode probe. Nat. Commun. *3*, 960.
89. Otsuka, T., and Kawaguchi, Y. (2008). Firing-pattern-dependent specificity of cortical excitatory feed-forward subnetworks. J. Neurosci. *28*, 11186–11195.
90. Yamagata, Y., Yanagawa, Y., and Imoto, K. (2018). Differential Involvement of Kinase Activity of Ca(2+)/Calmodulin-Dependent Protein Kinase IIalpha in Hippocampus- and Amygdala-Dependent Memory Revealed by Kinase-Dead Knock-In Mouse. eNeuro *5*, ENEURO.0133-0118.2018.

STAR★METHODS

KEY RESOURCES TABLE

REAGENT or RESOURCE	SOURCE	IDENTIFIER
Antibodies		
Rabbit polyclonal anti-ADAM23	Yokoi et al.[35]	N/A
Rabbit polyclonal anti-ADAM23	Abcam	Cat# ab28302; RRID: AB_722575
Rabbit polyclonal anti-ADAM22 (extracellular)	Muona et al.[76]	N/A
Rabbit polyclonal anti-ADAM11	This paper	N/A
Rabbit polyclonal anti-Caspr2	Sigma-Aldrich	Cat# C8737; RRID: AB_2083511
Rabbit polyclonal anti-FH tag (DYKDDDDKGGHHHHHH)	Yokoi et al.[35]	N/A
Rabbit polyclonal anti-LGI2	At l as Antibodies	Cat# HPA017140; RRID: AB_1852833
Rabbit polyclonal anti-LGI3	Fukata et al.[26]	N/A
Rabbit polyclonal anti-LGI4	This paper	N/A
Rabbit polyclonal anti-Olig2	Millipore	Cat# AB9610 RRID: AB_570666
Rabbit polyclonal anti-N-cadherin	Santa Cruz Biotechnology	Cat# sc-7939; RRID: AB_647794
Rabbit monoclonal anti-HA-Tag (Clone C29F4)	Cell Signaling Technology	Cat# 3724; RRID: AB_1549585
Mouse monoclonal anti-ADAM22 (Clone N46/30)	NeuroMab	Cat# 75–083; RRID: AB_10675128
Mouse monoclonal anti-β-catenin (Clone 14)	BD Biosciences	Cat# 610153; RRID: AB_397554
Mouse monoclonal anti-Caspr1 (Clone K65/35)	NeuroMab	Cat# 75-001; RRID: AB_2083496
Mouse monoclonal anti-Caspr2 (Clone K67/25)	NeuroMab	Cat# 75-075; RRID: AB_2245198
Mouse monoclonal anti-APC (Clone CC-1)	Millipore	Cat# OP-80; RRID: AB_2057371
Mouse monoclonal anti-FLAG (Clone M2)	Sigma-Aldrich	Cat# F3165; RRID: AB_259529
Mouse monoclonal anti-Hisx6 (Clone 9F2)	Fujifilm Wako pure chemicals	Cat# 010–21861; RRID: AB_2921308
Mouse monoclonal anti-Kv1.1 (Clone K36/15)	NeuroMab	Cat# 75–105; RRID: AB_2128566
Mouse monoclonal anti-Kv1.2 (Clone K14/16)	NeuroMab	Cat#75-008; RRID: AB_2296313
Mouse monoclonal anti-Kv1.3 (Clone L23/27)	NeuroMab	Cat# 75-009; RRID: AB_2133637
Mouse monoclonal anti-Kv1.4 (Clone K13/31)	NeuroMab	Cat#75-010; RRID: AB_2249726
Mouse monoclonal anti-LGI1	Yokoi et al.[35]	N/A
Mouse monoclonal anti-MBP (Clone 1)	Millipore	Cat# MAB382; RRID: AB_94971
Mouse monoclonal anti-N-Cadherin (Clone 32)	BD Biosciences	Cat#610920; RRID: AB_2077527
Mouse monoclonal anti-PSD-95 (Clone 7E3-1B8)	Thermo Fisher Scientific	Cat# MA1-046; RRID: AB_2092361

(*Continued on next page*)

Continued

REAGENT or RESOURCE	SOURCE	IDENTIFIER
Mouse monoclonal anti-V5 (Clone SV5-Pk1)	Thermo Fisher Scientific	Cat# R960-25; RRID: AB_2556564
Mouse monoclonal anti-HA (Clone 16B12)	Covance	Cat#MMS-101P; RRID: AB_10064068
Rat monoclonal anti-MBP (Clone 12)	Abcam	Cat# ab7349; RRID: AB_305869
Rat monoclonal anti-FLAG (Clone L5)	Novus	Cat# NBP1-06712; RRID: AB_1625981
Guinea pig polyclonal anti-ADAM22	Yokoi et al.[35]	N/A
Guinea pig polyclonal anti-Ankyrin-G	Synaptic Systems	Cat# 386005; RRID: AB_2737033
Guinea pig polyclonal anti-LGI1	Yokoi et al.[35]	N/A
Guinea pig polyclonal anti-vGluT1	Millipore	Cat# AB5905; RRID: AB_2301751
Guinea pig polyclonal anti-vGluT2	Millipore	Cat# AB2251; RRID: AB_2665454
Human recombinant monoclonal anti-LGI1 (clone AB060-110)	Kornau et al.[77]	N/A
Bacterial and virus strains		
Escherichia coli DH5 alpha cells	Takara Bio	Cat# 9057
Escherichia coli, Stellar Competent Cells	Takara Bio	Cat# 636763
Chemicals, peptides, and recombinant proteins		
Papain	Worthington	Cat# LS003126
B-27	Thermo Fisher Scientific	Cat# 17504044
GlutaMax	Thermo Fisher Scientific	Cat# 35050061
Horse serum, heat inactivated	Thermo Fisher Scientific	Cat# 26050088
Fetal bovine serum	Sigma-Aldrich	Cat# 172012
Polyethylenimine	Sigma-Aldrich	Cat# P3143
Rat tail Type I Collagen	Corning	Cat# 354236
DNase I from bovine pancreas Type IV	Sigma-Aldrich	Cat# D5025
Lipofectamine	Thermo Fisher Scientific	Cat# 18324012
Plus reagent	Thermo Fisher Scientific	Cat# 11514015
Poly-D-lysine hydrobromide	Sigma-Aldrich	Cat# P6407
Hoechst 33342	Thermo Fisher Scientific	Cat# H3570
Fos-Choline-14	Anatrace	Cat# F312S
Anti-FLAG M2 affinity gel	Merck Millipore	Cat# A2220
FLAG peptide	Sigma-Aldrich	Cat# F3290
Ni-NTA Agarose	Qiagen	Cat# 30210
Sequencing Grade Modified Trypsin	Promega	Cat# V5113
Critical commercial assays		
RNAscope Fluorescent Multiplex Reagent kit	ACD	320850
RNAscope Target Probe - Mm-Lgi1	ACD	523191
RNAscope Target Probe - Mm-Lgi2	ACD	580991
RNAscope Target Probe - Mm-Lgi3	ACD	446531
RNAscope Target Probe - Mm-Mbp-C2	ACD	451491-C2
RNAscope Duplex Positive Control Probe - Mm PPIB-C1/POLR2A-C2	ACD	321651
RNAscope 2-plex Negative Control Probe	ACD	320751
Deposited data		
Mass spectrometry data	This study	ProteomeXchange: PXD047790 JPOST: JPST002419

(*Continued on next page*)

Continued

REAGENT or RESOURCE	SOURCE	IDENTIFIER
Experimental models: Cell lines		
COS7	ATCC	Cat# CRL-1651
HEK293T	ATCC	Cat# CRL-3216
Rat primary hippocampal neurons	N/A	N/A
Mouse primary cortical neurons	N/A	N/A
Experimental models: Organisms/strains		
Mouse: *Lgi3-FH* knock-in	This paper	N/A
Mouse: *Lgi3* knockout	This paper	N/A
Mouse: *Lgi1* knockout	Fukata et al.[26]	N/A
Mouse: *Thy1–Lgi1-FH* transgenic	Fukata et al.[26]	N/A
Mouse: B57BL/6N	Japan SLC	N/A
Mouse: B6D2F1	Japan SLC	N/A
Mouse: *Actb*-iCre	Zhou et al.[78]	N/A
Mouse: *Rosa26*-LSL-Cas9 knock-in	The Jackson Laboratory	Cat# 026175; RRID: IMSR_JAX:026175
Mouse: *Rosa26*-L-Cas9 knock-in	This paper	N/A
Mouse: *Lgi3*-LoxP	Marafi et al.[73]	MGI: 7331635
Mouse: *Mbp*-Cre transgenic	RIKEN BRC Niwa-Kawakita et al.[79]	Cat# RBRC01461
Oligonucleotides		
Primers for Lgi3-FH knock-in mouse genotyping: Forward: GGCGACAGAAATTTGTACGGTTC Reverse: CCAGGCCCACTTCTTTGTG	This paper	N/A
Primers for Lgi3 knockout mouse genotyping: Forward: GTTCTCAGAAACAGTTTGTGGCTC Reverse: CCACTTCTTTGTGTATGTGTGTG	This paper	N/A
Primers for LGI1 knockout mouse genotyping: WT Forward: CAGATCCTTTGTGAGATCTGGTT KO Forward: AGCGCATCGCCTTCTATCGCCTTC Common Reverse: AGAAGGCTTATCCGAATACATGCC	Fukata et al.[26]	N/A
Primers for Thy-1 LGI1-FH Tg mouse genotyping: Forward: GCTTGACCAGATTCATTGGCGACT Reverse: CTAATGGTGATGGTGATGATGACC	Fukata et al.[26]	N/A
Primers for Actb-iCre mouse genotyping: Forward: AATCAGCCCCTTCCACATGG Reverse: CCGTAAGTTATGTAACGCGG	Zhou et al.[78]	N/A
Primers for Rosa26-LSL-Cas9 knock-in Forward: CTAGGCCACAGAATTGAAAGATCT Reverse: GTAGGTGGAAATTCTAGCATCATCC Wild-type allele: Forward: AAGGGAGCTGCAGTGGAGTA Reverse: CAGGACAACGCCCACACA	This paper	N/A
Primers for Lgi3-LoxP mouse genotyping: Forward: AACTCCAACTGTGGCCGTGCAG Reverse: CCTGTGAGTGTCTACCTAGCC Common Reverse: GGCAGGAGTCTGGTCCATGC	Niwa-Kawakita et al.[79]	N/A
Primers for Mbp-Cre Tg mouse genotyping: Forward: AATGCTTCTGTCCGTTTGCC Reverse: CTACACCAGAGACGGAAATC Internal control: Forward: CTAGGCCACAGAATTGAAAGATCT Reverse: GTAGGTGGAAATTCTAGCATCATCC	RIKEN BRC #BRC01461	N/A

(*Continued on next page*)

Continued

REAGENT or RESOURCE	SOURCE	IDENTIFIER
Recombinant DNA		
pX330	Addgene	Cat# 42230
pX330: mouse Lgi3-exon8-gr#1 for *Lgi3-FH* knock-in (for genome-editing)	This paper	N/A
pCAGGS: LGI1-HA	Fukata et al.[26]	N/A
pCAGGS: LGI1-V5	Fukata et al.[26]	N/A
pCAGGS: LGI2-V5	This paper	N/A
pCAGGS: LGI1-V5 E383A	This paper	N/A
pCAGGS: LGI3-HA	Fukata et al.[26]	N/A
pCAGGS: LGI3-V5	This paper	N/A
pCAGGS: LGI3-V5 D331N	This paper	N/A
pCAGGS: LGI4-V5	This paper	N/A
pCAGGS: ADAM23	Fukata et al.[7]	N/A
pCAGGS: N-cadherin	This paper	N/A
pCAGGS: DPP10-HA	Ohkawa et al.[80]	N/A
pEGFP-N3: Kv1.1-HA	Fukata et al.[26]	N/A
pEF-Bos: Kv1.2-HA	This paper	N/A
pEF-Bos: Kvβ2-myc	Fukata et al.[26]	N/A
pGW: Kv1.4-HA	This paper	N/A
pGW: PSD-95-FLAG	Fukata et al.[7]	N/A
pCAGGS: mCherry	Otsuka et al.[81]	N/A
pCAGGS-ChR2-Venus	Addgene	Cat# 15753
Software and algorithms		
Mascot version 2.6.1	Matrix Science	http://www.matrixscience.com/mascot_support_v2_6.html
Proteome Discoverer software version 2.2	Thermo Fisher Scientific	https://www.thermofisher.com/store/products/OPTON-30945#/OPTON-30945
Leica LAS AF	Leica Microsystems	https://www.leica-microsystems.com/
Leica Application Suite X	Leica Microsystems	https://www.leica-microsystems.com/
Carl Zeiss ZEN software	Carl Zeiss	https://www.zeiss.com/microscopy/us/home.html
Image Studio	LI-COR	https://www.licor.com/bio/jp/
Image Studio Lite	LI-COR	https://www.licor.com/bio/jp/
Fiji/ImageJ	Schneider et al.[82]	https://imagej.net/software/fiji/
PyMOL	Schrödinger, LLC	https://pymol.org/2/
Axograph	AxoGraph	https://axograph.com/
Ekuseru-Tokei 2012 software	BellCurve	https://bellcurve.jp/
ClustalW2	EMBL-EBI	https://www.ebi.ac.uk/Tools/msa/clustalw2/
Igor Pro 9	WaveMetrics	https://www.wavemetrics.com/

RESOURCE AVAILABILITY

Lead contact

Further information and requests for resources and reagents should be directed to and will be fulfilled by the Lead contact, Masaki Fukata (fukata.masaki.h6@f.mail.nagoya-u.ac.jp).

Materials availability

All unique/stable reagents generated in this study are available from the Lead contact upon reasonable request.

Data and code availability

- The raw mass spectrometry data have been deposited to the ProteomeXchange Consortium (http://www.proteomexchange.org/) via the jPOST partner repository (https://repository.jpostdb.org/) with the accession numbers: PXD047790 for ProteomeXchange and JPST002419 for jPOST.
- This paper does not report original code.
- Any additional information required to reanalyze the data reported in this work paper is available from the Lead contact upon request.

EXPERIMENTAL MODEL AND SUBJECT DETAILS

Mice

Mouse strains used in this study include: *Lgi3*-FH knock-in (generated in the present study), *Lgi3* KO (generated in the present study), *Lgi1* KO,[26] *Thy1-Lgi1*-FH transgenic,[26] *Lgi3*-LoxP[72,73] (MGI: 7331635), *Mbp*-Cre transgenic (RIKEN BRC), *Rosa26*-LSL-Cas9 knock-in (The Jackson Laboratory), and *Actb*-iCre knock-in mice,[78] and C57BL/6N and B6D2F1 female mice (Japan SLC). They were bred and maintained in the animal facility of National Institute for Physiological Sciences. There was no randomization of mice before analysis, and the mice used in this study were selected based purely on availability including male and female mice (except for female mice to obtain embryonic mice and obtain fertilized eggs). Genotyping was performed using PCR primers as listed in Key resources table. All animal studies were reviewed and approved by the ethics committees at National Institutes of Natural Sciences and were performed according to the institutional guidelines concerning the care and handling of experimental animals.

Rat or mouse primary neuronal culture

Primary hippocampal neurons were obtained from rat embryos at embryonic day 19 and seeded onto poly-L-lysine–coated 12 mm coverslips in 24-well plates in neurobasal medium supplemented with B-27 and 2 mM glutamax and 10% fetal bovine serum. After 3-h incubation, the media was changed to neurobasal medium supplemented with 2 mM glutamax and B-27.

Mouse cortical neurons were prepared from mouse embryos at embryonic day 16–17 and seeded onto 0.1% polyethylenimine and 50 μg/mL collagen I–coated 12-well plates.

Cell lines

HEK293T and COS7 cells were cultured in Dulbecco's modified Eagle's medium containing 10% fetal bovine serum. Cells were transfected using Lipofectamine plus (Thermo Fisher Scientific).

METHOD DETAILS

Plasmid constructions for protein expression in the heterologous cells

The cDNAs of rat *Lgi1* (NM_145769), mouse *Lgi2* (NM_001310604.1), rat *Lgi3* (NM_001107277), mouse *Lgi4* (NM_144556.2), rat *Kcna1* (Kv1.1, NM_173095.3), rat *Kcna2* (Kv1.2, NM_012970.3), rat *Kcnab2* (Kvβ2, NM_017304.2) and mouse *Adam23* (NM_011780.3) were cloned from rat or mouse brain total RNA by RT-PCR. The cDNAs encoding rat *Lgi1* (residues 1–557) with 3′UTR, mouse *Lgi2* (residues 1–542), rat *Lgi3* (residues 1–548), and mouse *Lgi4* (residues 1–537) tagged with V5 or HA, mouse *Adam23* (non-tag), mouse *Cdh2* (N-cadherin), and human *DPP10* tagged with HA were subcloned into the pCAGGS vector. Rat *Kcna1* (Kv1.1) tagged with HA was subcloned into the pEGFP-N3 vector (EGFP is not expressed). Rat *Kcna2* (Kv1.2) tagged with HA and rat *Kcnab2* (Kvβ2) tagged with Myc-tag were subcloned into pEF-BOS vector. Rat *Kcna4* (Kv1.4) extracellularly tagged with HA and rat *Dlg4* (PSD-95) tagged with FLAG were subcloned into pGW vector. Indicated mutations were introduced by site-directed mutagenesis. All PCR products were analyzed and confirmed by DNA sequencing.

Secretion test of LGI mutant proteins

cDNAs for wild-type or variants of LGI proteins were transfected into HEK293T cells. At 24 h after transfection, cells were washed with serum-free DMEM and cultured for an additional 24 h under serum-free conditions. Cell lysates and conditioned media were analyzed by Western blotting. For Western blotting, chemical luminescent signals were detected with a cooled CCD camera (the FUSION Solo system, Vilber-Lourmat).

Generation of *Lgi3*-FH knock-in and *Lgi3* loss-of-function mutant (*Lgi3*$^{-/-}$) mouse

To generate the *Lgi3*-FH knock-in mouse, the single guide RNA (sgRNA) target sequence of mouse *Lgi3* (NM_145219), 5′-ACTGGTGTACCGACATGTTG-3' (sgRNA#1), was subcloned into the pX330 (Addgene 42230) vector, which expresses Cas9 and sgRNA. For a homology-directed repair (HDR) template DNA, the ∼1.5 kb homology sequence flanking each side of the target sequence for mouse *Lgi3* was isolated by genomic PCR, and then the sequence encoding FH tag (5′-GGATCCGAATTCGACTACAAGGATGACGACGACAAGGGAGGTCATCATCACCATCACCAT-3′) was inserted after the nucleotide position 1644 of the mouse *Lgi3* coding sequence. This corresponds to the position just after the last amino acid of Ala548 in the mouse LGI3. This template was identical to the corresponding *Lgi3* locus, except for four silent mutations (CGA CAT GTT GTG ->CGG CAC GTG GTC) to prevent the gene editing

by the same sgRNA#1. The pX330 plasmid harboring sgRNA#1 and the linearized HDR template DNA were co-injected into fertilized eggs, collected from superovulated B6D2F1 female mice (F1 hybrid between C57BL/6N and DBA/2) mated with C57BL/6N male mice. To select the desired founder mice, obtained F0 pups were screened by the genomic PCR analysis and subsequent direct sequencing analyses using primer pairs located outside the homology arms. Besides the *Lgi3*-FH knock-in mouse, a mouse harboring an allele with an in-frame deletion (c.1356_1634del, p.Glu452_Val544del) in the last exon (exon 8) of *Lgi3* was also selected as a candidate for a loss-of-function mutant mouse (*Lgi3*$^{-/-}$ mouse). Then, the founder mice harboring the knock-in or deletion allele were back-crossed with C57BL/6N mice. No genomic integration of the Cas9-cassette was confirmed by genomic PCR.

Generation of *Lgi1*$^{+/-}$;*Lgi3*$^{-/-}$ mouse

Lgi1 heterozygous KO mice (*Lgi1*$^{+/-}$)[26] were crossbred with *Lgi3*$^{-/-}$ mice to generate the *Lgi1*$^{+/-}$;*Lgi3*$^{+/-}$ mouse. The obtained *Lgi1*$^{+/-}$;*Lgi3*$^{+/-}$ mice were bred with *Lgi3*$^{-/-}$ mice to generate *Lgi1*$^{+/-}$;*Lgi3*$^{-/-}$ mice. *Lgi1*$^{+/-}$;*Lgi3*$^{-/-}$ mice are viable with no obvious developmental defects.

Generation of *Lgi3* oligodendrocyte-specific conditional knockout mouse

Lgi3-LoxP mouse in which two LoxP sites were inserted upstream and downstream of the first exon was previously generated using a standardized gene recombination approach.[72,73] Oligodendrocyte-specific deletion of *Lgi3* gene was achieved by crossing the *Lgi3*$^{LoxP/+}$ mouse with *Mbp*-Cre transgenic driver mouse in which Cre recombinase was expressed by *Mbp* promotor (RIKEN BRC[79]) generating *Lgi3*$^{LoxP/+}$;*Mbp*-Cre offspring. *Lgi3*$^{LoxP/+}$;*Mbp*-Cre mice were cross-bred with *Lgi3*$^{LoxP/+}$ or *Lgi3*$^{LoxP/LoxP}$ mice obtained from intercrossed *Lgi3*$^{LoxP/+}$ mice breeding. We noticed that germline or early developmental recombination occurred in the offspring leading to the deletion of one of the floxed exon 1 (ΔE1) and resulting in *Lgi3*$^{LoxP/\Delta E1}$. Thus, we used littermates of *Lgi3*$^{LoxP/\Delta E1}$;*Mbp*-Cre and *Lgi3*$^{LoxP/\Delta E1}$ (control) for the experiments to examine whether LGI3 is mainly expressed in oligodendrocytes in the mouse brain (Figure 1F).

Generation of *Rosa26*-Cas9 knock-in mouse

Rosa26-LSL-Cas9 knock-in mice which have a floxed-STOP cassette preventing expression of the downstream bicistronic sequences of Cas9 and EGFP in *Rosa26* locus (The Jackson Laboratory) were cross-bred with *Actib*-iCre knock-in mice (Cre recombinase is expressed under the control of the human beta-actin gene promoter)[78] to delete floxed-STOP cassette and systematically express Cas9 gene (*Rosa26*$^{Cas9/+}$;*Actb*-iCre). *Actib*-iCre allele was removed by intercrossing for maintaining the mouse colony and *Rosa26*-L-Cas9 knock-in mice (*Rosa26*$^{Cas9/Cas9}$) were used for the experiments.

Biochemical analysis of mouse tissue and primary neuron lysates

Mouse tissues and organs were dissected and homogenized in 4 volumes of buffer H [20 mM Tris-HCl (pH8.0), 2 mM EDTA, 320 mM sucrose, 200 μg/mL PMSF]. Mouse cortical neuron lysates were collected with buffer A [10 mM PBS (pH7.5), 5 mM EDTA, 4% SDS, 100 μg/mL PMSF]. Protein concentration was determined by the BCA protein assay (Thermo Fisher Scientific). For comparison of protein levels, equal amounts of protein were subjected to Western blotting.

Subcellular fractionation to isolate crude myelin and synaptosomal fractions

Subcellular fractionation of the mouse brain was performed according to well-established discontinuous sucrose density gradient protocols.[83] Mouse brains were homogenized in 3 volumes of buffer containing 10 mM HEPES (pH7.4), 2 mM EDTA, 320 mM sucrose, 200 μg/mL PMSF on ice with the Potter homogenizer. The molarity of homogenate was adjusted to 1.25 M sucrose, by the addition of 2.0 M sucrose containing 10 mM HEPES (pH7.4). Homogenate was then layered with 1.0 and 0.32 M sucrose containing 10 mM HEPES (pH7.4). After a 100,000 g overnight centrifugation at 4°C, the 0.32/1.0 M interface (crude myelin fractions) and 1.0/1.25 M interface (crude synaptosomal fractions) were collected. Each fraction was re-homogenized and protein concentrations were determined by the BCA protein assay. Twenty μg of proteins of each fraction was analyzed by Western blotting.

Tandem affinity purification (TAP) of LGI3-FH from the knock-in mouse brain

LGI3-FH was purified from the *Lgi3*$^{FH/FH}$ mouse brain as previously described[26] with some modifications. Whole brains from three wild-type or *Lgi3*$^{FH/FH}$ mice (P100-102) were homogenized in buffer H at 4°C. After centrifugation at 20,000 g for 1 h, the pellets (crude membrane fraction) were resuspended and incubated for 1 h in extraction buffer [20 mM Tris-HCl (pH 8.0), 2 mM EDTA, 150 mM NaCl, 50 μg/mL PMSF] containing 2% Fos-Choline-14 (FC-14, Anatrace). After centrifugation at 100,000 g for 1 h, the supernatant was incubated with anti-FLAG M2 agarose. The first eluate was obtained with 20mM Tris-HCl (pH 7.5) buffer containing 150mM NaCl, 1% Triton X-100, 20 mM imidazole, and 0.25 mg/mL FLAG peptide. The eluate was mixed with Ni-NTA beads, and the second eluate was obtained with 20 mM Tris-HCl (pH 7.5) buffer containing 150 mM NaCl, 0.5% Triton X-100, and 250 mM imidazole. The purified proteins were separated by SDS-PAGE, and subjected to silver staining or Western blotting.

Mass spectrometry

The proteins in the TAP eluates from the wild-type and *Lgi3*$^{FH/FH}$ mouse brains were concentrated by Trichloroacetic acid/acetone precipitation and redissolved in the denaturing buffer containing 7 M guanidine hydrochloride, 0.5M Tris-HCl (pH 8.5), and 10 mM

EDTA. Then, proteins were reduced with dithiothreitol and alkylated with iodoacetamide, concentrated, and digested with trypsin at 37°C overnight (in-solution digestion). The obtained peptides were separated via nano-flow liquid chromatography (EASY-nLC1000, Thermo Fisher Scientific) using a reverse-phase C18 column (0.075 Å~ 125 mm; Nikkyo Technos). The liquid chromatography eluent was coupled to a nano ion spray source attached to an Orbitrap Elite mass spectrometer (Thermo Fisher Scientific). For shot-gun analysis including protein identification, label-free quantification, and volcano plot analyses, we used the Mascot2.6.1 (Matrix Science) and Proteome Discoverer2.2 software (Thermo Fisher Scientific). Two biological replicates (two sets of purifications) were injected twice on the mass spectrometer to obtain four technical replicates. Peptide and protein identifications were calculated with protein false discovery rate (FDR) < 0.01. No filtering was applied and obtained protein lists with a high FDR confidence (<0.01) from control and *Lgi3*$^{FH/FH}$ replicates were used for statistical analysis to compare protein abundances based on peak intensity. To make the volcano plots, keratins and trypsin were excluded from the list. Analyses were supported by NIBB Trans-Omics Facility.

Cell-surface binding assay

COS7 cells were seeded onto three poly-*d*-lysine coated 12-mm coverslips in each well of a 6-well plate (2x10^5 cells/well) and co-transfected with LGI1-V5 or LGI3-V5 with ADAM23. At 24 h after transfection, the surface-bound LGIs-V5 were live-stained with the anti-V5 antibodies for 30 min at 37°C. Then, the cells were fixed with 4% paraformaldehyde/120 mM sucrose/100 mM HEPES (pH 7.4) at room temperature (RT) for 10 min and blocked with PBS containing 10 mg/mL BSA for 10 min on ice. The surface-bound LGIs-V5 were visualized with Alexa Fluor 488-conjugated secondary antibodies. Then, fixed cells were permeabilized with 0.1% Triton X-100 and incubated with anti-ADAM23 for total ADAM23 staining, followed by Cy3-conjugated secondary antibodies and Hoechst33342 (Invitrogen). To examine the direct interaction of LGI3 with Kv1.1 or Kv1.2, COS7 cells were cotransfected with LGI3-V5, Kv1.1, and Kvβ2 or LGI3-HA, Kv1.2, and Kvβ2. Kvβ2 promotes the surface expression of Kv1 channels.[84] Surface-expressed Kv1.1 and surface-bound LGI3-V5 were live-stained with anti-Kv1.1 and anti-V5 antibodies, and visualized with Alexa Fluor 555- and Alexa Fluor 488-conjugated anti-mouse IgG2b and IgG2a secondary antibodies, respectively. Likewise, surface-bound LGI3-HA was live-stained with anti-HA antibodies and visualized with Alexa Fluor 488-conjugated anti-Rb IgG secondary antibody after fixation with 4% PFA. After permeabilization, the total Kv1.2 was stained with anti-Kv1.2 antibody and visualized with Alexa Fluor 555-conjugated anti-mouse IgG2b secondary antibody. Fluorescent images were acquired with a confocal laser scanning microscopy system (LSM5 Exciter, Carl Zeiss) equipped with a Plan Apochromat 63x/1.40 oil immersion objective lens. Microscope control was performed with Carl Zeiss ZEN software.

Cell surface colocalization and co-clustering assay

For cell surface colocalization analysis, COS7 cells were seeded onto three poly-*d*-lysine coated 12-mm coverslips in each well of a 6-well plate (2x10^5 cells/well) and cotransfected with ADAM23 and Kv1.4-HA or DPP10-HA, or with Kv1.4-HA and N-cadherin. Kv1.4 has a highly conserved amino acid sequence with Kv1.1 and Kv1.2 (~65% identity) involving a similar PDZ-binding motifs (PBM) that directly interact with PDZ domains of PSD-95 and is more efficiently expressed at the cell surface than Kv1.2 *in vitro*.[85] At 24 h after transfection, the cells were fixed with 4% paraformaldehyde/120 mM sucrose/100 mM HEPES (pH7.4) at room temperature (RT) for 10 min and blocked with PBS containing 10 mg/mL BSA for 10 min on ice. The surface-expressed proteins were stained with the anti-ADAM23, anti-HA, and anti-N-cadherin antibodies for 60 min at RT. Then the cells were incubated with Alexa Fluor 488 or Cy3-conjugated secondary antibodies for 60 min at RT.

For cell surface co-clustering assay, COS7 cells were cotransfected with the indicated combination of ADAM23, N-cadherin, Kv1.4-HA, and PSD-95-FLAG. At 24 h after transfection, the cells were fixed with 4% paraformaldehyde/120 mM sucrose/100 mM HEPES (pH7.4) at room temperature (RT) for 10 min and blocked with PBS containing 10 mg/mL BSA for 10 min on ice. The surface-expressed ADAM23, Kv1.4-HA, and N-cadherin were stained with the anti-ADAM23, anti-HA, and anti-N-cadherin antibodies, respectively for 60 min at RT. After washing the cells with PBS followed by blocking, cells were incubated with Alexa Fluor 488 or Cy3-conjugated secondary antibodies for 60 min at RT. Then, cells were permeabilized with 0.1% Triton X-100 and incubated with anti-FLAG antibody for 60 min at RT, followed by Alexa Fluor 647-conjugated secondary antibody. Fluorescent images were acquired with a confocal laser scanning microscopy system (TCS SP5 II, Leica) equipped with an HCX PL APO 63x/1.40 oil immersion objective lens. Microscope control and all image analyses were performed with Leica LAS AF software.

Immunohistochemistry/fluorescence analysis

Lgi3$^{FH/FH}$ or *Lgi3*$^{-/-}$ mice and their control wild-type (or C57BL/6) mice were treated with sodium pentobarbital (100 mg/kg, i.p.) and transcardially perfused with 4% paraformaldehyde in 0.1 M phosphate buffer (pH 7.4). The brain was removed and immersed in the same fixative for 12 h at 4°C, cryoprotected in 20% sucrose in PBS overnight at 4°C, embedded in OCT compound, and frozen at −80°C. The 30-μm free-floating sections were cut on a cryostat (CM1950, Leica). Antigen retrieval was performed by incubating the sections in 10 mM citrate buffer (pH 6.0) at 80°C for 30 min followed by rinsing with PBS. The sections were blocked for 1 h in PBS containing 10% normal goat serum and 0.3% Triton X-100 at 4°C and then incubated in the mixture of indicated primary antibodies (see Key resources table) for 36–48 h at 4°C. After washing with PBS containing 0.3% Triton X-100, signals were visualized with Alexa Fluor 488, Cy3, and Alexa Fluor 647-conjugated secondary antibodies.

Alternatively, freshly dissected brains and sciatic nerves of *Lgi3*$^{FH/FH}$ or *Lgi3*$^{-/-}$ mice and their littermate controls were frozen in n-hexane cooled on dry ice, and embedded in OCT compound. Then, the frozen sections (7-μm in thickness) were cut on a cryostat

and fixed with acetone for 20 min on ice (on glass slides). Fixed sections were rehydrated and blocked for 1 h at RT in PBS containing 10% normal goat or donkey serum, and were incubated in the mixture of indicated primary antibodies (see Key resources table) for 1 h at RT, followed by the mixture of Alexa Fluor 488, Cy3, and Alexa Fluor 647-conjugated secondary antibodies. Specific reactivities of anti-LGI1 antibody were previously described.[77] Fluorescent images were acquired with a confocal laser scanning microscopy system (TCS SP5 II, Leica) equipped with an HCX PL APO 63x/1.40 oil immersion objective lens. Microscope control and all image analyses were performed with Leica LAS AF or LAS X software, and images were acquired with the same laser power and detector settings for comparison.

For imaging the protein distribution in the whole brain, fresh frozen brain sections were incubated with the indicated primary antibodies and subsequently with IRDye 680CW or IRDye 800CW conjugated secondary antibody, and scanned at a wavelength of 700 or 800 nm, respectively, by an infrared scanning system (Odyssey CLx, LI-COR). Scanning system control and all image analyses were performed with Image Studio and Image Studio Lite software (LI-COR).

For quantifications of the oligodendrocyte lineage cell density in CC, nine different images were obtained from three slices of each animal using confocal microscopy (TCS SP5 II, Leica). The scanned target area of the tissue was measured using Fiji/ImageJ software (https://imagej.net/Fiji) and the number of CC-1 or Olig2 positive cells was manually counted. Cell densities were calculated as cell number/mm^2. For each group, three different animals were used for the quantification.

For quantifications of the perinodal architecture, the number and size of the paranodal Caspr1 clusters were measured using ''analyze particles'' plugin of Fiji/ImageJ software with the original grayscale images. The same settings of thresholding and range were applied for comparison. The number and the longitudinal length of the juxtaparanodal clusters were manually measured by using Fiji/ImageJ. The juxtaparanodal clusters were defined as the clusters flanked by paranodal Caspr1 clusters.

Three to ten images per slice were obtained from each animal. For each group, three different animals were used for the quantification, except for Figures S7D and S7E (described in Figure legends). Adjustments of the brightness, contrast, and input levels on Adobe Photoshop were equally applied across the whole image and among images to be compared in the Figures. For quantification of protein density of the juxtaparanodal Kv1 channels, circular regions of interest of 0.134 μm^2 (common minimum area) were made in the proximal area of JXP (immediately adjacent to the paranodal clusters) and the mean intensity was measured by using Fiji/ImageJ software. For colocalization analysis of LGI3 or LGI1 with vGlut1 and vGlut2 (vGlut1/2), Manders co-localization coefficient was obtained by ''BIOP-JACoP'' plugin of Fiji/ImageJ software. For quantification of the density of Kv1.2 expressed at the presynapse in the cortex, vGlut1/2-positive puncta were identified by ''analyze particles'' plugin of Fiji/ImageJ software, and the fluorescent intensity of Kv1.2 overlapping vGlut1/2-puncta was measured. For quantification of the juxtaparanodal cluster formation on the *Adam23* or *Adam22* knock-out axons achieved by AAV-mediated CRISPR-Cas9 system (see ''AAV vector preparation and infection'' and ''Stereotaxic injection of AAV vector''), AAV-infected axons were identified by mCherry reporter expression. Then, the number of the paranodal Caspr1 clusters and adjacent juxtaparanodal clusters on the mCherry-positive axons were manually counted by using Fiji/ImageJ. We observed the contralateral cortex to the AAV-injected hemisphere (Figure 6F) since the mCherry-positive axons were sparsely identified and not masked by somatodendritic mCherry signals in contrast to the ipsilateral hemisphere.

STED superresolution imaging and image analysis

Immunohistochemistry: 4% paraformaldehyde-fixed mouse brain blocks embedded in the OCT compound were prepared as described above. Frozen sections (7-μm in thickness) were cut on a cryostat and placed on precoated slides. Antigen retrieval was performed by incubating the sections in 10 mM citrate buffer (pH 6.0) at 95°C for 15 min. After rinsing with PBS, the sections were blocked for 1 h in PBS containing 10% normal goat serum and 0.3% Triton X-100 at 4°C, and then incubated in the mixture of indicated primary antibodies (see Key resources table) at 4°C overnight. After washing with PBS containing 0.3% Triton X-100, sections were incubated in the mixture of fluorescent secondary antibodies for 2 h at RT. Immunocytochemistry: rat primary cultured hippocampal neurons (12 DIV) were fixed with 4% paraformaldehyde for 20 min at RT and permeabilized with 0.1% Triton X-100 for 10 min on ice. After washing with PBS, neurons were blocked with PBS containing 10 mg/mL BSA for 10 min on ice and incubated with anti-Kv1.1 antibody at 4°C overnight. After washing with PBS, neurons were incubated in the fluorescent secondary antibodies at 4°C overnight. Specimens were mounted in ProLong Diamond (Thermo Fisher Scientific). For two color-STED imaging with 660-nm or 775-nm depletion laser, Alexa Fluor 488- and 555-conjugated secondary antibodies (Thermo Fisher Scientific) or Alexa Fluor 594- (Thermo Fisher Scientific) and STAR 635P- (Abberior Instruments) conjugated secondary antibodies were used, respectively. For single-color STED imaging, 775-nm depletion laser and STAR 635P-conjugated secondary antibodies were used. Gated-STED imaging was performed using Leica TCS SP8 gated STED superresolution system combined with Leica HyD detectors (supported by Exploratory Research Center on Life and Living Systems, ExCELLS). Single optical slices were acquired with an HC PL APO 100x/1.40 Oil STED WHITE objective lens (5× or 10x zoom; 1,024 x 1,024-pixel format; 100 Hz scan speed; 2 line-averaging). Alexa Fluor 488, -555, −594, and STAR 635P were excited at 488, 554, 594, and 633-nm white-light laser, respectively. Depletion was accomplished with a CW 660-nm laser (set at 65% of laser power, 10% for z-depletion; and time-gating of HyD detectors at 0.5–3 ns) or a pulsed 775-nm laser (set at 20–30% of laser power, 10% for z-depletion; and time-gating of HyD detectors at 0.3–10 ns). The acquired images were processed with Lightning deconvolution (Leica) to obtain the maximum resolution. The subcluster size of juxtaparanodal proteins was defined as the full width at half maximum (FWHM) across the fluorescence signals by using FWHM tool in LASX software (Leica). To avoid artifacts in measurements, the spatially confined signals which were recognized as subcluster-shape before and after Lightning deconvolution were measured. Subclusters which were sparsely identified and

separated from each other in the distal JXP were selected for the measurements. To show close or overlapping localization between juxtaparanodal proteins, intensity line profiles were drawn across the juxtaparanodal protein clusters by using the LASX software. The specificity of obtained signals for LGI3-FH was validated by using wild-type mice as a negative control. The length of juxtaparanodal Kv1.1 clusters in the mouse cortex was manually measured by using Fiji/ImageJ and compared between wild-type and *Lgi3*$^{-/-}$ mice. To identify the periodic nanostructure of Kv1.1 at the AIS in the rat primary cultured neurons, intensity line profiles were drawn across the juxtaparanodal protein clusters by using Fiji/ImageJ.

Fluorescent *in situ* hybridization (FISH)

Double label FISH was performed with the probes targeting *Lgi3* (cat#446531), *Lgi1* (cat#523191), *Lgi2* (cat#580991), and *Mbp* (cat#451491) mRNAs by using the RNAscope fluorescent multiplex detection kit V1 (Advanced Cell Diagnostics) according to the manufacturer's instructions. Fresh frozen mouse brain sections (10-μm thick) were fixed with 4% paraformaldehyde, followed by tissue pretreatment, probe hybridization following RNAscope fluorescence multiplex assay, and sections were counterstained with DAPI to visualize nuclei. Fluorescent images were acquired with a confocal laser scanning microscopy system (LSM5 Exciter, Carl Zeiss) equipped with a Plan Apochromat 63x/1.40 oil immersion objective lens. Microscope control was performed with Carl Zeiss ZEN software. The specificity of the assay was validated by using positive (cat#321651) and negative control (cat#320751) probes. *Mbp* transcripts were detected not always at the nucleus and cell body, but throughout the white matter because of intracellular trafficking of *Mbp* mRNA in oligodendrocytes.[86] Thus, we manually counted the nucleus containing *Mbp* transcripts (at least more than four puncta) for the *Mbp*-positive cell. Similarly, the nucleus with *Lgi3*, *Lgi1*, or *Lgi2* transcripts was counted. The numbers of the positive cells were quantified and summarized in Table S1. The results from two independent experiments were pooled.

In utero electroporation

Plasmids, pCAGGS-ChR2-Venus[87] and pCAGGS-mCherry, were purified using the Endofree plasmid maxi kit (Qiagen). Plasmid DNA was diluted to 0.6 mg/mL (ChR2) with 0.3 mg/mL (mCherry) in PBS, and Fast Green solution was added to a final concentration of 0.03% to monitor the injection. Pregnant C57BL/6N (wild-type) or *Lgi3*$^{-/-}$ mice with E15.5 embryos were anesthetized with ketamine (40 mg/kg, i.m.) and xylazine (4 mg/kg, i.m.). DNA solution (~0.5 μL) was injected into the lateral ventricle of embryos, using glass pipettes. To control expression sites among cortical areas, electroporation was performed with triple electrode probes.[88,81] The head of each embryo was held with a tweezers-type electrode (as negative poles), and a single electrode (as a positive pole) was attached to the motor cortical area. Square voltage pulses (35 V in amplitude and 50 ms in duration) were applied five times at 1 s intervals. After surgery, embryos were returned to the abdominal cavity, and the abdominal wall and skin were sutured.

Slice experiments

Brain slices were prepared from both male and female animals, expressing ChR2 and mCherry by *in utero* electroporation, aged between postnatal 65–85 days, as described previously.[89] Brains were cut in an ice-cold solution containing (in mM): 90 N-methyl-D-glucamine, 40 choline-Cl, 2 KCl, 1.25 NaH_2PO_4, 1.5 $MgCl_2$, 0.5 $CaCl_2$, 26 $NaHCO_3$, and 10 glu0cose (310 ± 5 mOs/mL, pH 7.4 adjusted with HCl). Slices including motor cortical area (300-μm thickness) were incubated in an oxygenated artificial cerebral spinal fluid (ACSF) composed of (in mM): 126 NaCl, 2.5 KCl, 1.25 NaH_2PO_4, 1 $MgCl_2$, 2 $CaCl_2$, 26 $NaHCO_3$, and 10 glucose (310 ± 5 mOs/mL, pH 7.4; bubbled with 95% O_2/5% CO_2) containing 0.2 mM ascorbic acid and 4 mM lactic acid at RT. The bath solution (ACSF) was continuously perfused in the recording chamber, where the temperature was adjusted to 30°C. Whole-cell recordings were obtained from motor cortical PCs located at upper part of L5 (L5a), using pipettes filled with a solution containing (in mM): 130 potassium methylsulfate, 0.5 EGTA, 2 $MgCl_2$, 2 Na_2ATP, 0.2 GTP, 20 HEPES, 0.1 leupeptin and 0.75% biocytin (pH 7.2, 290 ± 5 mOs/mL). To activate ChR2, blue light illumination (473 nm DPSS laser, 1–1.5 mW in intensity and 1 msec in duration) was applied through a 40× water immersion objective lens. Irradiation area was restricted to 300-μm diameter by insertion of a pinhole on the optical path. Light illumination was applied to the medial part of white matter at approximately 100-μm horizontal distance from the recording cell (White matter stimulation). EPSCs were recorded while membrane potentials were voltage-clamped at −60 mV. Recordings were discarded when synaptic currents consisting of multiple peaks were evoked by a single light stimulation. The amplitude of each EPSC in the train was measured from the level immediately before each EPSC onset. Intensity and duration of light stimulation were controlled with a computer. In axonal loose-patch recordings, action potentials were evoked by electrical stimulation applied through a bipolar tungsten electrode. The electrode was placed in the middle of two cerebral hemispheres of corpus callosum (Figure 7K, inset). A current pulse of 0.5–1.5 mA in amplitude and 50 μsec in duration was used for stimulation.

Basic physiological properties of L5a PCs and L2/3 PCs were analyzed in recordings obtained with a current-clamp mode (Tables S4 and S5). The input resistance was determined with a transient voltage response to a brief hyperpolarizing current injection (−30 pA, 200 msec duration). Spike threshold was defined as a voltage preceding the spike when the first derivative dVm/dt > 20 mV/ms in firing responses evoked by current pulse injection. Spike height was determined with the difference of the threshold and the peak of a spike. Spike width was defined as the time from the threshold to the potential repolarized to the same voltage. All data were obtained and analyzed using Axograph software (AxoGraph). Data were represented as mean ± SD.

Structural protein modeling and sequence alignment

For the prediction of three-dimensional structural models of human LGI3 (NP_644807), the homology modeling was performed by SWISS-MODEL server (https://swissmodel.expasy.org/) using the LGI1 structure in the LGI1–ADAM22 complex [PDB 5Y31 (https://doi.org/10.2210/pdb5Y31/pdb)] as a template. PyMOL software (Schrödinger) was employed for the three-dimensional graphics representation. Sequence alignments were performed by ClustalW2 run by European Molecular Biology Laboratory (https://www.ebi.ac.uk/Tools/msa/clustalw2/).

AAV vector preparation and infection

DJ-type AAV vectors were prepared using AAV-DJ Helper Free Packaging System (Cell Biolabs). Briefly, the packaging plasmids (pAAV-DJ and pHelper) and transfer plasmid (pAAV-U6-sgRNA-CAG-mCherry) were transfected into HEK293T cells using the calcium phosphate method. A crude cell extract containing AAV vector particles was obtained from transfected cells, and AAV vector particles were subsequently purified by serial ultracentrifugation with cesium chloride. The purified particles were dialyzed with phosphate-buffered saline (PBS) containing 0.001% Pluronic F-68 (Sigma-Aldrich), followed by concentration with an Amicon 10K MWCO filter (MerckMillipore). The copy number of the viral genome (vg) was determined by real-time quantitative PCR. The following sgRNA target sequences (5′-3′) were used: Scramble, GCACTACCAGAGCTAACTCA; *Adam23*, GCTTACCCGAGCTCCACGTAT; *Adam22*, GGTGCATAATGGGAGACACC. For validation of CRISPR-Cas9-based gene targeting, the primary cultured cortical neurons from *Rosa26*$^{Cas9/Cas9}$ mouse (3 DIV) were infected with the AAV for 11 days followed by western blotting analysis of the harvested neuron lysates.

Stereotaxic injection of AAV vector

Adult mice (P38-46) were anesthetized with ketamine hydrochloride (100 mg/kg body weight, i.p.) and xylazine hydrochloride (5 mg/kg body weight, i.p.). AAV DJ-sgRNA-CAG-mCherry vectors ($2.1–3.0\times10^{13}$ vg/ml) were injected into the two different sites of the primary motor cortex (M1) by a glass capillary connected to a micro infusion pump (0.6 μL in each site of the M1 at 0.1 μL/min). The injection sites of the anteroposterior (AP) and mediolateral (ML) coordinates from the bregma and the dorsoventral (DV) coordinate from the dura were as follows: AP 1.5 mm, ML 2.0 mm, DV 1.0 mm and AP 1.0 mm, ML 1.7 mm, DV 0.8 mm. Eight weeks after injection (P94-102), mice were subjected to immunohistochemical analysis as described in "Immunohistochemistry/fluorescence analysis".

Animals used for behavioral experiments

Behavior analysis was performed using male mice. At the start of the rota-rod test, mice were between eleven to fifteen weeks of age. Morris water maze test followed the rota-rod test. Mice were accustomed to the experimenter by careful handling for more than one week before the start of experiments. At the introduction of the IntelliCage system for the series of behavioral tasks, mice were aged between ten to fourteen weeks. No handling was performed on the mice prior to their introduction to the IntelliCage system.

Rota-rod

Motor coordination and learning were assessed with an accelerating rod apparatus (Ugo-Basile, #47650), which consisted of a plastic rod (3 cm diameter, 5.8 cm long) with a gritted surface flanked by two large discs. On the first trial day, before the trials mice were placed on the rod rotated at 5 rpm for several seconds for habituation. In the trials, mice were placed on an accelerating rotarod with the rotation speed starting at 5 rpm and gradually increasing up to 40 rpm over 300 s. Latency until a fall was monitored for 300 s (cut-off time). Mice were given three trials each day with 20-min rests between trials. The experiments were performed for 3 consecutive days.

Morris water maze

The Morris water maze was performed as previously described.[90] A circular pool with a diameter of 1 m was filled with opaque water colored with white paint to a depth of 20 cm. Water temperature was maintained at 24°C–25°C. The escape platform with a diameter of 11 cm was submerged 1 cm below the water surface. The visible cue for the platform consisted of a black pole (10 cm tall) with a ball on top colored black in its lower half (3.5 cm in diameter) standing in the center of the platform. The swimming paths of animals were recorded by a black and white charge-coupled device video camera mounted above the center of the pool using LabVIEW and Vision software (National Instruments; RRID: SCR_014325), and analyzed by Igor Pro 9 software (WaveMetrics; RRID: SCR_000325). Extra-maze cues were posted above the wall of the pool as spatial references.

Naive mice were first accustomed to the water without spatial cues and the visible cue for the platform on the day before the start of water maze training. They were gently released into the pool, allowed to swim for 30 s, then guided onto the submerged platform, and allowed to remain there for 30 s. This procedure was repeated three to four times.

In water maze training, mice were individually subjected to two blocks (30–60 min apart) of four trials (30-s intertrial interval) per day with spatial cues. Platform location was fixed for the same group of mice trained on the same days, but altered among different groups of mice (Six to seven mice per group). Mice were gently released into the pool with the starting position changed in each trial, and given 60 s to reach the platform. After climbing onto the platform, mice were allowed to remain there for 30 s. If a mouse was unable to locate the platform within 60 s, the trial was concluded, and the mouse was gently guided onto the platform and remained

there for 30 s. After the training, mice were returned to their home cage. The escape latency was calculated as the average time of the four trials per block to reach the platform. Mice were subjected to visible platform training for the first 3 days. Subsequently, the visible cue for the platform was removed with the platform location kept intact. The mice were then given hidden platform training for another 6 days. On days 3 and 6 of hidden platform training, the platform was removed after training trials of the day, and a probe trial was performed to assess spatial memory. Mice were released into the pool from the opposite side of the original platform location and allowed to search for the platform location for 60 s, while their swimming paths were recorded. Mice were then gently guided to the original platform location and allowed to sit on the large spatula for 30 s. The following parameters were measured for each probe trial: (1) the percentage of time spent in each imaginary quadrant of the pool (target, left, opposite, and right quadrants); (2) the number of center crossings of the hypothetical platform location in each quadrant; and (3) swimming speed. The escape latencies for visible and hidden platform training were compared between the genotypes by using two-way repeated measures ANOVA, followed by Bonferroni's post hoc test where appropriate. The percentage of time spent in each imaginary quadrant of the pool and the number of center crossings of the hypothetical platform location in each quadrant in probe trials were analyzed in each genotype by using one-way ANOVA, followed by Tukey's post hoc test where appropriate. The swimming speed in probe trials was compared between the genotypes by using unpaired t test.

Behavioral analysis using IntelliCage system

The mice were implanted with Radiofrequency identification (RFID) microchips and habituated inside the 61.0 × 43.5 × 21.5 cm^3 cage for over 2 weeks until introduced to the IntelliCage (TSE systems). In the IntelliCage, a total of 16 mice (n = 8 per group) were tested in a single cage. The animal facility was maintained at 20°C–26°C temperature, 40–70% relative humidity, 12 h light-dark cycle (7:00 ON; 19:00 OFF). All mice were fed commercial normal chow *ad libitum* and received water *ad libitum* or as a reward unless otherwise stated.

Test apparatus (IntelliCage)

IntelliCage (TSE Systems GmbH, Germany) is a fully automated testing apparatus (61.0 × 43.5 × 21.5 cm^3) for monitoring behavior of group-housed RFID-tagged mice in a home cage equipped with four triangular operant chambers (hereafter referred as corners) (15 × 15 × 21 cm^3).[58] The corner entrance and the inner space is large enough for a single mouse to enter at a time. Each mouse is recognized by the RFID antennas at its entrance, and the infrared sensors and lickometers inside the corner enable simultaneous monitoring of each RFID-tagged mouse. Each corner holds two water bottles, and their nozzles are accessed through nose poke holes with motorized access doors; the infrared beam-break response detector on each of the nose poke holes responds to the mouse nose pokes which triggers the door opening/closing. Experimenters can flexibly program the rules for opening/closing of the doors.

Experimental setup

The experimental day is defined as a period starting from the beginning of the light phase to the end of the following dark phase. Behavioral responses of each mouse were recorded through various sensor devices of IntelliCage, associated with the animal ID, and were used to analyze each of the spontaneous/cognitive-behavioral indices. The cage was cleaned once a week, and the general health conditions of each mouse were checked (body weights were measured; skin, hair, eyes, mouth, tail conditions, and basic walking movements in an open cage were visually assessed).

Exploratory behavior and basal activity

Mice were introduced to IntelliCage at 9 a.m. and allowed to habituate to the cage environment. When a mouse entered the corner, the door in the nose poke hole opened automatically to permit drinking. Corner visits during the first 24 h were recorded and analyzed as indices of novel environment exploration. After the recording of 24-h exploratory behavior, the door opening was triggered by a nose poke, for the rest of the experiments (unless otherwise stated): A single nose poke would open the door for 3000 msec (on the first day of habituation) or 2000 msec (on the following day) to allow drinking. Corner visits, nose pokes, and lickings for eleven days are recorded and analyzed as indices of basal activity, corner preferences, nose poke hole-preferences, and movement patterns. A wild-type mouse that was not habituated to IntelliCage (only twelve corner visits with drinking water out of twenty-one total corner visits per two days during the habituation session) was excluded from the following experiments.

Self-paced learning and behavioral flexibility (SP-FLEX) test

In this test, each mouse was assigned a pair of corners as correct corners and had to shuttle between the two correct corners to obtain water as a reward, while drinking was not permitted at the remaining pair of corners until the rule switched. When a mouse nose poked at one of the correct corners, the door opened for 2000 msec to permit the liquid intake, except there were the following restrictions: The door opened only once per visit, and a mouse was not permitted to obtain the reward in a row by re-entering in the same corner. Success (getting a reward by a direct move from the previously rewarded corner to another rewarded corner) and failure (visiting and nose-poking at one of the two nonrewarding corners) responses were integrated into Wald's sequential probability ratio test (SPRT) statistics to calculate each mouse's probability of success. Visits without nose pokes were omitted from the calculation. Whenever the performance of a mouse reached the set upper criteria, the assignment of rewarded and non-rewarded corners of the

mouse was reversed. The number of trials (the sum of the above mentioned correct and failure responses) required to reach upper criteria for the rule reversal was used to assess the efficiency of learning and behavioral flexibility; the upper criteria were set at 30%. For the first session, each mouse was assigned one of the two pairs of diagonally positioned corners as correct corners. In the shuffle session, the pair of correct corners was assigned from all possible corner pair combinations, which was shuffled around every reversal. In all conditions, the chance level of this task was 20%, which was set as lower criteria to assess perseveration. The significance level for the acceptance of each criterion was 0.05. There was no set task period, so each mouse performed the task self-paced, therefore the timing of the rule reversal varied for each mouse. Briefly, we used the following two experimental conditions to precisely assess the degree of learning and behavioral flexibility impairments in mice.

Experiment 1; Complete shift (CS) of rewarded corners:

Here, mice initially learned a behavioral sequence in which they were rewarded for moving back and forth between two diagonally opposite corners (e.g., Corners A and C) out of four corners (e.g., Corner A, B, C, D). Whether the performance reached a pre-set criterion (successful visit rate = 30%) was automatically determined by the software using sequential probability ratio statistics that were updated for each corner visit (significance level for the acceptance of successful visit rate being greater than the criterion, was set as 5%). When the performance reached the criterion, the two corners that had been rewarded (Corners A and C) and the two corners that had not been rewarded (Corners B and D) were reversed. Therefore, the mouse has to adapt to the new rule of going back and forth to the previously nonrewarded corners (Figure S8H). Note that all the rewarded corners and all the non-rewarded corners are alternated (therefore referred to as complete shift (CS) protocol). In this experiment, mice underwent only CS protocol. This experiment lasted until all individual mice housed together finished the seventh CS (CS7) up to eight days.

Experiment 2; Shuffled condition with complete shifts (CS) and partial shifts (PS) of the rewarded corners:

Here, the mice first learned a behavioral sequence in which they are rewarded for moving back and forth between two diagonally opposite corners (e.g., Corners A and C) similar to that in experiment 1. When their performance reached the criteria (successful visit rate = 30%), the rewarded corners were changed such that, only one of the two previously rewarded corners was switched with a previously non-rewarded corner. In other words, the combination of the rewarded corners and the non-rewarded corners were partially alternating [therefore referred to as partial shift (PS) protocol]. When the mouse reaches the successful visit rate criterion after the partial shift, all the rewarded and non-rewarded corners are alternated completely (new rewarded-corner combination) as in the CS protocol. In this experiment, CS and PS were presented in shuffled order until their performance reached the criteria, as shown in Figure S8H. This experiment lasted until all individual mice housed together finished the fifth PS (PS5) up to ten days except for the following mouse: A wild-type mouse that did not reach the criteria for more than four days in the middle of the task was excluded from the result.

In experiments 1 and 2, the number of trials required to reach a criterion of performance in the shift phases is used as a measure of behavioral flexibility. In experiment 2, the performance in the entire shift phase including CS and PS is analyzed.

QUANTIFICATION AND STATISTICAL ANALYSIS

Statistical details of individual experiments are described in figure legends or corresponding method sections. To perform statistical analysis, at least 3 experiments were performed for independent tissue samples or mice, except for Figures S7D and S7E, as described in figure legends. We excluded mice if we observed any abnormality in terms of size and weight in mice before performing experiments. The mice in this study were not randomized and were selected based purely on availability. No statistical method was used to determine sample size, and sample sizes are consistent with those reported in similar studies. The variance between groups was compared by F test. For comparisons of unpaired two groups, Two-tailed Student's t test, Mann-Whitney U test, or Welch's t test was used. To compare paired two groups, Wilcoxon signed-rank test was used. For comparisons of multiple test subjects, one-way repeated measures ANOVA with post hoc Tukey's test was used. For comparisons of unpaired two groups in the behavioral analysis, two-way repeated measures ANOVA with post hoc Bonferroni's test was used. To compare within the group, one-way ANOVA, followed by Tukey's post hoc test was used. Statistical analysis was performed with Ekuseru-Toukei 2012 software (BellCurve).

Cell Reports, Volume *43*

Supplemental information

Oligodendrocyte-derived LGI3 and its receptor ADAM23 organize juxtaparanodal Kv1 channel clustering for short-term synaptic plasticity

Yuri Miyazaki, Takeshi Otsuka, Yoko Yamagata, Toshihiro Endo, Makoto Sanbo, Hiromi Sano, Kenta Kobayashi, Hiroki Inahashi, Hans-Christian Kornau, Dietmar Schmitz, Harald Prüss, Dies Meijer, Masumi Hirabayashi, Yuko Fukata, and Masaki Fukata

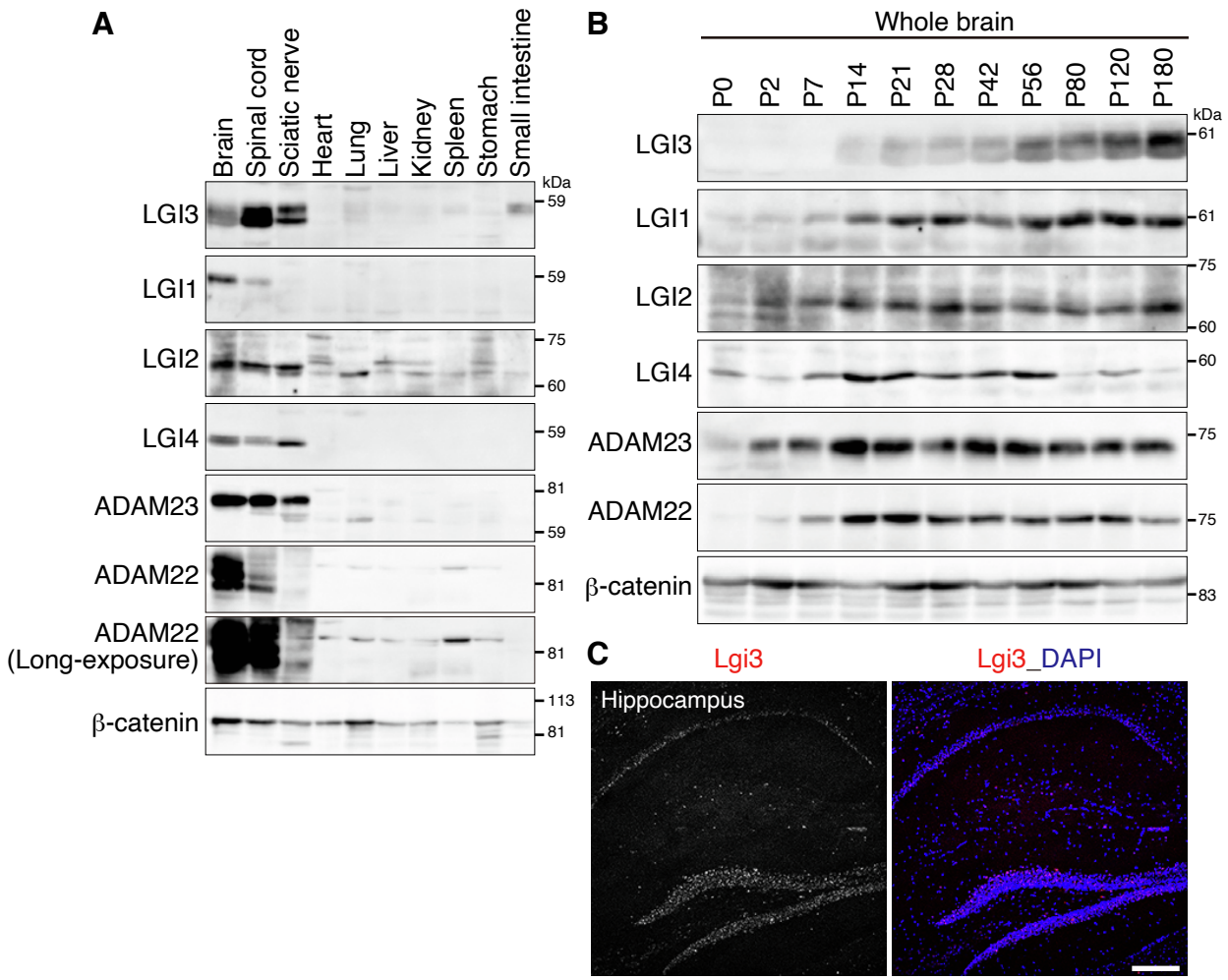

Figure S1. Tissue and developmental expression profiles of LGI family members in mice, Related to Figure 1

(A) Western blotting of various mouse tissue extracts (20 μg total protein each, P90 mouse) for LGI family and ADAM23 family proteins.

(B) Western blotting of mouse brain extracts from different postnatal ages (40 μg total protein each) for LGI family and ADAM23 family proteins.

(C) *Lgi3* mRNA is detected in neuronal cells of the mouse hippocampus (dentate granule cells and CA1 pyramidal neurons) by FISH analysis. Nuclear DNA was stained by DAPI. P125 mouse brain slice was used. Scale bar, 200 μm.

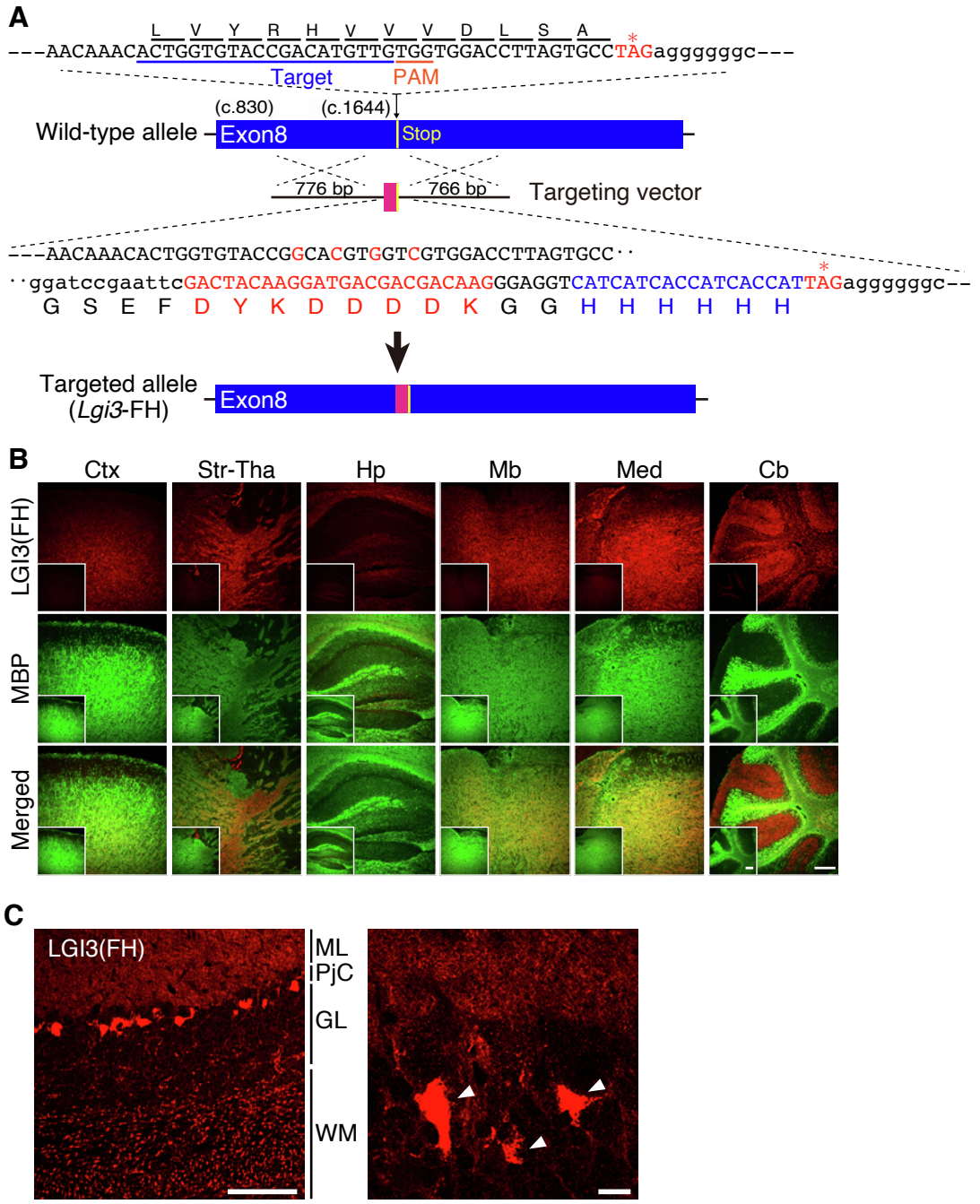

Figure S2. LGI3 is localized in myelin-rich brain regions, cerebellar molecular layers, and basket cell terminals, Related to Figure 2

(A) Targeting strategy for the *Lgi3*$^{FH/FH}$ knock-in allele by the CRISPR-Cas9 system. The targeting vector for the homology-directed repair has a FLAG-Hisx6 (FH) tag sequence (GSEFDYKDDDDKGGHHHHHH) flanked by ~1.5 kb homology arms.

(B) LGI3-FH is largely colocalized with MBP in the various mouse brain regions. Fluorescence signals of FH antibody in *Lgi3*$^{FH/FH}$ mice are specific, as no signals are observed in wild-type mice (insets). Ctx cortex; Str, striatum; Tha, thalamus; Hp, hippocampus; Mb, midbrain; Med, medulla; Cb, cerebellum. Scale bar, 250 μm.

(C) LGI3-FH is localized at the molecular layer (ML) and basket cell terminals (pinceau) in the mouse cerebellum. Note that paintbrush-like clusters of LGI3-FH are observed in the cerebellar white matter (WM) but not in the molecular layer (left). Magnified image shows the localization of LGI3-FH at pinceau (right, arrowheads). PjC, Purkinje cell layer; GL, granule cell layer. Scale bars, 100 μm (left) and 10 μm (magnified, right).

P166 (B) and P100 (C) mouse brain slices were used.

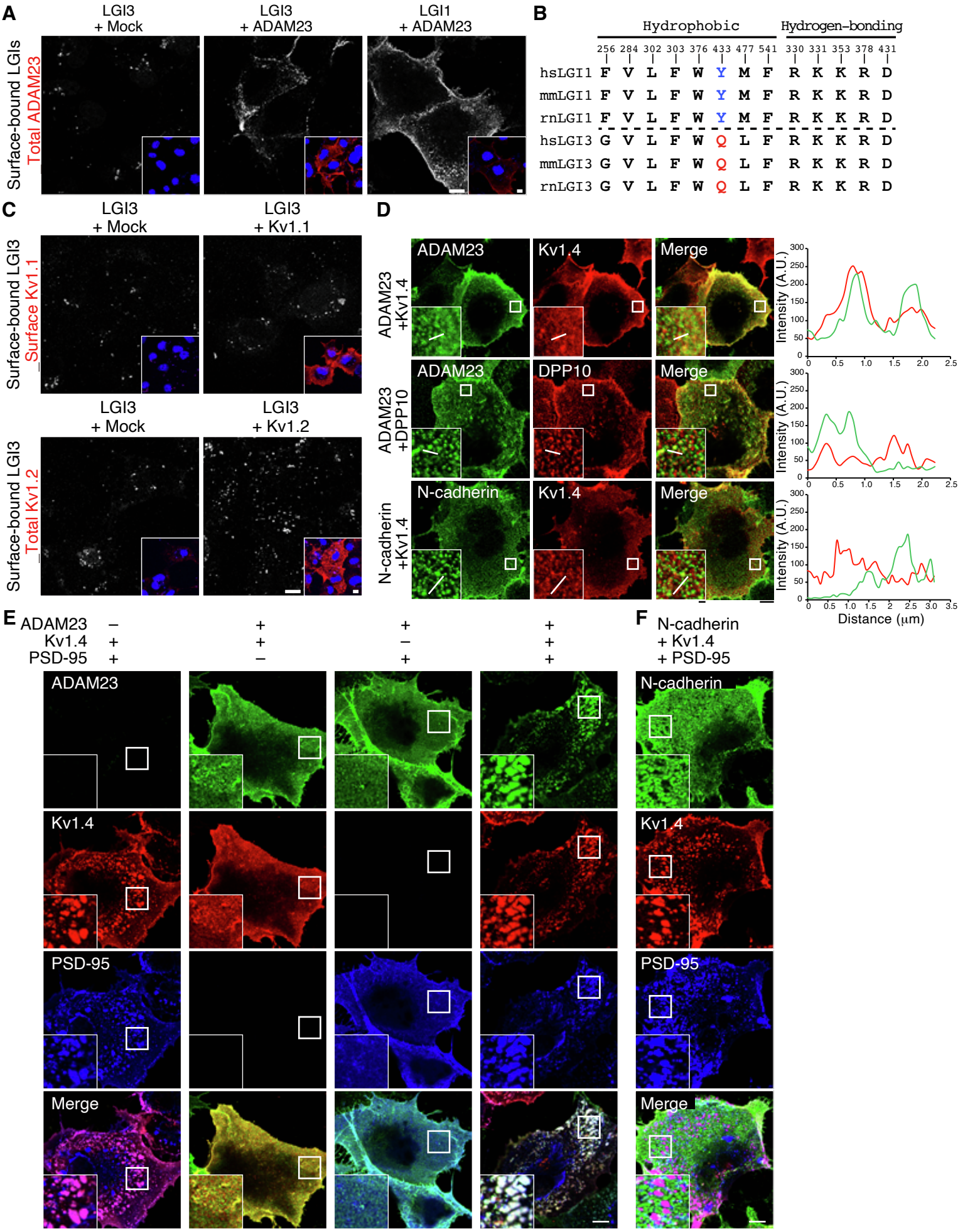

Figure S3 (related to Fig.3)

Figure S3. LGI3 directly interacts with ADAM23 but not with Kv1 channels in vitro, Related to Figure 3

(A) Cell-surface binding assay between LGI3 and ADAM23. COS7 cells were cotransfected with V5-tagged LGI3 or LGI1 (LGIs) and ADAM23 constructs. Surface-bound LGIs were live-stained with anti-V5 antibodies (grayscale). The total ADAM23 was stained after permeabilization (red, inset). The mock-cotransfected cells were used as a negative control for the surface binding of LGI3. Nuclear DNA was stained by Hoechst 33342 (blue). Scale bars, 10 μm.

(B) Amino-acid residues of LGI1 responsible for the hydrophobic and hydrogen-bonding interactions with ADAM22 or ADAM23 are conserved in those of LGI3. Blue and red letters represent amino acid residues with distinct properties at the binding interface of LGI1 and LGI3, respectively. hs, Homo sapiens; mm, Mus musculus; rn, Rattus norvegicus.

(C) Cell-surface binding assay between LGI3 and Kv1 channels. COS7 cells were cotransfected with HA-tagged LGI3 and Kv1.1 (upper), or V5-tagged LGI3 and Kv1.2 (lower) constructs. Surface LGI3 (grayscale) and Kv1.1 were live-stained (red, inset) and total Kv1.2 was stained after permeabilization (red, inset). Nuclear DNA was stained by Hoechst 33342 (blue). Scale bars, 10 μm.

(**D**) Cell surface co-localization analysis indicates the specific co-localization of ADAM23 with Kv1.4. COS7 cells were cotransfected with ADAM23 and Kv1.4-HA (upper), ADAM23 and DPP10-HA (middle), or N-cadherin and Kv1.4-HA (bottom) constructs, respectively. Surface ADAM23, Kv1.4 (HA), DPP10 (HA), and N-cadherin were co-immunostained. The insets show the magnified images of each white square area. Fluorescent intensity profiles along the white lines in the insets are shown (right). Scale bars, 10 μm and 1 μm (insets, magnified).

(**E** and **F**) Cell surface co-clustering assay. (E) Co-expressed Kv1.4-HA (surface) and PSD-95-FLAG showed robust co-cluster formation in contrast to ADAM23 (surface) with Kv1.4-HA or PSD-95-FLAG in COS7 cells. Cotransfection of ADAM23, Kv1.4-HA, and PSD-95-FLAG resulted in large co-cluster formation as observed by cotransfection of Kv1.4-HA and PSD-95-FLAG. (F) The co-clustering activity was not seen for surface N-cadherin in the cells cotransfected with Kv1.4-HA and PSD-95-FLAG. The insets show a magnified image of each white square area. Scale bars, 10 μm.

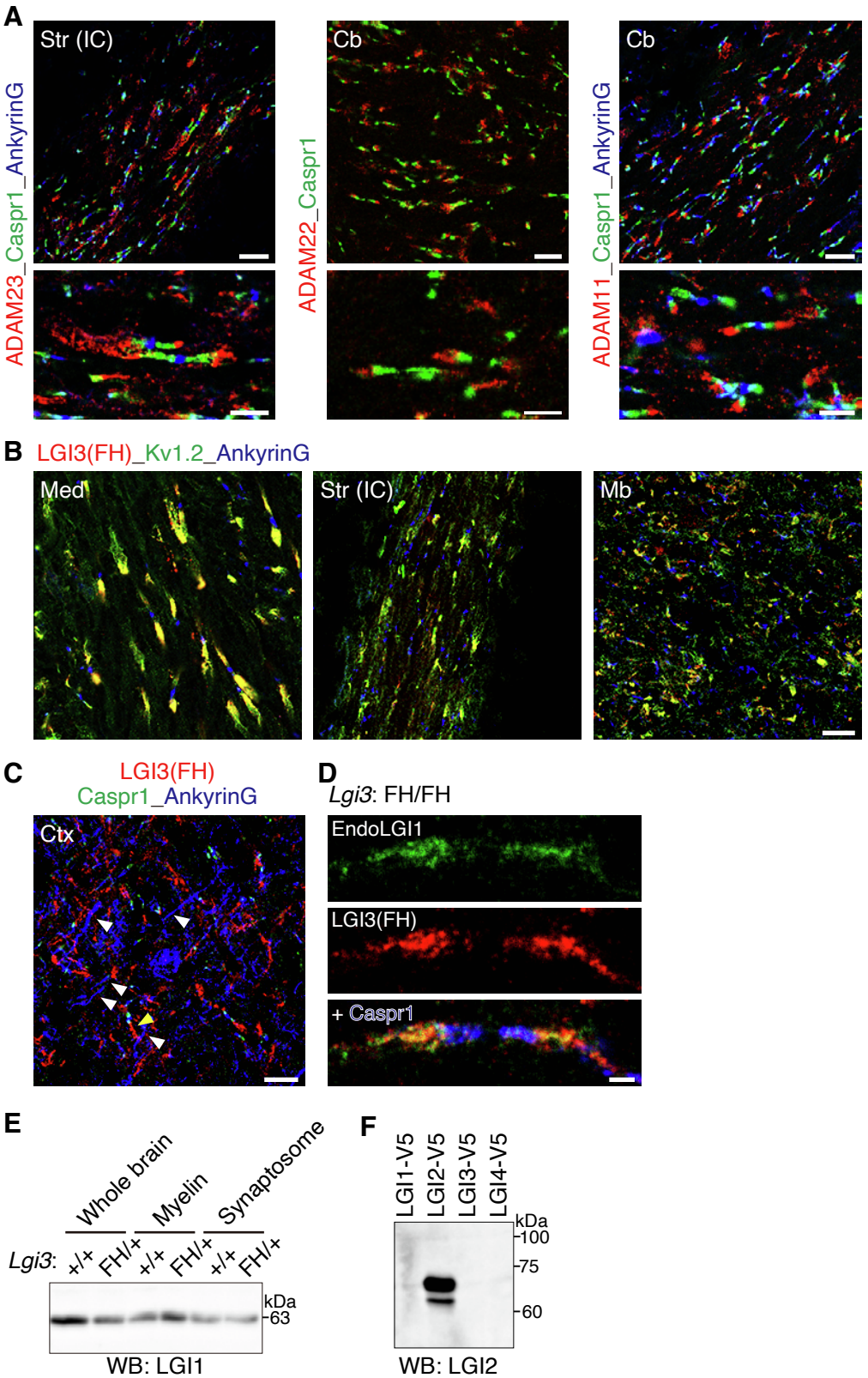

Figure S4 (related to Fig.3)

Figure S4. Juxtaparanodal localization of LGI3-associated proteins: ADAM23 subfamily, Kv1 channels, and LGI1, Related to Figure 3

(A) Localization of ADAM23, ADAM22, and ADAM11 at the JXP in the mouse brain. Caspr1 and ankyrinG were co-labeled for a paranodal marker and a nodal marker, respectively. Scale bars, 10 μm (top) and 5 μm (magnified, bottom).

(B) LGI3-FH and Kv1.2 are colocalized at the JXP in the various brain regions of the *Lgi3*$^{FH/FH}$ mouse. Scale bar, 10 μm.

(C) LGI3-FH is not identified at the AIS in the cortex of the *Lgi3*$^{FH/FH}$ mouse. White arrowheads indicate the AIS determined by the localization of ankyrinG. A yellow arrowhead indicates the representative localization of LGI3 at the JXP. Str, striatum; IC, internal capsule; Cb cerebellum; Med, medulla; Mb, midbrain; Ctx, cortex. Scale bar, 10 μm.

(D) Endogenous LGI1 is colocalized with LGI3-FH at the JXP in the cerebellar white matter of the *Lgi3*$^{FH/FH}$ mouse. Scale bar, 1 μm. P100 (A-D) mouse brain slices were used.

(E) LGI1 protein is detected not only in synaptosomal fractions but also in myelin fractions of the mouse brains (P34). The same sample was analyzed in Figure 2D.

(F) The family member-specific reactivity of the LGI2 antibody was confirmed by Western blotting of conditioned medium from HEK293T cells transfected with LGIs-V5.

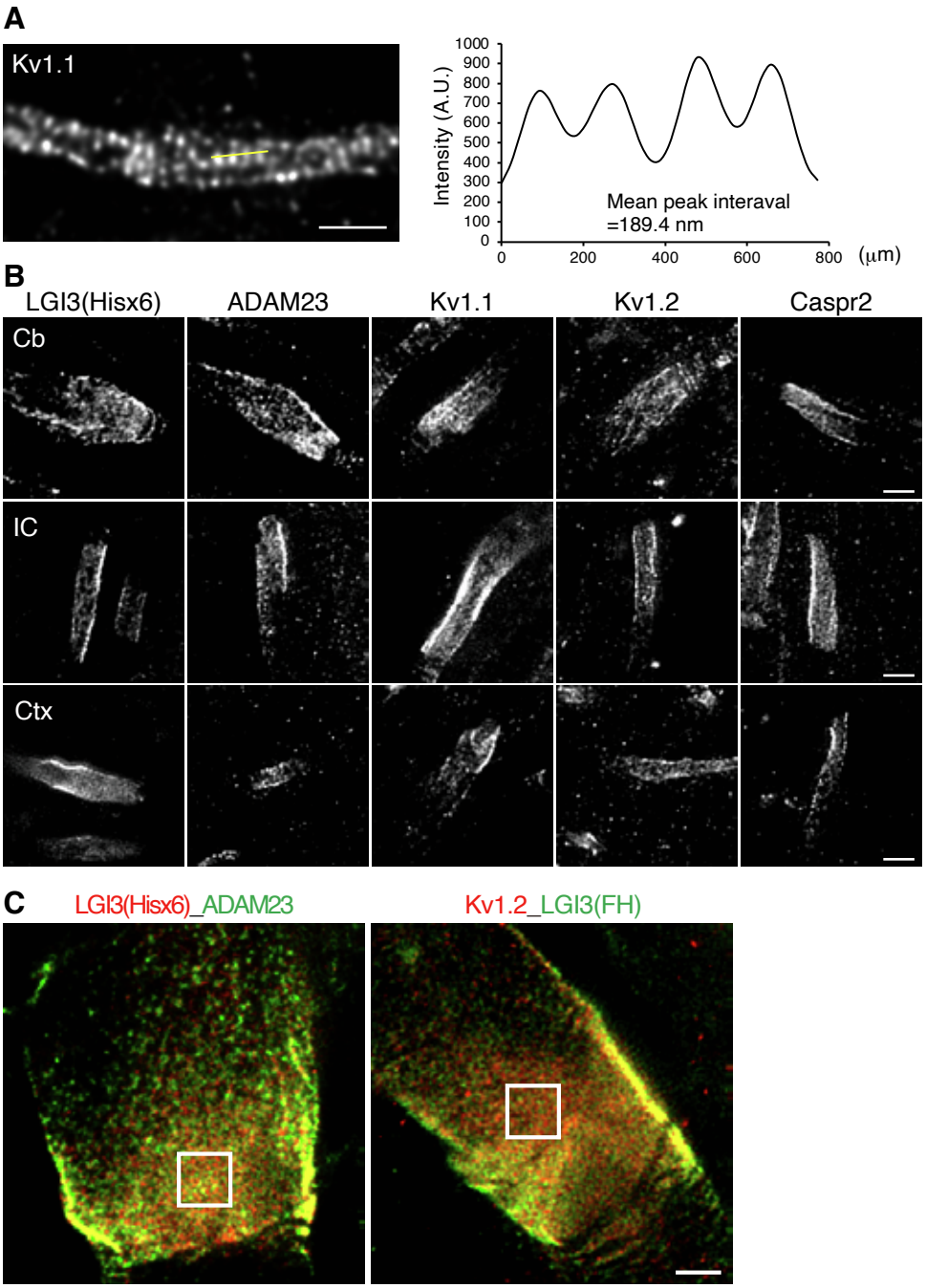

Figure S5. Superresolution imaging of JXP proteins, Related to Figure 4

(**A**) Ladder-like periodic nanoscale localization of Kv1.1 channel at the AIS in rat hippocampal primary cultured neurons. Fluorescent intensity profile along the yellow line and its mean peak interval are shown (right). Scale bars, 1 μm.

(**B**) STED imaging identifies the nanoscale organizations of LGI3, ADAM23, Kv1.1, Kv1.2, and Caspr2 at the JXP in the various brain regions, which resemble those in medulla (Figure 4B). Cb cerebellum; IC, internal capsule; Ctx, cortex. Scale bars, 1 μm.

(**C**) Uncropped images of 2C-STED imaging of JXP proteins. The square areas are magnified in Figure 4C. JXP areas of large axons in medulla were observed. Scale bar, 1 μm.

P100 (A-B) *Lgi3*$^{FH/FH}$ mouse brain slices were used.

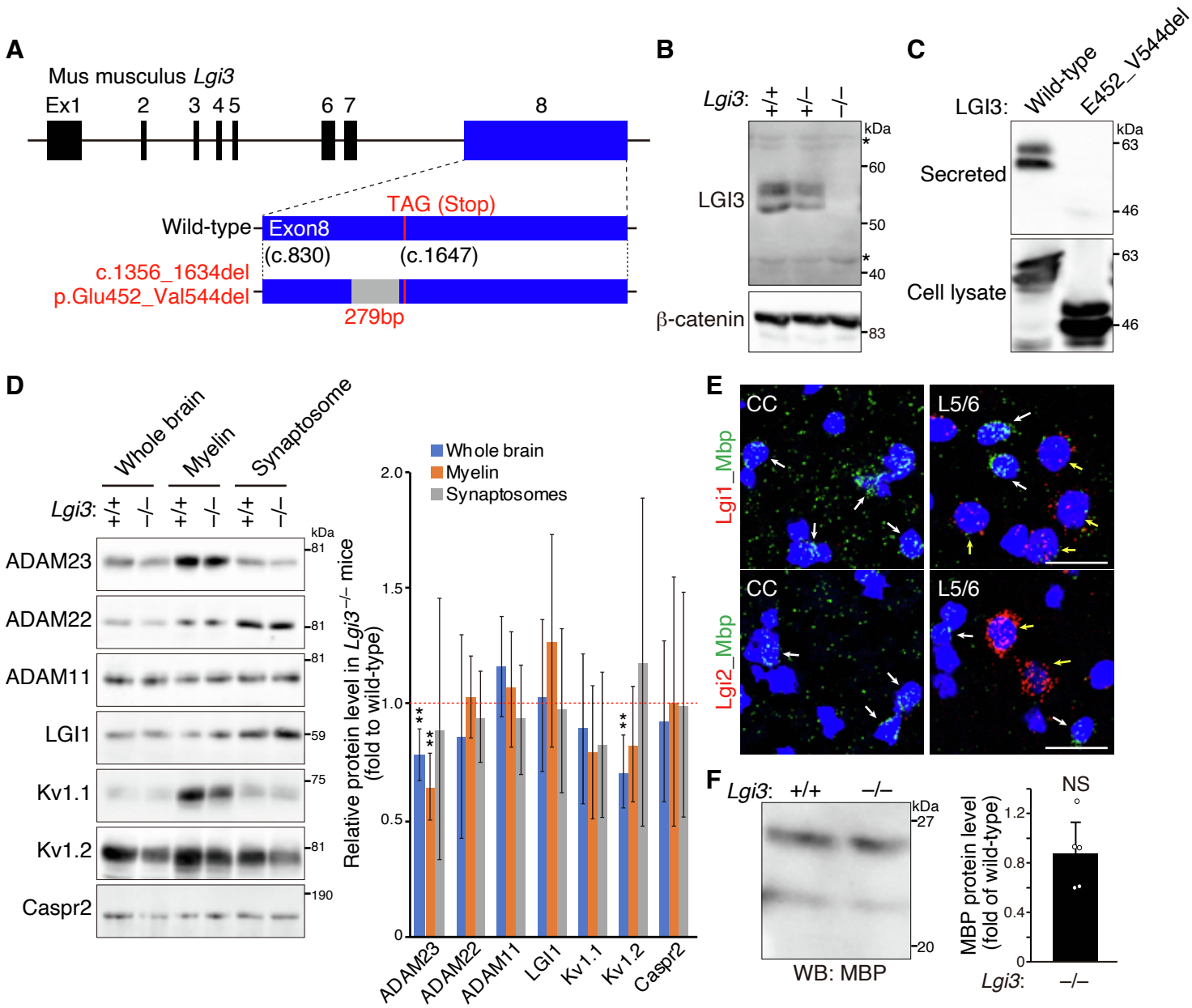

Figure S6 (related to Fig.5)

Figure S6. Generation and characterization of *Lgi3* loss-of-function mutant mouse (*Lgi3*$^{-/-}$ mice), Related to Figure 5

(A) Schematic presentation of the *Lgi3* deletion mutant allele. A large (279 base pair) in-frame deletion mutation in Exon8 of the *Lgi3* gene causes 93 amino-acid deletion in the EPTP domain of LGI3 protein (Glu452_Val544del).

(B) LGI3 protein is not detectable in the whole brain lysate of the homozygous *Lgi3* mutant mouse. An asterisk indicates the nonspecifically detected bands on the Western blot. *Lgi3*$^{+/+}$, *Lgi3*$^{+/-}$, and *Lgi3*$^{-/-}$ indicate wild-type, heterozygous, and homozygous mutant mice, respectively.

(C) LGI3 E452_V544 deletion mutant protein is not secreted from HEK293T cells transfected with rat LGI3 constructs.

(D) Loss of LGI3 reduces ADAM23 and Kv1.2 channels in myelin fractions of the young mouse brain (P30). Representative Western blots of the whole mouse brain lysates and subcellular fractions of wild-type ($^{+/+}$) and *Lgi3*$^{-/-}$ mice with the indicated antibodies are shown (left). Relative protein levels of each fraction of the *Lgi3*$^{-/-}$ mouse brains compared with wild-type control are shown in graph (right). n = 5 mice per genotype. Two-tailed Mann-Whitney U Test. **p < 0.01. mean ± SD.

(E) Loss of LGI3 does not induce *Lgi1* and *Lgi2* mRNA expression in the oligodendrocytes. White arrows, *Mbp*$^{+}$/*Lgi1*$^{-}$ or *Mbp*$^{+}$/*Lgi2*$^{-}$ cells; yellow arrows, *Mbp*$^{-}$/*Lgi1*$^{+}$ or *Mbp*$^{-}$/*Lgi2*$^{+}$ cells. Nuclear DNA was stained by DAPI (blue). P100 *Lgi3*$^{-/-}$ mouse brain slices were used. Scale bars, 20 μm. CC, corpus callosum; L5/6, cortical layers V and VI.

(F) MBP protein levels are not significantly different between wild-type ($^{+/+}$) and *Lgi3*$^{-/-}$ mice (P100). A representative Western blot of MBP protein is shown. Quantification of relative MBP protein levels of the *Lgi3*$^{-/-}$ mouse brain compared to wild-type control is shown in graph. n = 5 mice per genotype. Mann-Whitney U test. NS, not significant. mean ± SD.

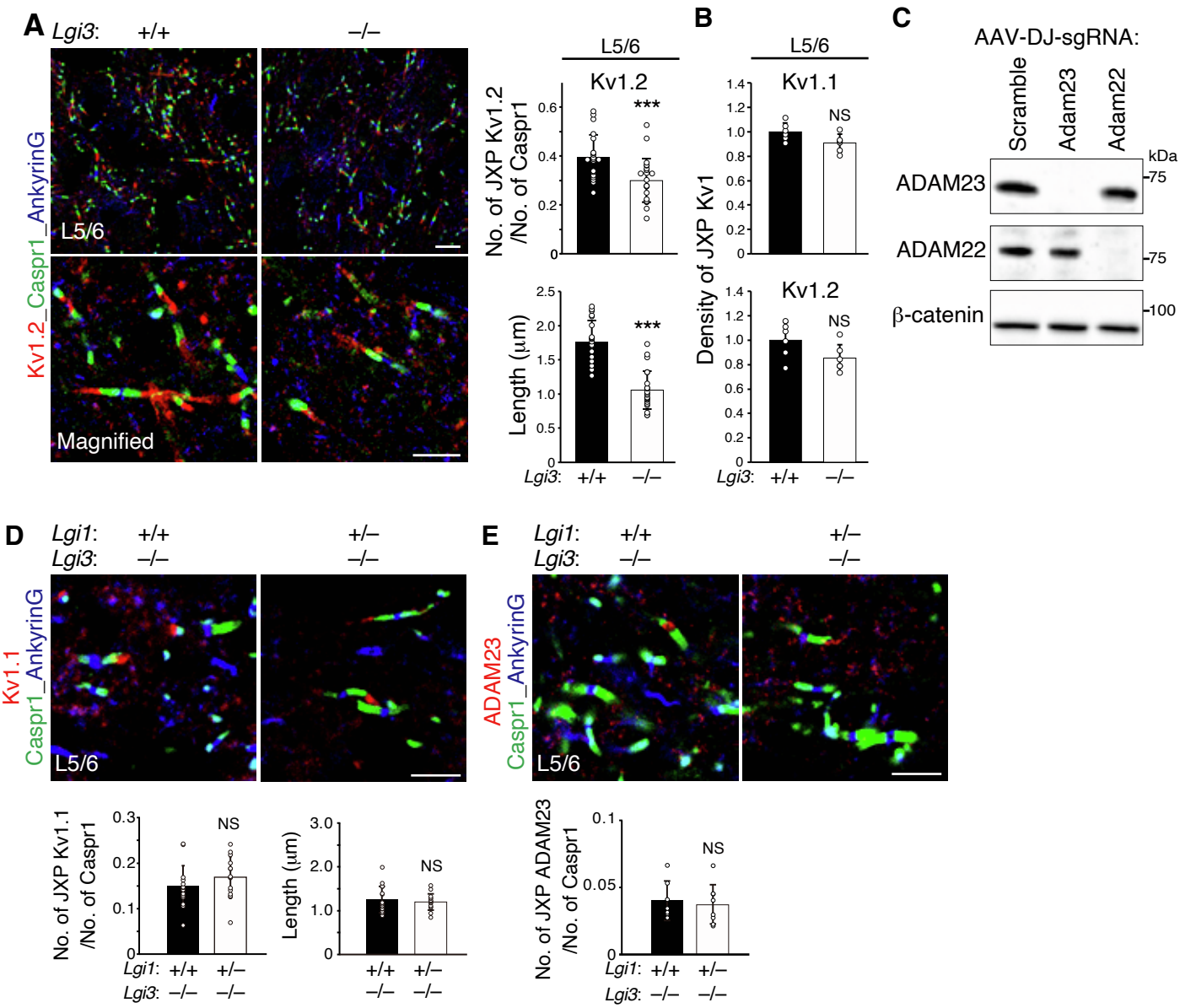

Figure S7. Loss of LGI3 affects Kv1 channel clustering at the JXP, Related to Figure 6

(**A**) Kv1.2 channel clustering at the JXP is impaired by loss of LGI3. Shown are representative images of immunohistochemistry for Kv1.2 channel at the JXP with axonal domain proteins in L5/6 of wild-type ($^{+/+}$) and *Lgi3*$^{-/-}$ mice (left). The number and length of Kv1.2 channel clusters at the JXP are quantitatively compared between genotypes (shown in the graph, right). Scale bars, 10 μm (top) and 5 μm (magnified, bottom). Two-tailed Mann-Whitney U Test. ***p < 0.001. mean ± SD.

(**B**) The density (mean fluorescence intensity) of JXP Kv1 channels in the cortex is not significantly altered in *Lgi3*$^{-/-}$ mice. Two-tailed Mann-Whitney U Test. NS, not significant. mean ± SD.

(**C**) Validation of *Adam23* family gene KO by AAV-mediated CRISPR-Cas9. Primary cultured cortical neurons from *Rosa26*$^{Cas9/Cas9}$ knock-in mouse embryos were infected with AAV-DJ carrying sgRNA expressing cassette and a bicistronic mCherry reporter gene at 3 DIV. The targeted *Adam* family genes were specifically reduced in the cultured neuron lysates harvested at 14 DIV. AAV was treated at 1.0 x 10^4 vg /cell.

(**D** and **E**) The clustering of Kv1 channels and ADAM23 at the JXP was not significantly different between *Lgi1*$^{+/+}$;*Lgi3*$^{-/-}$ and *Lgi1*$^{+/-}$;*Lgi3*$^{-/-}$ mice. Shown are representative images of immunohistochemistry for Kv1.1 channel (D) and ADAM23 (E) clusters at the JXP in the cortex (L5/6). The number and length of juxtaparanodal Kv1.1 channel and ADAM23 clusters are quantitatively compared between genotypes (shown in the graph, right). n = 2 mice per genotype. Mann-Whitney U Test. NS, not significant. mean ± SD. Scale bars, 5 μm.

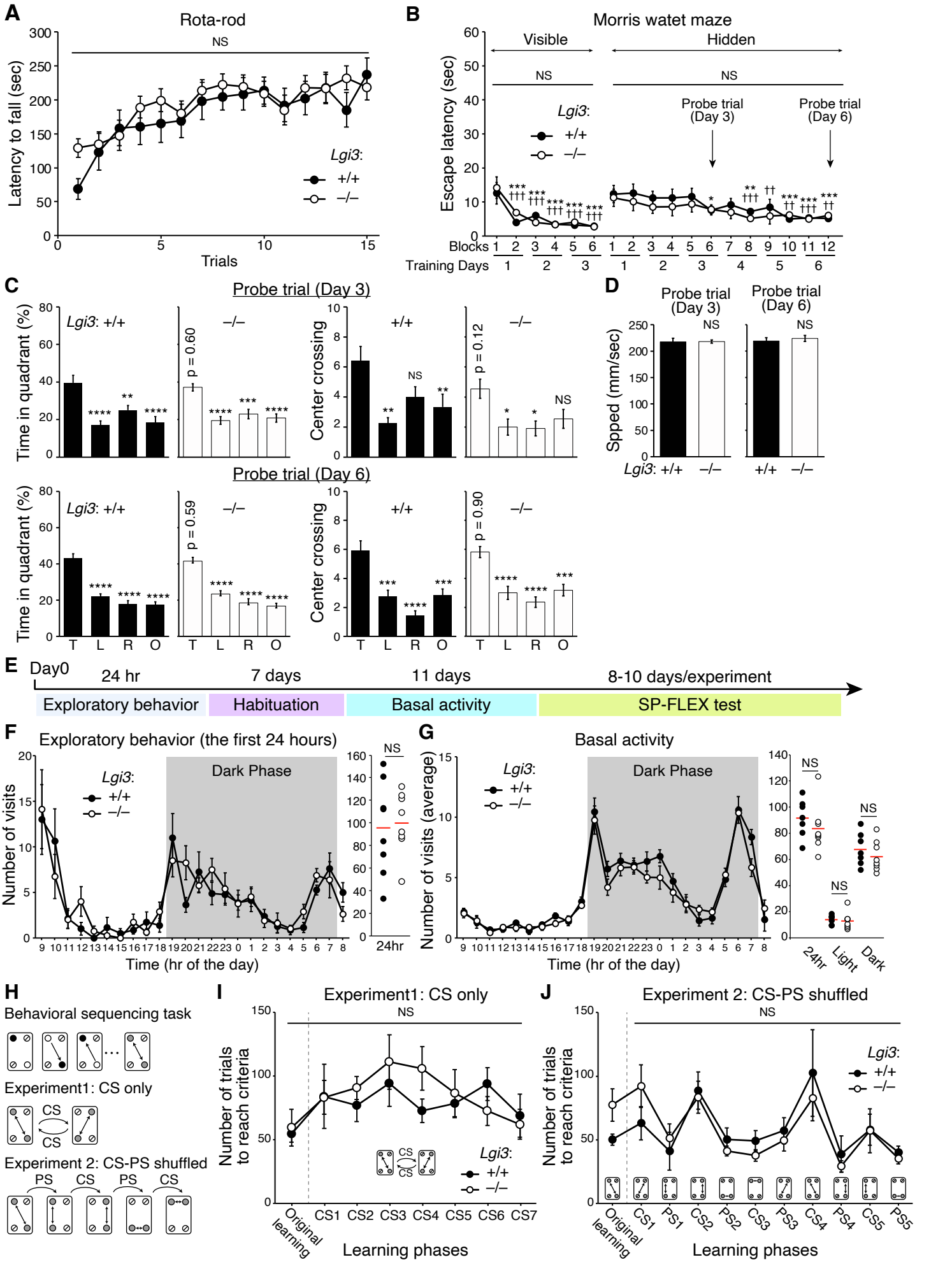
A
Rota-rod
NS
Latency to fall (sec)
Trials
Lgi3:
+/+
–/–
B
Morris watet maze
Visible
Hidden
NS
NS
Escape latency (sec)
Probe trial (Day 3)
Probe trial (Day 6)
Blocks
Training Days
C
Probe trial (Day 3)
Probe trial (Day 6)
Time in quadrant (%)
Center crossing
p = 0.60
p = 0.12
p = 0.59
p = 0.90
T L R O
D
Probe trial (Day 3)
Probe trial (Day 6)
Spped (mm/sec)
E
Day0
24 hr
7 days
11 days
8-10 days/experiment
Exploratory behavior
Habituation
Basal activity
SP-FLEX test
F
Exploratory behavior (the first 24 hours)
Dark Phase
Number of visits
Time (hr of the day)
24hr
G
Basal activity
Number of visits (average)
24hr
Light
Dark
H
Behavioral sequencing task
Experiment1: CS only
CS
Experiment 2: CS-PS shuffled
PS
I
Experiment1: CS only
Number of trials to reach criteria
Original learning
CS1 CS2 CS3 CS4 CS5 CS6 CS7
Learning phases
J
Experiment 2: CS-PS shuffled
Original learning
CS1 PS1 CS2 PS2 CS3 PS3 CS4 PS4 CS5 PS5
Learning phases

Figure S8

Figure S8. Bhehavioral anaysis of *Lgi3*$^{-/-}$ mice

(**A**) Motor coordination and learning are intact in the *Lgi3*$^{-/-}$ mice (Rota-rod test). Mice were placed on an accelerating rotating rod. The speed of the rod is accelerated from 5 rpm to 40 rpm over 300 sec. Latency to fall of 15 trials of three consecutive days is shown in the graph. n = 13 per genotype. Two-way repeated measures ANOVA. Genotype effect, $F_{(1, 24)} = 0.37$, p = 0.55. NS, not significant. mean ± SEM.

(**B**, **C**, and **D**) Spatial recognition and memory of *Lgi3*$^{-/-}$ mice were examined by the Morris water maze tasks. (B) Escape latencies in the visible platform trials (six blocks of the first three days) and the following hidden platform trials (twelve blocks of the six days) of *Lgi3*$^{-/-}$ mice were compared to the wild-type. Two-way repeated measures ANOVA. Visible platform trial: interaction, $F_{(5, 105)} = 0.90$, p = 0.49; genotype, $F_{(1, 21)} = 0.31$, p = 0.58; blocks of trial effect, $F_{(11, 105)} = 19.22$, p < 0.001; Hidden platform trial: interaction, $F_{(11, 231)} = 0.65$, p = 0.78; genotype, $F_{(1, 21)} = 0.82$, p = 0.37; blocks of trial effect, $F_{(11, 231)} = 7.14$, p < 0.001. NS, not significant. Bonferroni's post hoc test. *p <0.05, **p <0.01, ***p <0.001 (wild-type); †p <0.05, ††p <0.01, †††p <0.001 (*Lgi3*$^{-/-}$) (vs the first trial in each training). mean ± SEM. (C) Probe trials were performed on days 3 and 6 after training trials. Percentage time in each quadrant (left) and the number of center crossings of the hypothetical platform (right) were analyzed. One-way ANOVA post hoc Tukey's test (vs target in each genotype). NS, not significant, *p <0.05, **p <0.01, ***p <0.001, and ****p <0.0001. P-values in the graph show the differences in the target quadrant or center crossing between wild-type and *Lgi3*$^{-/-}$ mice (Student t-test). mean ± SEM. T, target quadrant; L, left quadrant; R. right quadrant; O, opposite quadrant. (D) Swimming speed measured for 60 sec in the probe trials on days 3 and 6 was not significantly different between genotypes (Student t-test). mean ± SEM. (B-D) n = 11 (wild-type mice) and n = 12 (*Lgi3*$^{-/-}$ mice).

(**E**) Experimental schedule of behavioral analysis using IntelliCage. SP-FLEX test, Self-paced behavioral sequencing learning and behavioral FLEXibility test.

(**F** and **G**) Exploratory behavior (F) and basal activity (G) of *Lgi3*$^{-/-}$ mice and wild-type control mice were assessed. The total number of corner visits during the 24 hr of the exploratory behavior task (F, right) and the mean number of corner visits for the 24-hour, light, and dark period are shown in graph (G, right), respectively. Student t-test. NS, not significant. Red lines represent the mean value. (F) n = 8 mice per genotype. (G) n = 7 (wild-type mice) and n = 8 (*Lgi3*$^{-/-}$ mice). mean ± SEM.

(**H**) Behavioral sequencing task scheme for self-paced learning and flexibility, showing opposite rewarded corners where the mouse has to go back and forth. In the complete shift (CS)-only task, the diagonally opposite rewarded corners are alternated sequentially with the other, upon achieving the successful visit-rate criterion at one diagonal. In the shuffled task, CS is alternated with the partial shift (PS) task, where only one of the two previously rewarded corners is switched with a nonrewarded corner. Black-filled circle, rewarded corner (active); Open circle, rewarded corner (inactive); crossed-out circle, non-rewarded corner; gray-filled circles connected with double arrow, rewarding sequence.

(**I** and **J**) No significant differences were observed between genotypes in the CS-only and CS-PS-shuffled SP-FLEX experiments. Two-way repeated-measures ANOVA. CS-only (I): genotype effect, $F_{(1, 13)} = 0.26$, p = 0.62, NS, not significant. n = 7 (wild-type mice) and n = 8 (*Lgi3*$^{-/-}$ mice); CS-PS-shuffled (J), genotype effect, $F_{(1, 12)} = 0.067$, p = 0.80. n = 6 (wild-type mice) and n = 8 (*Lgi3*$^{-/-}$ mice). mean ± SEM.

Table S1. Summary of FISH analysis of *Lgi1*, *Lgi2*, and *Lgi3* expression in oligodendrocytes in the mouse brain, Related to Figure 1

	Lgi3$^+$ /DAPI$^+$ cells (%)	*Mbp*$^+$ /DAPI$^+$ cells (%)	*Mbp*$^+$ /*Lgi3*$^+$ cells (%)	*Lgi3*$^+$ /*Mbp*$^+$ cells (%)	*Lgi1*$^+$ /DAPI$^+$ cells (%)	*Mbp*$^+$ /*Lgi1*$^+$ cells (%)	*Lgi2*$^+$ /DAPI$^+$ cells (%)	*Mbp*$^+$ /*Lgi2*$^+$ cells (%)
Corpus Callosum	69.8	65.3	83.8	89.7	N.D.	N.D.	N.D.	N.D.
Internal capsule (Striatum)	52.8	55.7	92.9	88.1	N.D.	N.D.	N.D.	N.D.
Cerebellum (White matter)	46.9	45.3	86.3	89.1	2.0	N.D.	N.D.	N.D.
Cortex layer 5/6	42.3	22.7	51.0	87.9	45.8	N.D.	23.2	N.D.
Cortex layer 2/3	49.2	5.4	10.6	100.0	51.4	N.D.	21.6	N.D.
Thalamus	54.8	24.5	43.0	94.6	25.2	N.D.	N.A.*2	N.D.
Medulla	58.8*1	29.5	45.2*1	89.0	28.5	N.D.	N.A.*2	N.D.

The average percentage of two independent experiments is shown (P125, C57BL/6 mouse brains).

*1: The subregions in the medulla, in which *Lgi3*$^+$ cells are locally clustered, are excluded from the calculation.

*2: *Lgi2*$^+$ cells are not distributed uniformly in the thalamus and medulla.

N.D., not detected; N.A., not applicable.

Table S3. Kv1 channel peptides identified in LGI3-mediated protein complexes by proteomic analysis, Related to Figure 3

	Amino acid sequence*	# PSMs
Kcna1	[R].NRPSFDAILYYYQSGGR.[LI]	8
(Kv1.1)	[R].NEYFFDR.[NH]	4
	[R].RPVNVPLDMFSEEIK.[F]	4
	[R].QVWLLFEYPESSGPAR.[VGI]	4
	[M].TVMSGENADEASTAPGHPQDGSYPR.[Q]	1
	[R].VVINISGLR.[F]	4
	[K].TLAQFPNTLLGNPK.[K]	1
	[K].GLQILGQTLK.[A]	2
	[K].FYELGEEAMEK.[F]	1
	[KR].FREDEGFIK.[E]	1
Kcna2	[R].NRPSFDAILYYYQSGGR.[LI]	8
(Kv1.2)	[R].NEYFFDR.[NH]	4
	[R].RPVNVPIDIFSEEIR.[F]	16
	[R].QVWLLFEYPESSGPAR.[VGI]	4
	[M].TVATGDPVDEAAALPGHPQDTYDPEADHECCER.[V]	4
	[R].VVINISGLR.[F]	4
	[K].TLAQFPETLLGDPK.[K]	4
	[K].EEERPLPENEFQR.[Q]	3
	[R].ETEGEEQAQYLQVTSCPK.[I]	2
	[K].GLQILGQTLK.[A]	2
	[R].FYELGEEAMEMFR.[E]	2
Kcna3	[R].NRPSFDAILYYYQSGGR.[LI]	8
(Kv1.3)	[R].NEYFFDR.[NH]	4
	[R].RPVNVPIDIFSEEIR.[F]	16
	[R].QVWLLFEYPESSGPAR.[VGI]	4
	[R].VVINISGLR.[F]	4
	[K].GLQILGQTLK.[A]	2

Kcna4	[R].NRPSFDAILYYYQSGGR.[LI]	8
(Kv1.4)	[R].NEYFFDR.[NH]	4
Kcna6	[R].NRPSFDAILYYYQSGGR.[LI]	8
(Kv1.6)	[R].NEYFFDR.[NH]	4
	[R].QVWLLFEYPESSGPAR.[VGI]	4
Kcna10	[R].NEYFFDR.[NH]	4
(Kv1.8)	[K].GLQILGQTLK.[A]	2

* The peptide sequences shown in black indicate uniquely identified peptides, while the peptide sequences shared between different Kv1 channels are shown by the same color other than black.

PSM, peptide-spectrum match.

Table S4. Electrophysiological properties of L5a PCs, Related to Figure 7

	Wild-type (control)	*Lgi3*$^{-/-}$
Resting membrane potentials (mV)	-70.7 ± 4.2	-71.9 ± 5.2
Input resistance (MΩ)	96.2 ± 25.7	92.7 ± 31.0
Spike threshold (mV)	-42.7 ± 3.1	-42. 5 ± 5.6
Spike height (mV)	81.5 ± 7.5	79.1 ± 8.7
Spike width (msec)	3.6 ± 1.1	3.9 ± 1.4

Table S5. Electrophysiological properties of L2/3 PCs, Related to Figure 7

	Wild-type (control)	*Lgi3*$^{-/-}$
Resting membrane potentials (mV)	-79.2 ± 1.8	-78.8 ± 1.5
Input resistance (MΩ)	72.1 ± 19.7	71.6 ± 21.0
Spike threshold (mV)	-39.9 ± 1.9	-40.0 ± 2.1
Spike height (mV)	83.7 ± 4.1	83.4 ± 7.3
Spike width (msec)	3.7 ± 0.4	3.8 ± 0.5